# X-ray Astrophysics: The Spoiler Clusters and XRISM Synchrotron Calibrations

by

Connor Martz

A thesis
presented to the University of Waterloo
in fulfillment of the
thesis requirement for the degree of
Master of Science
in
Physics

Waterloo, Ontario, Canada, 2019

## Author's Declaration

I hereby declare that I am the sole author of this thesis. This is a true copy of the thesis, including any required final revisions, as accepted by my examiners.

I understand that my thesis may be made electronically available to the public.

## Abstract

Cool core galaxy clusters hosting brightest cluster galaxies (BCGs) in their centres radiate away their energy on timescales of less than $10^9$ yr. If cooling wasn't offset by some form of heating, the hot atmosphere would cool and continously form stars at rates of hundreds to thousands of solar masses per year. However, observations by *Chandra* have revealed no evidence of gas cooling at these expected rates. Instead, predicted cooling rates are counteracted via mechanical feedback from active galactic nuclei (AGN), which heats the intracluster medium (ICM) and suppresses cooling. Observations have shown that nebular emission and molecular gas in BCGs are associated with rising X-ray bubbles inflated by radio jets launched by massive black holes. Molecular clouds have either condensed from low entropy gas being uplifted in the wakes of X-ray bubbles or can be lifted directly.

In this thesis I present an analysis of a sample of five cool-core galaxy clusters (A2029, A2151, A2107, EXO0422-086, RBS0533) observed with the *Chandra X-ray Observatory* selected on the basis of having an upper limit on $H\alpha$ emission in the ACCEPT database, yet with short central cooling times. I extract thermodynamic profiles for each cluster and show that the central cooling time and entropy falls below $\sim$1 Gyr and 30 kev cm$^2$ respectively. I thorougly explore each cluster for evidence of X-ray bubbles, and discuss a method of detecting and confirming the significance of bubbles. Only RBS0533 has detectable radio/X-ray bubbles which are commonly associated with cooling atmospheres. Although, despite its prominent X-ray bubble, RBS0533 lacks significant levels of molecular gas. I argue that cold gas is absent at appreciable levels in these systems because radio bubbles are either absent or in the case of RBS0533, its radio bubbles are unable to lift low entropy atmospheric gas to an altitude where the ratio of the cooling time to the free-fall time falls below unity.

I also search for signatures of uplifted gas in our sample by creating metallicity maps and extracting thermodynamic profiles along radio jet axis and "off" of radio jet axis' to determine if metal enriched gas preferentially lies along the former. Inspection of maps and subsequent statistical analysis of profiles confirms that metal-rich plasma does not preferentially lie along any direction.

Finally, I present an analysis of my work during a filter calibration project for the X-ray Imaging and Spectroscopy Mission (*XRISM*), where I assisted in the calibration of a set of Resolve optical blocking filters (IVCS-6 and OVCS-7A) using metrology synchrotron beamlines at the Canadian Light Source and Advanced Light Source.

**Acknowledgements**

I firstly want to thank my supervisor and mentor Brian McNamara for his guidance, encouragement, and patience in me as I slowly matured into an academic, and well rounded individual. I also want to thank my thesis committee members: Michael Balogh, for his generosity, and his insightful lectures on everything related to galaxies; David Hawthorn, for taking the time out of his busy schedule to help me understand the basics of X-ray absorption spectroscopy; and Michael Hudson for agreeing to be on my thesis defence committee. Moreover I want to extend a thank you out to Megan Eckart and Maurice Leutenegger for allowing myself and the University of Waterloo to participate in an unforgettable project. I'd also like to thank my past supervisor at Wilfrid Laurier University, Ioannis Haranas, without whom I may have never had a chance to pursue my dream of going to graduate school to study Astrophysics.

I would also like to acknowledge a few of my office mates who were critical to my success. Firstly, Adrian Vantyghem, for his many useful lessons and constructive feedback which helped me become a more confident programmer and researcher. Prathamesh Tamhane, for his insightful discussions with me throughout my research, but most importantly, for his friendship and our hour (sometimes several) long conversations. Faerlin Pulido for his advice and support in helping me get started and answering all of my technical questions. Iurii Babyk for all of our interesting conversations and for providing useful feedback on my research and writing. Andrew Reeves, for his ability to never fail in making me laugh. Muzi Li, for being one of the most pleasant travelling companions and for all of her assistance during the calibration project. Lastly, a special thanks to Marie-Joelle Gingras for her resourcefulness, relentlessness, and support in searching through several papers for data that helped improve my work considerably.

Finally, I'd like to thank my loved ones, without whom I would never have made it this far. My mother, Linda, who has always been a bastion of support for me to lean on, and the person to whom I owe many of my best qualities. My father, Bill, who has always supported me during my best and worst moments, and has taught me the value of generosity and patience. My sister, Sarah, who in many ways has always been my inspiration and taught me to never give up, and that anything is possible if you work hard enough. My brother, Evan, whom I've always looked up too, and whose humour and good nature is what helped shaped me into the man I am today.

Every one of you has been a crucial part of my success up until this point. These short sentiments are not nearly enough to capture how grateful I feel to have had any of you be a part of my life. All I can say is thank you, and that I hope I can impact someone else's life like you've impacted mine.

# Table of Contents

# List of Tables

# List of Figures

# Chapter 1

# Thermally Unstable Cooling Stimulated by Uplift

## 1.1 Introduction

Galaxy clusters are the largest and most virialized structures in the Universe, and are gravitationally bounded by its own self gravity. Typically, they contain hundred to thousands of individual galaxies spread over spatial regions of several Mpc. Within a few kpc of the gravitational potential well usually resides a central dominant galaxy (cD) otherwise known as a supergiant elliptical galaxy. When a galaxy within the cluster is dominant in its mass and luminosity it is referred to as the brightest cluster galaxy (BCG). The BCG is usually coincident with the peak X-ray emission. (Sarazin, 2009).

Prior to the launch of the *Uhuru* space satellite in 1970, X-ray emission had only been reported in three external galaxies (Gursky, 1973). Its superior sensitivity and sky coverage led to detections in 43 X-ray emitting clusters of galaxies (Gursky and Schwartz, 1977). Since then, several hundred galaxy clusters have been observed by many different satellites including: *OSO*8 (1975), *Einstein* (1978), *EXOSAT* (1983), *ROSAT* (1990), and *Chandra* (1999).

Clusters of galaxies have masses that range between $10^{14} - 10^{15} \mathrm{M}_{\odot}$. Velocity dispersion measurements of galaxies within clusters implies that only 3% of this mass is contained within individual stars residing in galaxies. Permeating the space between cluster galaxies is a dilute hot plasma called the intracluster medium, which accounts for roughly 13% of the clusters total mass. The vast majority of the remaining mass in clusters (84%) is

contained within non-baryonic (dark) matter which interacts only through gravitational effects (Peterson and Fabian, 2006).

### 1.1.1 Intracluster Medium

The intracluster medium (ICM), is a dilute plasma consisting primarily of primordial hydrogen and helium that was accreted by the cluster. The intracluster gas maintained at virial temperatures of $10^7 - 10^8$ K is almost entirely ionized. These temperatures are consistent with measurements from the line of sight velocity dispersion of cluster galaxies, $\sigma$, through the relation $T_X \propto \sigma^2$ (Mushotzky et al., 1978).

The ICM radiates primarily in X-rays through coulomb interactions between electrons and ions to produce thermal bremsstrahlung (free-free) emission Sarazin (2009). Below temperatures of $3 \times 10^7$ K, X-ray emission is dominated by metal recombination lines including the Mg, Si, and Fe lines to name a few (Böhringer and Werner, 2010). The total X-ray luminosity radiated by the ICM is given by:

$$L_X = \int n_e n_H \Lambda(T, Z) dV, \tag{1.1}$$

where $n_e$ is the electron number density, $n_H$ is the hydrogen number density, $V$ is the volume, and $\Lambda(T, Z)$ is the cooling function, which is calculated by integrating the emission from processes such as the ones mentioned above, and is also weighted by the energy of the observed photons (Peterson and Fabian, 2006). This cooling function will be addressed later in Section 1.3.2.

Gas densities are related to the normalization of the spectrum through emission measure, $\int n_e n_H dV$. The density of gas in clusters is distributed into a configuration within the atmosphere as to maintain hydrostatic equilibrium, and ranges from $10^{-1}$ cm$^{-3}$ in the central regions to $10^{-4}$ cm$^{-3}$ in the outskirts. The cooling time, $t_{\rm cool}$, due to free-free emission is significantly longer than the sound crossing time, $t_{\rm c}$, as is the Hubble time. The sound crossing time determines the time-scale to restore hydrostatic equilibrium Sarazin (2009). In a system that is spherically symmetric, the condition for hydrostatic equilibrium is given by:

$$\frac{1}{\rho}\frac{dp}{dR} = -\frac{GM(< R)}{R^2}, \tag{1.2}$$

where $\rho$ is the gas density, $p$ is the pressure, $M(< R)$ is the mass enclosed within radius $R$. The gas pressure is related to gas density using the ideal gas law,

$$p = \frac{\rho k_B T}{\mu m_p}, \tag{1.3}$$

where $k_B$ is the Boltzmann constant, $T$ is the temperature, $\mu$ is the atomic mass constant, and $m_H$ is the mass of proton. With these assumptions, the enclosed gravitating cluster mass is given by measuring the radial temperature and gas density profiles and calculated following,

$$M(< R) = -\frac{k_B T R^2}{\mu m_p G}\left[\frac{d\ln\rho}{dR} + \frac{d\ln T}{dR}\right]. \tag{1.4}$$

### 1.1.2 Cooling Flows

The cores of galaxy clusters continuously cool by radiating away thermal energy via X-rays. In the absence of heating mechanisms, the thermal energy is radiated away in a cooling time,

$$t_{\rm cool} = \frac{E_{\rm thermal}}{L_X} = \frac{3p}{2n_e n_H \Lambda(T, Z)}. \tag{1.5}$$

The density within relaxed clusters can reach levels of $10^{-1}$ cm$^{-3}$ causing the cooling time to fall below $10^9$ yr (Rafferty et al., 2008). This time scale is far shorter than the age of the cluster or even the time scale for previous heating events, which is indicative of a cooling flow.

As the gas within the cores of clusters radiates away energy, its density correspondingly increases to maintain hydrostatic equilibrium. The only way density can rise is for gas to flow inwards towards the center to slowly replenish the condensing gas. This increase in density also increases the X-ray luminosity which in turn increases the cooling rate (Fabian, 1994). In absence of heating mechanisms, this would result in a positive feedback loop and cause clusters to cool rapidly and deposit mass out of the ICM at rates of 100 - 1000 M$_\odot$ yr$^{-1}$,

$$\dot{M} = \frac{2}{5}\frac{\mu m_p L_{\rm cool}}{kT}. \tag{1.6}$$

Where $\mu \approx 0.61$ is the mean molecular weight of the ICM plasma, the 2/5 factor arises from the enthalpy of a monoatomic ideal gas, and $L_{\rm cool}$ is the central luminosity of the cluster and generally represents 10% of the clusters total luminosity Fabian (1994). Observations of galaxy clusters reveals a number of issues with this model of cooling flows. For instance, if mass were being deposited at the rates quoted above, then central regions of clusters should possess a plethora of young blue stars and harbour massive reservoirs of molecular gas. In addition, these young stars would shine brightly in UV and optical wavelengths, but observations reveal star formation rates of $1 - 100$ $\mathrm{M_{\odot}yr^{-1}}$ (Johnstone et al., 1987; O'Dea et al., 2004). Continuous cooling of the ICM at the rates 100 - 1000 $M_{\odot}\mathrm{yr}^{-1}$ over a fraction of the Hubble time could produce enormous quantities of molecular gas, $10^{11} - 10^{12}$ $\mathrm{M_{\odot}}$, which would be distributed over the central 100 kpc of the cluster Salomé and Combes (2003). On the other hand, cool gas and star formation is typically observed within the central tens of kpc, and molecular gas reservoirs are several orders of magnitude lower than predicted (Edge, 2001).

This implies that radiative losses in the ICM are being offset by some source of heating. The most plausible heating mechanism in clusters of galaxies is from active galactic nuclei (AGN), which is addressed in the following section.

### 1.1.3 AGN Feedback as a Heating Mechanism

The lack of evidence for cooling rates and star formation rates predicted by the cooling flow model suggests that some source of heating must be present to suppress cooling in the ICM. Heating mechanisms must be sufficient to offset radiative losses, which can on average range between $10^{42} - 10^{44}$ erg $\mathrm{s^{-1}}$. X-ray luminosities that lie in this range would require at least $10^{60} - 10^{62}$ erg of energy to be injected into the central 100 kpc over a time scale of $5 - 10$ Gyr.

Several heating processes have been proposed to remedy this problem, including heating through supernova feedback (Mathews and Baker, 1971), thermal conduction (Voigt and Fabian, 2004), and mergers (Sarazin, 2002). However, these first and last mechanisms have been shown to fall short of energies required to offset radiative cooling rates on cluster scales (Boehringer and Werner, 2009; Sarazin, 2009), and thermal conduction is ineffective in clusters where $t_{\rm cool}$ is short ($< 1$ Gyr) (Parrish et al., 2009; Voit and Donahue, 2015a).

Observations taken by the *Chandra* and *XMM-Newton* observatories have implicated the AGN residing at the center of galaxy clusters as the most likely heating candidate. In the standard model, accretion of cooling gas onto the central black hole within brightest cluster galaxies (BCGs) and giant ellipticals (gE), drives relativistic jets outwards from

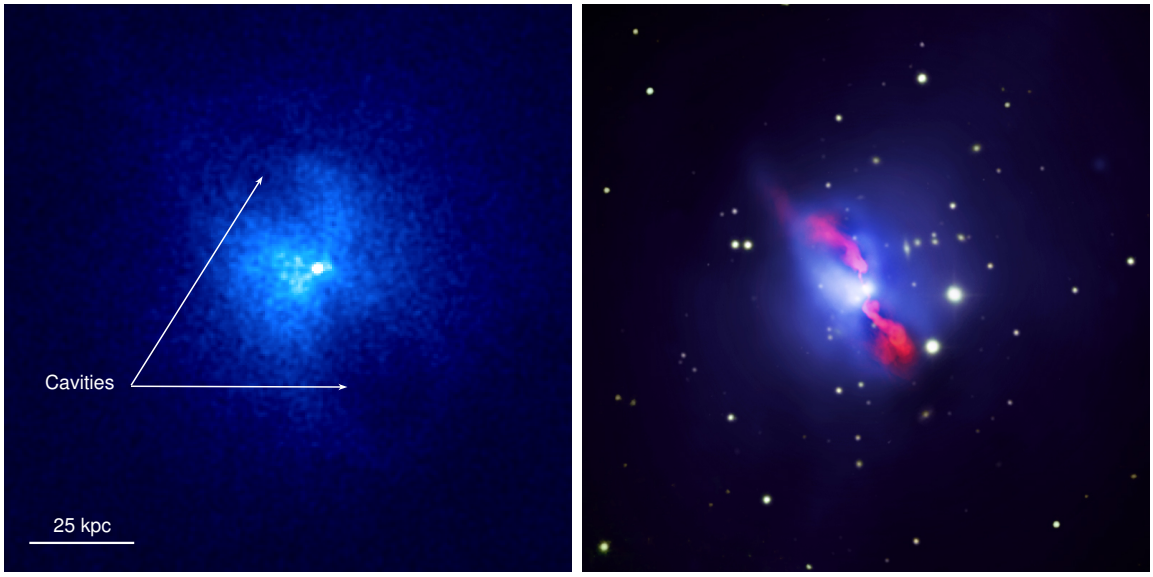


Figure 1.1: **Left**: *Chandra* X-ray image of Hydra-A showcasing its two cavities. **Right**: Composite image of Hydra-A, with: X-ray emission from Chandra (blue), VLA radio emission (red), DSS optical (yellow). Credit: Kirkpatrick et al. (2009)

the AGN which inflate buoyantly-rising X-ray bubbles into the atmosphere heating the ICM in the process (see McNamara and Nulsen 2007 for a review). High resolution X-ray imaging has revealed that these bubbles are visible in images as disturbances in the ICM in the form of surface brightness depressions as shown in Figure 1.4. These cavities have been detected in over 70% of clusters with short central cooling times (Dunn et al., 2005; Bîrzan et al., 2012).

X-ray cavities are elliptical regions that range in size from a few to hundreds of kpc in diameter, and are visible as surface brightness depressions of $20-30\%$ relative to their surroundings. Radio synchrotron emission fills these cavities (see Figure 1.1) and originates from relativistic electrons and magnetic fields (De Young, 2006).

The kinetic power of jets can be estimated from the work required to inflate the cavity, where additional energy is needed to displace the ICM, so the total cavity energy is given by its enthalpy (McNamara and Nulsen, 2007):

$$P_{\rm jet} = \frac{\gamma}{\gamma - 1}\left(\frac{pV}{t_{age}}\right), \tag{1.7}$$

where $p$ and $V$ are the cavity's pressure and volume respectively, $\gamma$ is the ratio of heat capacities which is 4/3 for a relativistic gas and 5/3 for a non-relativistic monatomic gas, $t_{\rm age}$ is the cavity's age. Three estimates are commonly used as a proxy for a cavity's age: the buoyant rise time, $t_{\rm buoy}$, the refill time, $t_{\rm r}$, and the sound crossing time, $t_{\rm c}$. In general, the buoyancy time, or the time taken for a bubble to rise at its buoyant terminal speed from the center of the cluster to its present location, is the best indicator of a cavity's age (Vantyghem et al., 2014; McNamara and Nulsen, 2007). Measured cavity power range between $10^{42} - 10^{46}$ erg s$^{-1}$, and roughly scales linearly with the luminosity of cooling regions, which suggests AGN feedback is sufficient to balance radiative cooling (Rafferty et al., 2006).

### 1.1.4 Thermal Instability

Suppose a parcel of gas with volume, $V$, at a radius, $R$, from the cluster centre, is in a stratified atmosphere in hydrostatic equilibrium with gas density, $\rho(R)$. If this parcel of gas is incompressible and displaced from its original position to a lower altitude, $z$, then it experiences a buoyant force given by,

$$F_{\rm buoy} = g[\rho(z-R) - \rho(R)]V \tag{1.8}$$

where $g$ is the local gravitational acceleration. From Newton's Second Law of Motion, $F = \rho(z-R)V\frac{d^2z}{dt'^2}$. Using a linear approximation, one can approximate the difference in densities in Equation 1.8 as,

$$\rho(z-R) - \rho(R) \sim \frac{d\rho(R)}{dR}z, \tag{1.9}$$

which can be used to simplify the above to a second-order differential equation,

$$\frac{d^2z}{dt'^2} = \frac{g}{\rho(R)}\frac{d\rho(R)}{dR}z, \tag{1.10}$$

this equation has a straightforward solution given by:

$$z = z_0 e^{\sqrt{-\nu_{BV}}t}, \tag{1.11}$$

where $\nu_{BV}$ is the Brunt-Väisälä frequency given by,

$$\nu_{BV}^2 = -\frac{g}{\rho(R)}\frac{d\rho(R)}{dR}. \tag{1.12}$$

This derivation indicates that when an incompressible parcel of gas is displaced to a lower altitude in an atmosphere, its density becomes lower than its surroundings since pressure decreases with height; meaning the gas must experience an upward force to maintain hydrostatic equilibrium. As it rises upward, it moves to an altitude where it is again surrounded by lower density gas, and so it experiences a downward force to compensate. The parcel of gas then will oscillate about this equilibrium altitude with frequency given by Equation 1.12.

In contrast to this discussion above, gas in realistic intracluster atmospheres are compressible. A parcel of gas will radiate away energy and cool in a timescale of $t_{\rm cool}$, causing its density to increase and thus the parcel of gas to free-fall towards the center in a time scale of $t_{\rm ff}$. The gas falls towards the center of the gravitational potential well until it reaches a point where it can maintain hydrostatic equilibrium with its surroundings.

If $t_{\rm cool}$ is significantly less than $t_{\rm ff}$, than it is cooling faster than gravity is able to respond. Upon reaching an equilibrium point, it will have cooled significantly and raised the density required to maintain hydrostatic equilibrium, thus the equilibrium level must be deeper in the clusters gravitational potential. If $t_{\rm cool}$ is significantly longer than $t_{\rm ff}$, density perturbations will oscillate about their equilibrium point with Brunt-Väisälä frequency.

A number of studies have pointed out that cooling gas may become thermally unstable which gives rise to filaments of cold gas observed in cooling flows (Fabian et al., 1980; Cowie et al., 1983). When gas becomes thermally unstable, density fluctuations cause overdense blobs of gas to form, which cool to low temperatures. Some of these blobs will sink towards the central black hole, while others may eventually disassociate from the hot atmosphere and may contribute to the formation of stars or cold molecular clouds (Cowie et al., 1980; Pizzolato and Soker, 2005b). Thermal instability has been shown to be guaranteed through theory (Nulsen, 1986), and simulations (McCourt et al., 2012), when the ratio of cooling to free-fall time satisfies, $t_{\rm cool}/t_{\rm ff} \lesssim 1$. More recent studies indicate that its value is less stringent than this, and occurs when $\min(t_{\rm cool}/t_{\rm ff}) \lesssim 10$ (Sharma et al., 2012; Voit and Donahue, 2015a), although observations fail to support this conjecture (Hogan et al., 2017b).

In the next section, I continue the discussion on thermal instability and discuss the correlation between cold gas in cluster cores and the surrounding hot atmosphere. In addition, we also argue that AGN feedback "stimulates" the condensation of cold gas.

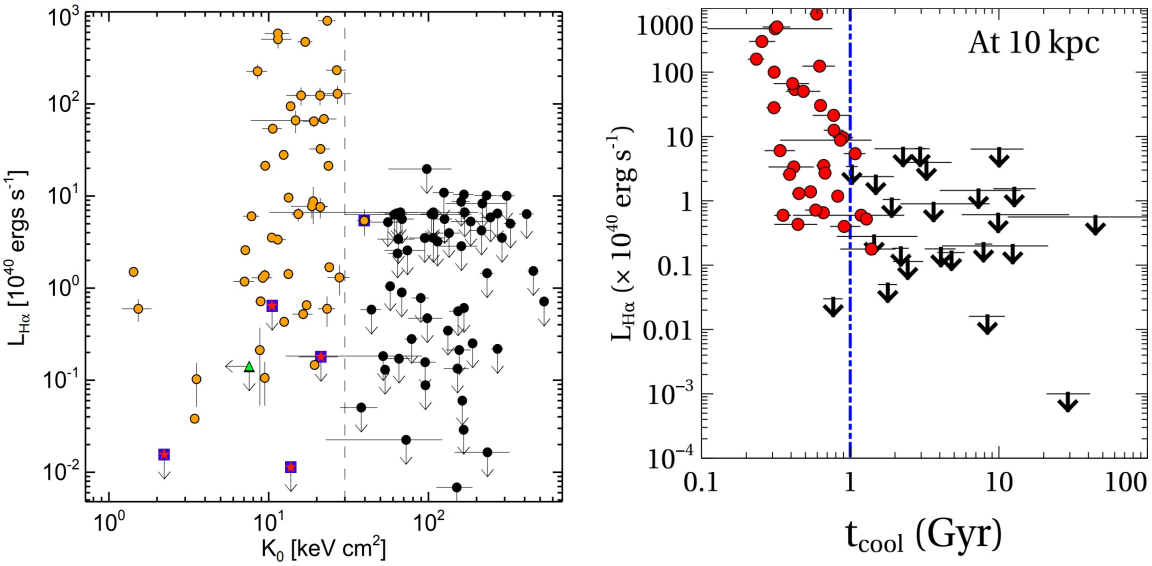


Figure 1.2: **Left**: Central entropy vs. H$\alpha$ luminosity, where orange circles are H$\alpha$ detections, black circles, squares filled with stars, and the green triangle are non-detection upper limits (Cavagnolo et al., 2008). **Right**: Central cooling time measured at 10 kpc vs. H$\alpha$ luminosity, where red circles represent H$\alpha$ detections and black arrows are upper limit detections (Hogan et al., 2017b).

### 1.1.5 Uplift

Tracers of cold gas have been shown to be highly correlated with the properties of hot atmospheres residing in clusters. In Figure 1.2, the H$\alpha$ luminosity (ionized gas at $\sim 10^4$ K which traces star formation) are plotted against the central cooling time and entropy index of the hot gas. Systems with cold gas are preferentially observed in systems where the cooling time falls below 1 Gyr (Rafferty et al., 2006; Hogan et al., 2017b), or when the central entropy is less than 30 keV cm$^2$ (Cavagnolo et al., 2008). These thresholds show that cold gas and the surrounding atmosphere in clusters of galaxies are related, suggesting that cold gas may form via thermal instabilities which cause the ICM to cool.

"Precipitation models" propose that thermal instabilities occur when these two thresholds are satisfied and when the minimum ratio of cooling time to free-fall time threshold is $\min(t_{\rm cool}/t_{\rm ff}) \lesssim 10$ (McCourt et al., 2012; Gaspari et al., 2013; Singh and Sharma, 2015; Voit et al., 2015b), although others have shown that instability ensues when $t_{\rm cool}/t_{\rm ff}$ falls within the range, $\sim 4-20$ (Voit and Donahue, 2015a), or $\sim 1-20$ (Li et al., 2015). When this instability is breached, cool gas condenses from the hot atmosphere increasing the rate

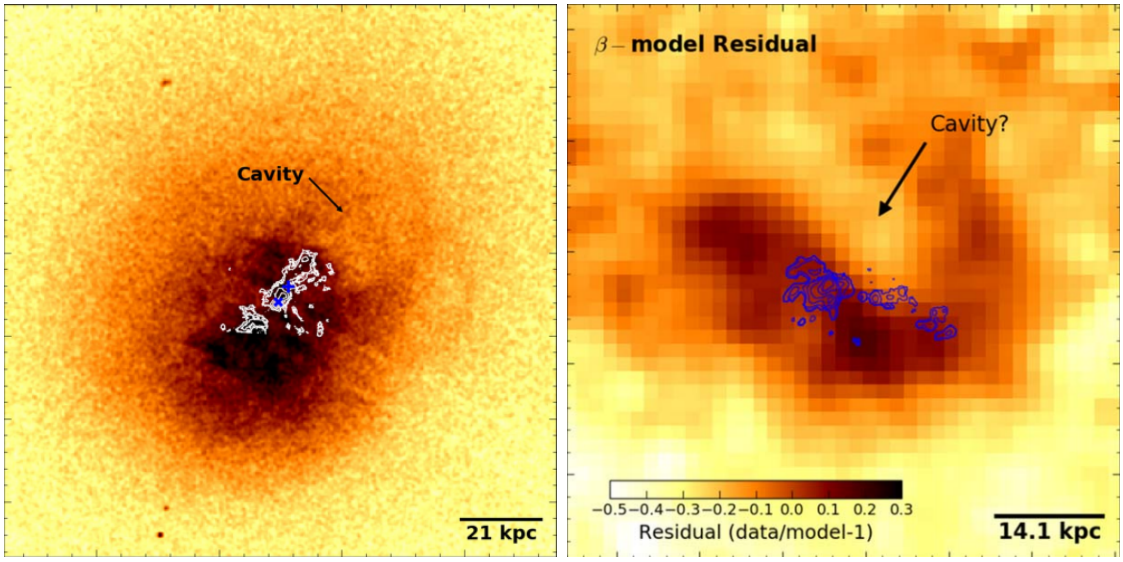


Figure 1.3: **Left**: Chandra X-ray image of 2A 0335+096, overlaid in white contours are H$\alpha$ emission extending towards an energetic cavity (Vantyghem et al., 2016). **Right**: Residual X-ray surface brightness image of RXC J1504-0248, after subtracting a double $\beta$-model, with CO(3-2) emission contours overlaid trailing a cavity candidate (Vantyghem et al., 2018).

of accretion onto the AGN. Jet power is known to be correlated with rate of accretion (Agudo et al., 2015), which implies a higher rate of accretion corresponds to a stronger jet power and thus more heat being injected into the ICM, driving $\min(t_{\rm cool}/t_{\rm ff}) \gtrsim 10$. This suppresses the condensation of cold gas, decreasing the rate of accretion onto the AGN. Subsequently, the hot atmosphere will slowly cool, and thus the cycle of cooling and heating repeats itself. When cooling of the hot atmosphere is suppressed via heating, simulations by Li et al. (2015) show that there is a significant delay of up to $1-2$ Gyr before star formation rates begin to decline due to the consumption of cold gas. As a result of this hysteresis effect, some systems with $\min(t_{\rm cool}/t_{\rm ff}) > 10$, still possess cold gas (Pulido et al., 2018).

New observations taken by the Atacama Large Millimeter Array (ALMA) probing molecular gas residing within central cluster galaxies, suggests a more complicated process for the condensation of cold gas than rapid cooling of the hot atmosphere. ALMA observations of 2A 0335+096 (Vantyghem et al., 2016), PKS 0735-191 (Russell et al., 2016) and RXC J1504-0248 (Vantyghem et al., 2018) reveal molecular gas orientated into long filaments. The observed line widths of these filaments are narrow, which implies that the

cold gas formed largely in-situ. In addition, these filaments trail X-ray cavities as shown in Figure 1.3, suggesting an outflow of cold gas in the wakes of cavities.

Motivated by these observations, McNamara et al. (2016) proposed the "stimulated feedback" model, where cold gas condenses from low entropy gas that is lifted outward from the central regions of clusters by buoyantly rising X-ray bubbles. The parcel of gas is lifted approximately to an altitude where thermal instabilities ensue; where its cooling time is shorter than its infall time, $t_{\rm cool}/t_{\rm I} \lesssim 1$. Here, the infall speed is determined by the lesser of the free-fall and terminal speeds of the thermally unstable gas. Where the terminal speed, $v_{\rm t}$, is determined from balancing the buoyant force against the drag force such that, $v_{\rm t} = \sqrt{2gV/(SC)}$. Here, $g$ is the local gravitational acceleration, $V$ is the volume of the bubble, $S$ is the cross section of the bubble, and $C$ is the drag coefficient (Churazov et al., 2001).

This model implies that feedback suppresses cooling on large scales while simultaneously stimulating thermally unstable cooling in the vicinity of the bubble, thus sustaining the feedback loop.

### 1.1.6 Metal-Enrichment from Outflows

The central regions of the ICM is chemically enriched beyond 1/3 solar of the mean metallicity (Allen and Fabian, 1998; Edge and Stewart, 1991), approaching solar values in cool-core clusters (de Grandi and Molendi, 2001). Supernovae (SNe) are primarily responsible for creating and distributing most of the elements heavier than hydrogen and helium. While type II SNe are what initially enriched the ICM to its mean value (Mushotzky et al., 1996) as these types of SNe are not as efficient at producing heavier elements such as iron, as is type Ia SNe (Werner et al., 2008).

Abundance maps of the ICM have demonstrated that metal-rich regions are preferentially aligned along the direction of radio jets (Simionescu et al., 2009; Kirkpatrick et al., 2011) as shown in Figure 1.4. This implies that AGN outbursts are able to couple to the metal-rich gas and displace it to higher altitudes. The maximum radius of the uplifted gas is given by the "iron radius" (Kirkpatrick and McNamara, 2015),

$$R_{\rm Fe} = (62 \pm 26) \times P_{\rm jet}^{0.45\pm0.06}\ [\rm kpc]. \tag{1.13}$$

In practice, this is defined as the radial bin furthest from the clusters centre where the $1\sigma$ error bars for the metallicity profiles (along the jet axis and off of the jet axis) do not overlap (see dotted line in right panel of Figure 1.4). These outflows are transporting

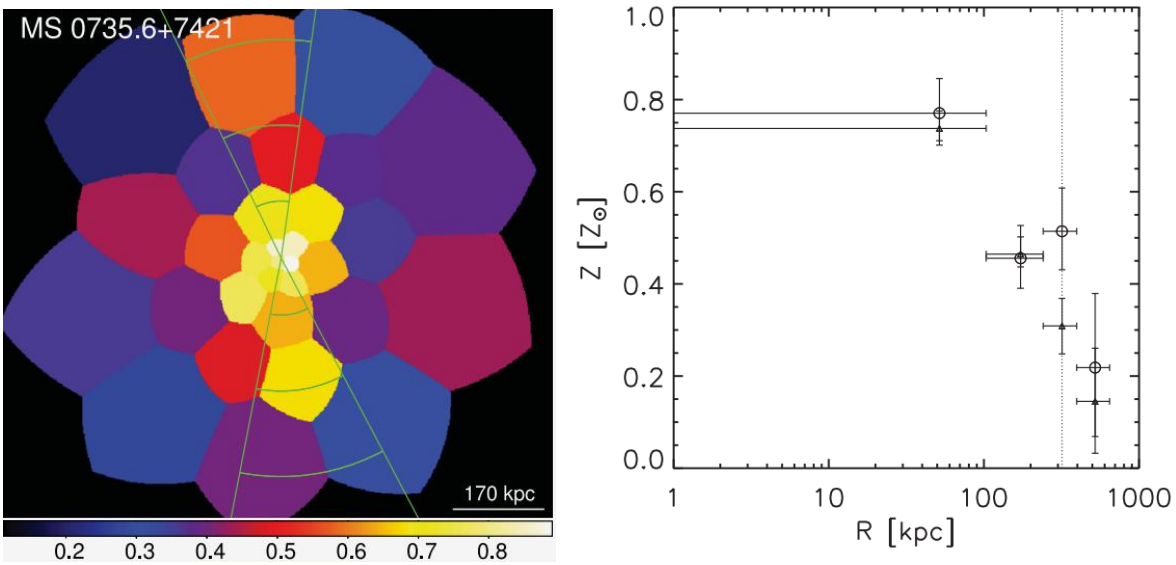


Figure 1.4: Images of MS0735.6+7421 taken from (Kirkpatrick and McNamara, 2015). **Left**: Metallicity map with extracted regions along jet directions shown in green. **Right**: Metallicity profile, where circles represent abundance measured along the jet axis, and triangles are measured off of the jet axis, where the dotted line is the measured iron radius.

significant amounts of gas, with typical outflow rates of 100 $M_\odot$ $yr^{-1}$, with total uplifted masses ranging between $\sim 10^8 - 10^{11}$ $M_\odot$ (Kirkpatrick and McNamara, 2015).

Outflow rates can only balance $10-20\%$ of the cooling rates, and thus would be unable to offset cooling inflows alone, although outflows of hot gas may play a role in offsetting cooling and thus regulating star formation.

### 1.1.7 Goals of this Thesis

It is the objective of this thesis to explore the link between uplift in galaxy clusters and the condensation of cold gas. Cold gas in the form of nebular H$\alpha$ emission is expected to form via thermal instabilities which cause the ICM to cool when the central cooling time falls below 1 Gyr, or when the entropy is less than 30 keV $cm^2$. These thermodynamic properties are commonly associated with molecular clouds, bright H$\alpha$ emission, and star formation in central galaxies. However, several outliers first identified in Cavagnolo et al. (2008), spoil this hypothesis, which are the focus of this work. Five clusters of galaxies: A2029, A2151, A2107, RBS0533, EXO0422-086, referred by some as the "spoiler" clusters,

are systems whose central atmospheric cooling times and entropy index fall below their respective thresholds, yet lack detectable H$\alpha$ emission, or appreciable star formation rates. Moreover, with the exception of a possible candidate in RBS0533, these clusters have no prominent cavity features. Observations using ALMA have also shown that molecular gas in cluster cores preferentially lie in the wakes of buoyantly rising X-ray bubbles (like those shown in Figure 1.3). These considerations, in part, led McNamara et al. (2016) to suggest that thermally unstable cooling instead occurs when low entropy gas from the cluster center is lifted in the updraft of buoyantly-rising X-ray bubbles.

This model proposes that the ability of a galaxy to lift cool gas is key to triggering thermally unstable cooling. If so, then cluster centrals with short atmospheric cooling times yet lacking cold clouds may also be devoid of X-ray cavities capable of lifting the low entropy gas (McNamara et al., 2016). This chapter tests this hypothesis by thoroughly searching for X-ray bubbles, which are commonly associated with short central cooling times. Signatures of uplifted, high metallicity gas are investigated, which are commonly associated with AGN feedback in the form of X-ray bubbles. Moreover, limits are placed on the statistical significance of these results. Thermodynamic profiles are also extracted to determine the $\min(t_{\rm cool}/t_{\rm ff})$, and are used to confirm if objects lie below the central cooling time and entropy thresholds.

This chapter is organized as follows: Firstly the sample and data reduction procedures are outlined in Section 1.2. Cluster surface brightness profiles, thermodynamic profiles are derived along with mass profiles in Section 1.3. In Section 1.4, an analysis technique for determining identification and significance of structure in the ICM is presented, which could be used to search for X-ray cavities/bubbles and other features. In Section 1.5, an examine the atmospheres of our clusters for traces of metal-enriched gas, and place limits on the significance of the findings. In Section 1.7, the findings are summarized and includes a discussion of thermal instabilities within the context of the "spoiler clusters."

## 1.2 X-ray Observations and Data Reduction

To investigate the properties of the hot intracluster gas, we turn to X-ray observations taken with *Chandra*. Section 1.2.1 describes our sample and how it was selected. Section 1.2.2 describes the steps taken to reduce X-ray data. Section 1.2.3 describes our process of how spectra are extracted and fit with XSPEC to measure properties of the ICM.

Table 1.1: *Chandra* X-ray data used in our analysis

| Cluster | z | $N_H$ ($10^{22}$ cm$^{-2}$) | ObsIDs | Total Exposure (ks) | | Cluster Center | |
|---|---|---|---|---|---|---|---|
| | | | | Raw | Cleaned | RA (J2000) | DEC (J2000) |
| | (1) | (2) | (3) | (4) | (5) | (6) | (7) |
| A2029 | 0.0773 | 0.033 | 891, 4977, 6101 | 107.6 | 103.3 | 15:10:56.077 | +05:44:41.05 |
| A2107 | 0.0411 | 0.0445 | 4960 | 35.57 | 34.8 | 15:39:39.043 | +21:46:58.55 |
| A2151 | 0.0366 | 0.0334 | 4996, 19592, 20086, 20087 | 102.8 | 80.2 | 16:04:35.758 | +17:43:18.54 |
| RBS0533 | 0.0123 | 0.102 | 3186, 3187, 5800, 5801 | 108.6 | 107.9 | 4:19:38.105 | +2:24:35.54 |
| EXO0422-086 | 0.0397 | 0.0786 | 19539, 20862, 20863 | 64.5 | 61.6 | 4:25:51.300 | -8:33:38.00 |

**Columns**: (1) redshift, (2) Column density, (3) Observation IDs used for the analysis, (4) Raw combined exposure of the ObsIDs used, (5) useable exposure after data filtering,(6) RA, (7) DEC.

### 1.2.1 Sample

First identified in (Cavagnolo et al., 2008), the "spoiler" clusters: Abell 2029, Abell 2107, Abell 2151, EXO0422-086, and RBS0533 are outliers in the traditional picture of cold gas condensation. Their central atmospheric cooling times and entropy lie below $10^9$ yr and 30 kev cm$^{-2}$, respectively, yet they are devoid of detectable nebular emission and star formation. *Chandra* X-ray data was obtained for A2151 and EXO0422-086, which were observed for 81.02 ks and 54.47 ks respectively, using the ACIS-I instrument. The remaining cluster observations were obtained from the *Chandra* Data Archive (CDA). Cluster coordinates and details of X-ray observations used in this thesis are shown in Table 1.1.

Throughout this thesis a standard ΛCDM cosmology is assumed, with $H_0 = 70$ km s$^{-1}$ Mpc$^{-1}$, $\Omega_m = 0.3$, and $\Omega_\Lambda = 0.7$.

### 1.2.2 Data Reduction

This sample was observed with the *Chandra* X-ray Observatory (CXO) using the Advanced CCD Imaging Spectrometer (ACIS) detector. X-ray properties for our analysis require that spectra be extracted from these observations. The *Chandra* X-ray Center (CXC) provided software for reprocessing event data to ensure that the latest software and calibration updates are applied to observations. Each observation was reprocessed with CIAO version 4.7 and CALDB version 4.6.7. The CHANDRA_REPRO script provided by CXC automates the recommended data processing steps, which applies the newest gain and charge transfer inefficiency correction to the level 1 event files. When possible, VFAINT mode was used to distinguish between good X-ray background events and bad events that are associated with cosmic rays. Photons with bad grades were subsequently removed and the level 2 event files were created. Background light curves are extracted from the level 2 event files, and are filtered using the LC_CLEAN script of M. Markevitch to identify and remove time intervals during an observation that are affected by flares. No observations were significantly affected by flares excluding A2151, where observation 4996 was terminated early and only has 2.3 ks of clean data, the details of raw and cleaned exposure times are given in columns 4 and 5 of Table 1.1. The cleaned level 2 event files were reprojected for each system to match the position of the OBSID with the longest cleaned exposure time. An image for each observation was produced by summing the events in the energy range, $0.5 - 7$ keV. These images were then summed to create a single raw image that is used to identify point sources using WAVDETECT (Freeman et al., 2002) as well as to define concentric annuli that will be used for spectral extraction. Point sources identified using WAVDETECT were visually inspected and excluded from subsequent analysis. The raw images which are not background subtracted or exposure corrected are shown in Figure 1.5

ACIS Blank-sky background were extracted for each observation which combines and reprojects the necessary background files from CALDB to be compatible with event files. Reprocessed blank-sky backgrounds were normalized to the source image count rate in the $9.5 - 12$ keV band. These background files were summed for each system and subtracted from raw images to produce images shown in Figure 1.6. The cluster center is taken to be the location of the BCG as the most massive galaxy closest to the X-ray centroid is one of the best tracers of the dynamical centre in clusters of galaxies (George et al., 2012). This result is also supported by simulations (Cui et al., 2016).

Concentric annuli centered on the BCG were created for each cluster, with the requirements that: The innermost annulus have a radius $\lesssim 10$ kpc and binned to have a minimum of $\sim 3000$ projected counts (background counts excluded), with an increasing number of counts per annulus with increasing distance from the centre. The requirement

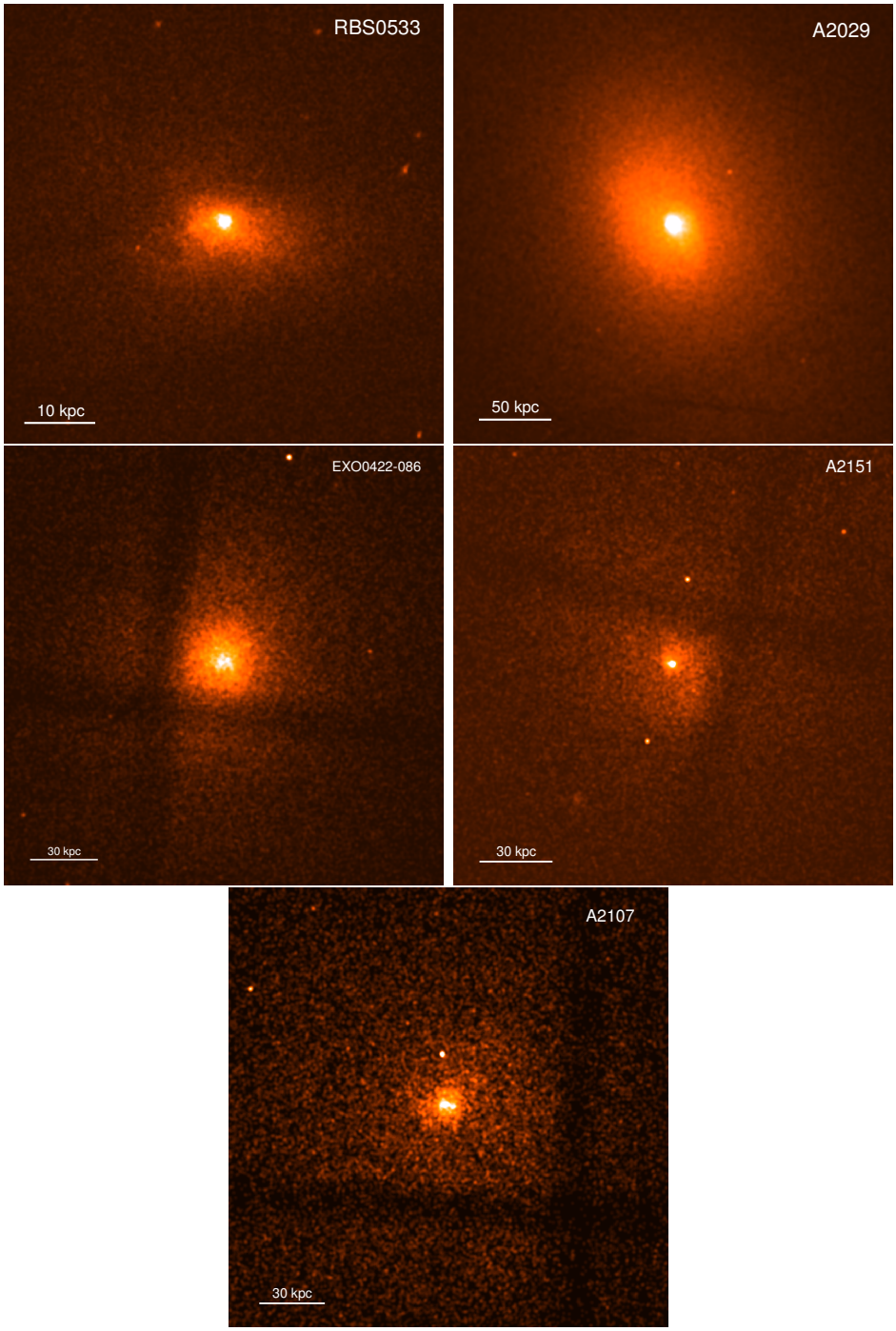


Figure 1.5: Summed Image of each ObsID in Table 1.1. No Background corrections have been applied to the images and each is Gaussian-smoothed with a 3 arcsec kernel radius.

of 3000 counts for the innermost annulus is to ensure that temperatures could be measured accurately in deprojection. Spectra were extracted from these annuli separately for each ObsID using specextract, and were binned to a minimum of 30 counts per channel. For each spectrum, weighted redistribution matrix files (RMFs) and weighted auxiliary response files (ARFs) were created using the ciao scripts mkacisrmf and mkwarf, respectively. The ARF contains information on the combined quantum efficiency (QE) of the detector as a function of energy averaged over time and the telescope/detector areas . The area (measured in $cm^2$) and the QE (measured in counts/photon) are multiplied together to create the ARF ($cm^2$ counts/photon). The RMF contains information on the mapping between physical properties of incoming photons like their energy, and their detected properties such as pulse height for a given detector, which are stored in a two dimensional matrix. The loss of area as a result of chip gaps and point sources was corrected by creating an exposure map for each observation with the mkexpmap command in CIAO. Each exposure map was weighted by the exposure time of each ObsID, summed, and then normalized by the total cleaned exposure time of all observations. These exposure maps were used to correct the previous background subtracted images, as shown in Figure 1.7. The mean value of the exposure map within the region of spectral extraction was taken as the suitable area correction and applied to the spectrum and background spectrum by setting the areascal keyword in the headers. All preceding steps within this section are necessary to produce a set of spectra that are prepared for model-fitting and subsequent analysis which are described in the next section.

### 1.2.3 Spectral Fitting

There are many different codes available that fit and model X-ray spectra to obtain projected gas properties of the ICM. Each spectrum is fit with an absorbed single temperature phabs(apec) model (Smith et al., 2001) in xspec version 12.9.1 (Arnaud, 1996). Spectra were fit using a $\chi^2$ minimization technique. The solar abundances were set to the values of Anders and Grevesse (1989). The hydrogen column density, $N_H$, were initially set to the galactic values of Kalberla et al. (2005) as shown in Table 1.1, but were allowed to vary. The redshift, $z$, was frozen to the value of the cluster, abundances, temperature, and model normalization were left free to vary. Density is related to the normalization of the apec thermal model through the emission integral,

$$\text{normalization} = \frac{10^{-14}}{4\pi\big(D_A(1+z)\big)^2}\int n_e n_H dV. \tag{1.14}$$

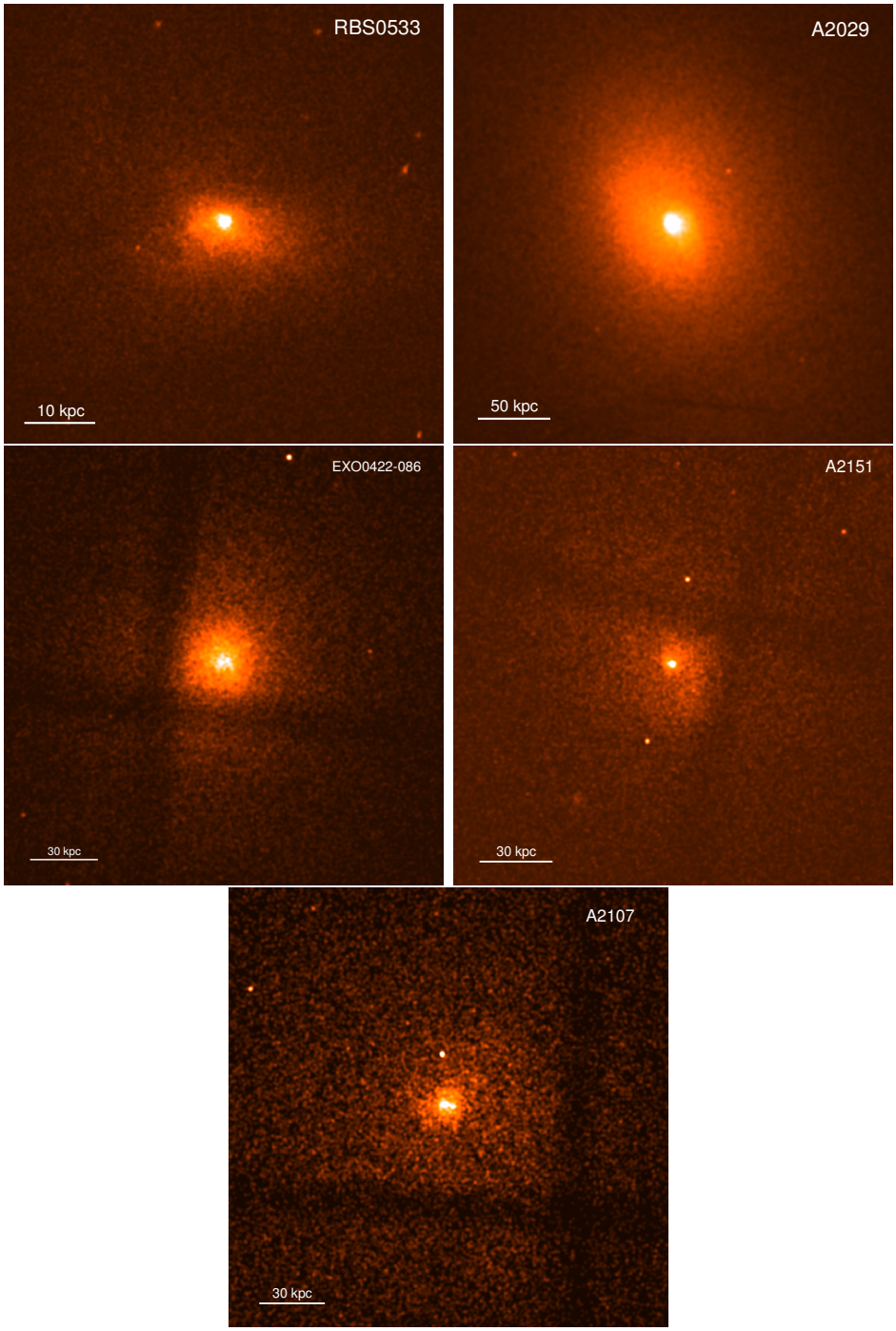


Figure 1.6: Each image is the same as in Figure 1.5 only they are background subtracted. Each image has also been Gaussian-smoothed with a 3 arcsec kernel radius.

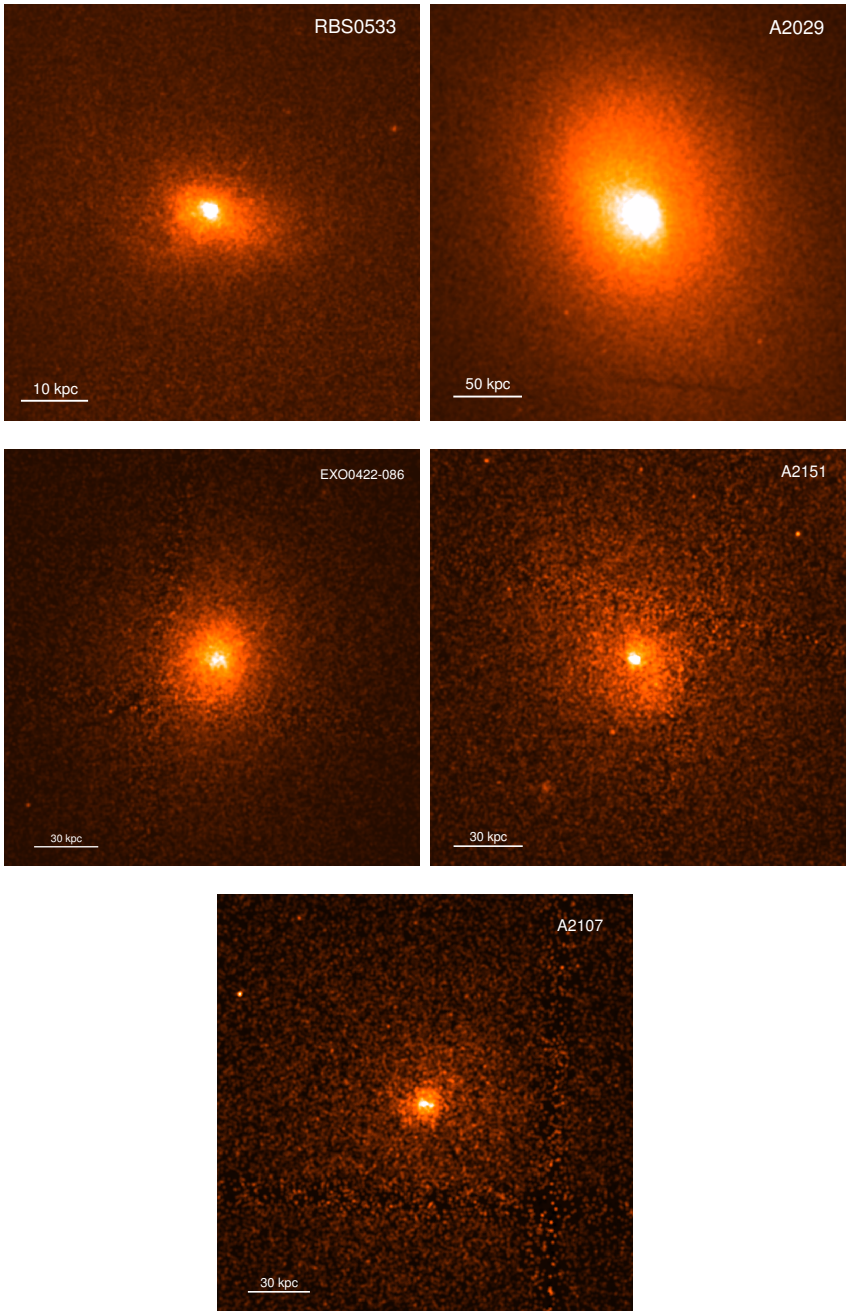


Figure 1.7: Each image is the same as in Figure 1.6 only they are exposure corrected to account for loss of area. Each image has also been Gaussian-smoothed with a 3 arcsec kernel radius. A clearly visible negative linear feature can be seen in A2029, which is due to the absorption by a foreground spiral galaxy (Clarke et al., 2004).

Here, $D_A$ is the angular diameter distance to the source, $n_e$ and $n_H$ are the electron and hydrogen number density, and $V$ is the volume of the annulus. Assuming hydrogen and helium mass fractions of X=0.75 and Y=0.24 (Anders and Grevesse, 1989), which gives $n_H = n_e/1.2$, and is assumed to be constant within each annulus. Another important property that can be determined via spectral fitting, is the X-ray luminosity, $L_X$, of the ICM. This was determined by modifying the previous model to PHABS×CFLUX(APEC). This allows us to obtain an estimate for the X-ray bolometric flux by integrating the unabsorbed thermal model between 0.1 and 100 keV. The resulting X-ray flux was then converted to the bolometric X-ray luminosity.

To summarize, after spectral fitting the following gas properties of the ICM are measured in each annulus: temperature, $kT$, metallicity, $Z$, model normalization, and bolometric X-ray luminosity, $L_X$. These are used to derive more gas properties of the hot atmosphere in Section 1.3.2 and Section 1.3.3.

## 1.3 Analysis

The analysis of the spoiler clusters begins with a study of the surface brightness profiles to identify any features in the ICM such as sloshing of hot gas, or depressions that are consistent with cavities in Section 1.3.1. In Section 1.3.2 we continue with our results from Section 1.2.3 to derive quantities using projected radial profiles. This is followed by a detailed deprojection analysis in Section 1.3.3. In Section 1.3.4, detailed steps are explained to obtain accurate mass profiles to measure the local free-fall times within each cluster.

### 1.3.1 Surface Brightness

Evidence for disturbances in the atmospheres which could be signatures of a bubble or cavity were investigated. Surface brightness (SB) profiles of the clusters were extracted from X-ray images, for a series of concentric annuli centered on the brightest pixel. After background subtraction, the resulting surface brightness profile may be fit with an isothermal $\beta$ model (Cavaliere and Fusco-Femiano, 1976; Branduardi-Raymont et al., 1981):

$$I_X = I_0[1 + (R/R_c)^2]^{-3\beta+1/2}, \tag{1.15}$$

where $I_0$ is the central surface brightness, $R_c$ is the core radius of gas distribution, and $\beta$ is the slope. Since an isothermal, single$-\beta$ model is a poor fit to the surface brightness

profiles, we instead fit the surface brightness profile with a double$-\beta$ model to account for the excess emission from the cool-core of the clusters,

$$I_X = I_1[1 + (R/R_{1,c})^2]^{-3\beta_1+1/2} + I_2[1 + (R/R_{2,c})^2]^{-3\beta_2+1/2}. \quad (1.16)$$

The surface brightness profiles are shown in Figure 1.8, where, the best fitting double$-\beta$ model parameters are shown in Table 1.2. This best-fitting model was subtracted from the X-ray images in Figure 1.7, and the difference is then divided by the model to produce the residual images shown in Figure 1.9. With the exception of RBS0533 which has a depression North of its centre, the remaining objects can easily be ruled out as having any clear bubbles. A more detailed analysis of this depression's significance will follow in Section 1.4.1, and other disturbances in the SB that can be explained by effects unrelated to AGN.

Several effects can cause disturbances in the brightness of the ICM. For instance, sloshing of intracluster gas can form cold fronts which create visible surface brightness discontinuities characterized by a sharp change in temperature and density (Markevitch and Vikhlinin, 2007). Cold fronts are created by halo interactions, which displace cool, dense intracluster gas from the centre of the potential well, and are directly related to spiral features seen in the ICM.

For instance, as a subcluster falls towards the main cluster, during it's passage through the pericenter the interaction of halos offsets gas in the main cluster core. This offset occurs during the subcluster's approach towards the main cluster, where the gravitational pull causes the main cluster's core to move towards the subcluster. However, the velocity field of the ICM surrounding the main cluster opposes this pull (Markevitch and Vikhlinin, 2007). While the halo of the main cluster can move towards the receding subcluster, the gas in main cluster is held back. After the subcluster emerges from the central region and continues to move away, the offset ICM will fall back towards the main cluster, and begin sloshing inside the potential well. The highest frequency of sloshing occurs on smaller scales, and so gas at a given radius moving in one direction will interact with gas on larger scales still moving in the opposite direction. The opposing flows will form cold fronts. While the subcluster passes through the main cluster core, at some radii it transfers angular momentum into the ICM, which allows sloshing features to take on a spiral form (Roediger, 2010).

Spiral features have been observed in many clusters, such as Perseus (Fabian et al., 2006), Virgo (Roediger et al., 2011), Centaurus (Sanders et al., 2016), and A2029 (Paterno-Mahler et al., 2013).

Roediger et al. (2012) performed hydrodynamic simulations to explore the nature and origin of sloshing spiral features in A496. They found that if a minor merger occurred

Table 1.2: The best fitting double$-\beta$ model parameters after fitting.

| Cluster | $I_1$ (counts/arcsec$^2$) | $R_{c,1}$ (arcsec) | $\beta_1$ | $I_2$ (counts/arcsec$^2$) | $R_{c,2}$ (arcsec) | $\beta_2$ | $\chi^2_{\rm red}$ (1) |
|---|---|---|---|---|---|---|---|
| A2029 | 835.5 | 0.35 | 0.22 | $-137.9$ | 80.4 | 0.22 | 2.4 |
| A2107 | 19.8 | 6.6 | 0.38 | $-10.9$ | $-11.7$ | 0.47 | 1.4 |
| A2151 | 38.4 | 2.2 | 0.5 | 4.5 | 26.6 | 0.40 | 1.3 |
| RBS0533 | 156.5 | 1.28 | 0.34 | 10.2 | $-42.9$ | 1.5 | 1.4 |
| EXO0422-086 | 20.6 | 9.9 | 0.46 | 7.04 | 21.7 | 0.46 | 1.4 |

**(1)**: The reduced $\chi^2$ after double$-\beta$ model fitting.

between A496 and a smaller, gas-free subcluster, and if the the initial fly-by was off-center, cool gas within the cluster could acquire angular momentum, preventing it from falling back into the centre. Cold fronts created in this simulation combined together to form the observed spiral features, which are not necessarily a result of recent mergers as Ascasibar and Markevitch (2006) have shown that such features can persist for several Gyrs. Evidence for sloshing features in the ICM were explored in the spoiler clusters.

In A2029, the cold fronts are clearly visible as a sharp change in SB as seen in the top left image of Figure 1.7. Our residual image of A2029, shown in Figure 1.9, reveals a continuous spiral feature directly associated with the cold front. Its spiral feature is the largest and most continuous one known, extending outward radially from the centre up to approximately 400 kpc (Paterno-Mahler et al., 2013). Similarly, A2151's residual image also reveals what appears to be a spiral feature. While not as prominent as A2029's sloshing feature, it extends radially outwards to at least 81 kpc. No clear evidence of sloshing was found in the remaining objects.

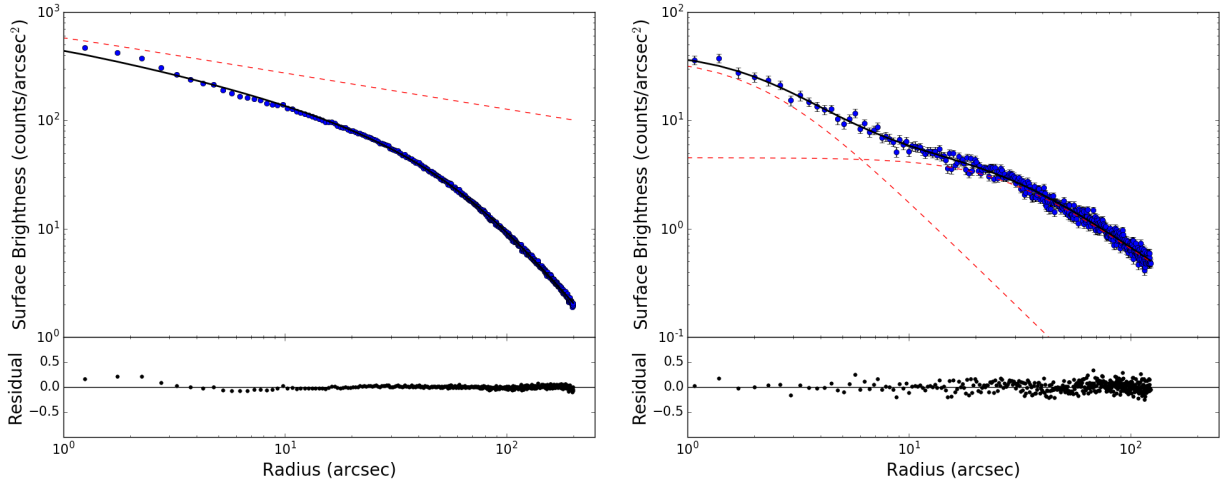


(a)




(b)

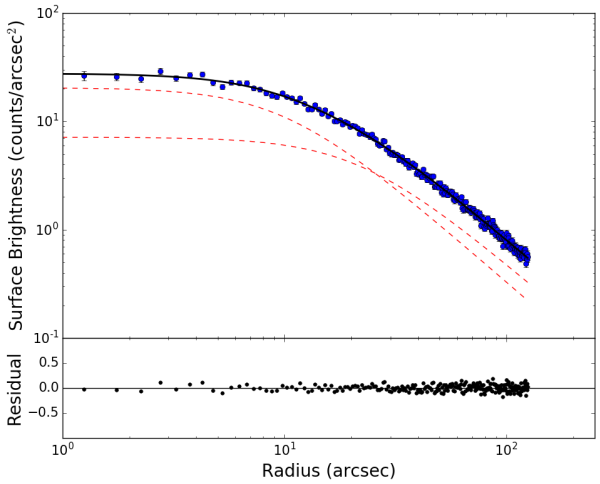


(c)

Figure 1.8: X-ray surface brightness profiles fit by an elliptical double-$\beta$ model. Blue points are the observed surface brightness profile, solid black line is the best fit obtained from double-$\beta$ model. Dashed red lines show the individual components of the double-$\beta$ model. Residual points are normalized by model values. Surface brightness profiles from top left to the bottom are: a) A2029, b) A2151, c) EXO0422-086. See Table 1.2 for details on fitting components.

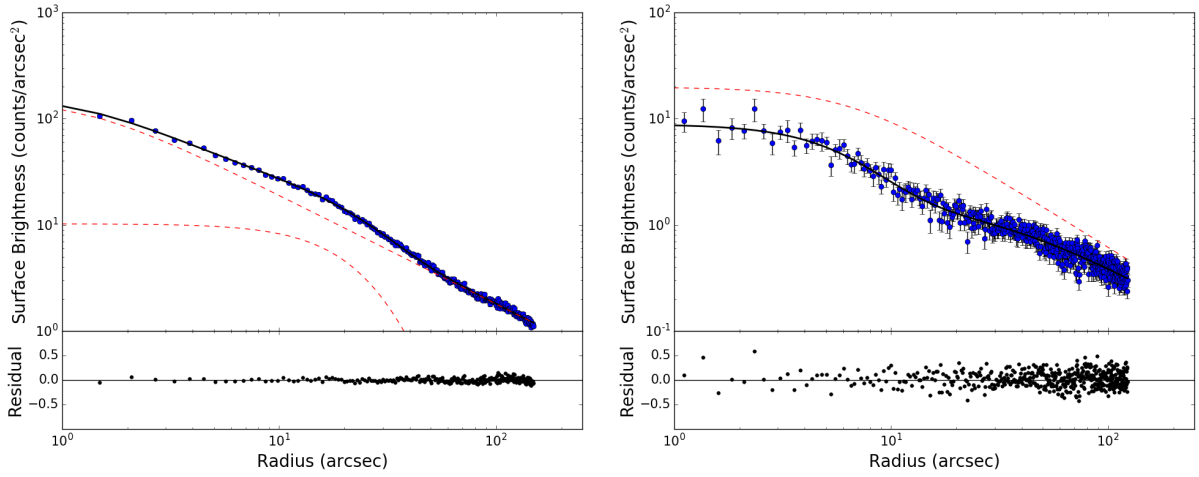


(d) (e)

Figure 1.8: Continued − Surface brightness profiles from left to right are: d)RBS0533, e) A2107. See Table 1.2 for details on fitting components.

### 1.3.2 Projected Profiles

In this section, we continue with the results from Section 1.2.3, and compute additional gas properties of the ICM using $n_e$ and $kT$, which will provide insight into the hot atmospheres of the cluster. The pressure and entropy index of the ICM are calculated as $p = 2n_e kT$ and $K = kTn_e^{-2/3}$, respectively. The cooling time, or the time it takes a parcel of gas to radiate away its thermal energy is computed as,

$$t_{\rm cool} = \frac{3}{2}\frac{p}{n_e {\rm n_H} \Lambda({\rm Z, T})} = \frac{3}{2}\frac{pV}{L_X} \tag{1.17}$$

where $\Lambda(Z,T)$ is the cooling function, that incorporates the contribution of important processes of X-ray emission (i.e. thermal bremsstrahlung emission) and depends on the temperature and solar abundance, $Z$, of the hot gas, as shown in Figure 1.10.

Finally, hot gas mass profiles are derived, $M = 2\mu_0 m_p n_e V$, where $m_p$ is the proton mass, and $\mu_0 = 0.62$, represents the mean molecular weight. The projected radial profiles are shown in Figure 1.11

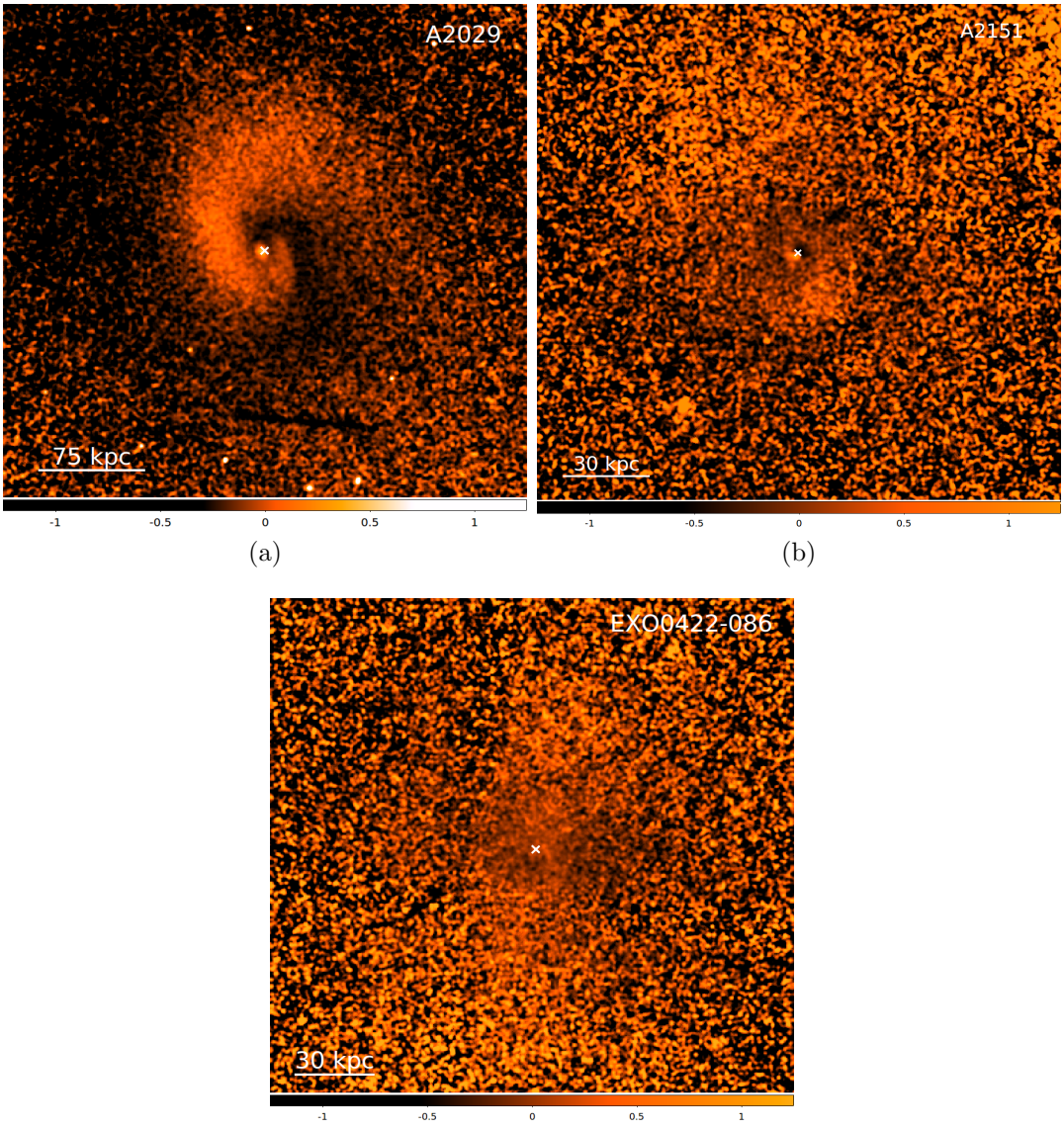


(a) (b)

(c)

Figure 1.9: Residual images of each cluster after double-$\beta$ model subtraction from Figure 1.7. Images were obtained by fitting a double $\beta$-model to the clusters surface brightness profile of the form in Equation 1.15. The white 'x' represents the location of the brightest pixel. Each image is exposure-corrected to account for loss of area and has also been Gaussian-smoothed with a 3 arcsec kernel radius. Residual Images are: (a) A2029, (b) A2151, (c) EXO0422-086.

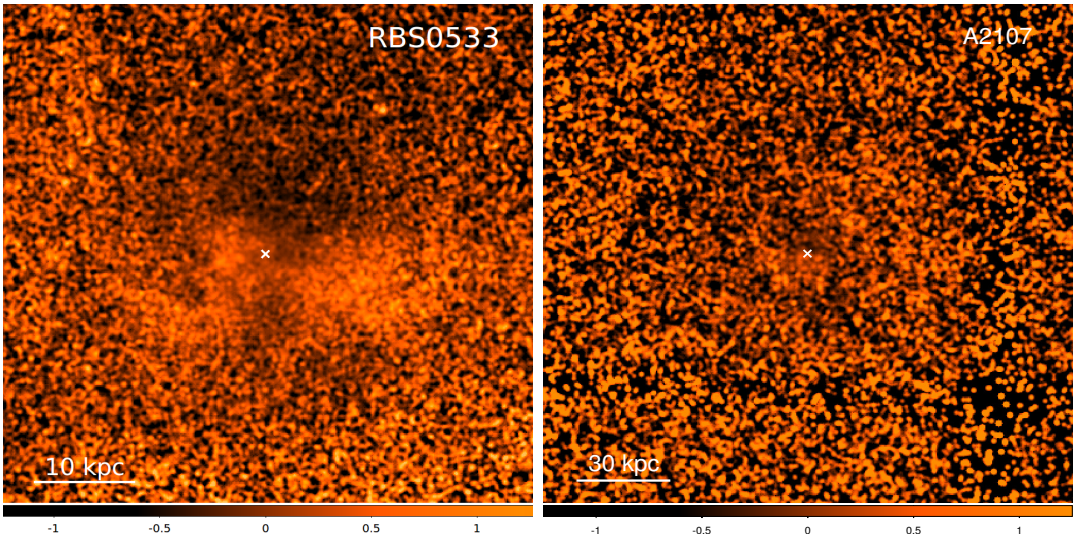


(d) (e)

Figure 1.9: Continued − Residual Images are: (d) RBS0533, (e) A2107. Clearly visible in RBS0533, are SB depression features to the North and South of the cluster centre, which may be potential X-ray cavities. The significance of these features are discussed in Section 1.4.1

### 1.3.3 Deprojected Profiles

In Section 1.2.3, spectra were extracted from regions of concentric annuli on the sky, where the temperature, density, and luminosity were assumed to be constant within each annulus. The projected foreground and background emission skews central-projected densities and temperatures to higher values. The reason for this is simply because the emission at any point in the sky is the superposition of emission from all points along the line-of-sight through the cluster. To derive accurate radial profiles of the inner regions of a cluster requires that spectra be "deprojected" to subtract off the contribution from the outer layers of the cluster. In this thesis, a model-independent deprojection routine which assumes only spherical geometry, called DSDEPROJ described in detail in (Sanders and Fabian, 2007; Russell et al., 2008). A brief description of this algorithm is now presented.

If we have $n$ number of annuli with spectra extracted from each annulus, and their corresponding blank-sky backgrounds, and if $j$ denotes the annulus that spectrums are extracted from, such that spectrums are extracted from j=1,2,...,n. Then, each projected spectrum, $\Upsilon_{\rm proj}[j]$, contains information about the photon count rate within an individ-

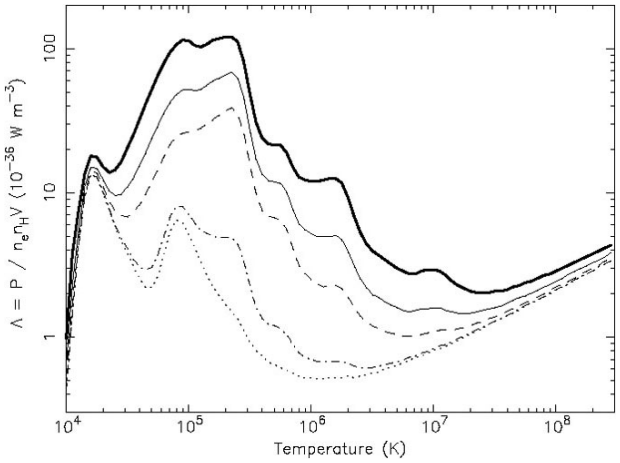


Figure 1.10: Cooling function for given temperatures assuming the plasma is optically thin and that no external radiation affects the ionization balance (collisional ionization equilibrium) taken from (Kaastra et al., 2008). The different lines reflect different metallicities relative to the solar value, $Z_\odot$, from top to bottom the lines are: 1 $Z_\odot$, 0.3 $Z_\odot$, 0.1 $Z_\odot$, and 0.001 $Z_\odot$

ual annulus, as a function of the spectral energy bin, such that $\Upsilon_j$ contains information about the count rate in the $j$-th annulus. The outermost annulus is assumed to have an uncontaminated spectrum, $\Upsilon_{\rm deproj}[n] = \Upsilon_{\rm proj}[n]$.

The algorithm starts on the outer most annulus, and works its way inwards. The count rate per unit volume is determined for the n-th annulus, and is scaled by the projected volume of the neighbouring inner annulus and is then subtracted from the count rate of this neighbouring annulus,

$$\Upsilon_{\rm deproj}[n-1] = \Upsilon_{\rm proj}[n-1] - \frac{V_{\rm proj}[n, n-1]}{V_{\rm total}[n]}\Upsilon_{\rm deproj}[n] \tag{1.18}$$

Here, $V_{\rm total}[n]$ is the total projected volume of the n-th annulus, $V_{\rm proj}[j,k]$ is the projected volume of the $k$-th annulus onto the $j$-th annulus. Generalizing this equation:

$$\Upsilon_{\rm deproj}[j] = \Upsilon[j] - \sum_{k=j+1}^{n} \frac{V_{\rm proj}[k,j]}{V_{\rm total}[k]}\Upsilon_{\rm deproj}[k] \tag{1.19}$$

Where j iterates from $n-1, ..., 1$. A Monte Carlo technique is then used to calculate the uncertainties in the count rate of each spectrum. This will then produce a set of

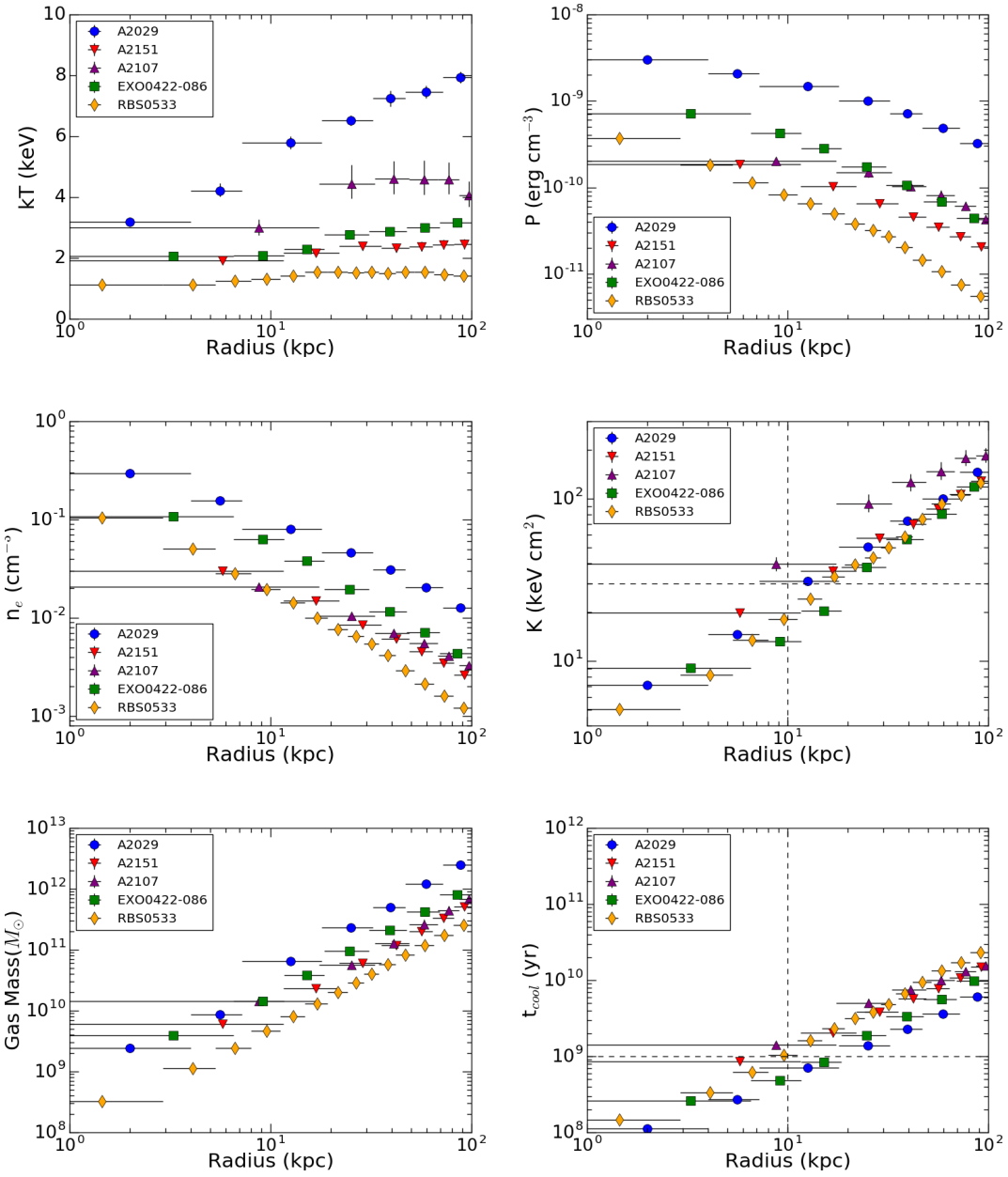


Figure 1.11: Projected temperature, pressure, density, entropy, gas mass, and cooling time profiles. The dashed horizontal lines represent the thresholds for the cooling time ($t_{\rm cool} = 1.0 \times 10^9$ yr) and entropy (K= 30 keV cm$^2$).

deprojected spectra that can be fit by models. Deprojected radial profiles can be obtained for deprojected spectra by following the same analysis in Section 1.2.3, which are shown in Figure 1.12.

### 1.3.4 Mass Models

In this Section, mass profiles are generated for each system, which are then used to determine the total cluster mass, gravitational acceleration, and free-fall times. The procedure is explained in Hogan et al. (2017a) for determining the gravitating mass profiles are adopted in this thesis. In Section 1.3.5 the mass profiles are fit to the spectra obtained in Section 1.2.2.

The methodology of Hogan et al. (2017a) to obtain mass profiles for a small sample of galaxy clusters, is in good agreement with the total cluster mass measurements on large and small scales. For instance, the total cluster mass of Hydra-A agrees well with calculations obtained with velocity dispersion measurements of the cluster core using HyperLeda at small radii (Hamer et al., 2014). At larger radii, it also agrees well with total mass measurements from weak-lensing (Okabe et al., 2016), and from profiles which assume only hydrostatic equilibrium using a Navarro-Frenk-White (NFW) potential (Main et al., 2017). The model consists of an NFW potential and a cored isothermal potential. The former has been shown to be an accurate description of the total gravitating potential of cluster masses on large scales (e.g. Pointecouteau et al., 2005; Vikhlinin et al., 2006) and takes the form of

$$\Phi_{\rm NFW}(R) = -4\pi G\rho R_s^2 \frac{\ln\left(1+R/R_s\right)}{R/R_s}, \tag{1.20}$$

where $\rho$ is the characteristic gas density and $R_s$ is the scale radius. Although the NFW profile provides a reasonable fit on large scales, its contribution alone underestimates masses inferred from stellar velocity dispersion due to the central galaxy (e.g. Fisher et al., 1995; Lauer et al., 2014; Hogan et al., 2017a). Thus, a cored isothermal potential is needed to account for this, given by

$$\Phi_{\rm ISO}(R) = \sigma_*^2 \ln\left(1+(R/R_I)^2\right). \tag{1.21}$$

Here $\sigma_*$ is the stellar velocity dispersion and $R_I$ is the isothermal scale radius which is used solely to prevent the gravitational acceleration from diverging from $R \to 0$, is chosen to be smaller than the scales of interest. The combined NFW and cored isothermal potential, dubbed ISONFWMASS, is implemented as an XSPEC extension in the package CLMASS (Nulsen et al., 2010). The model assumes the cluster atmosphere is spherically symmetric

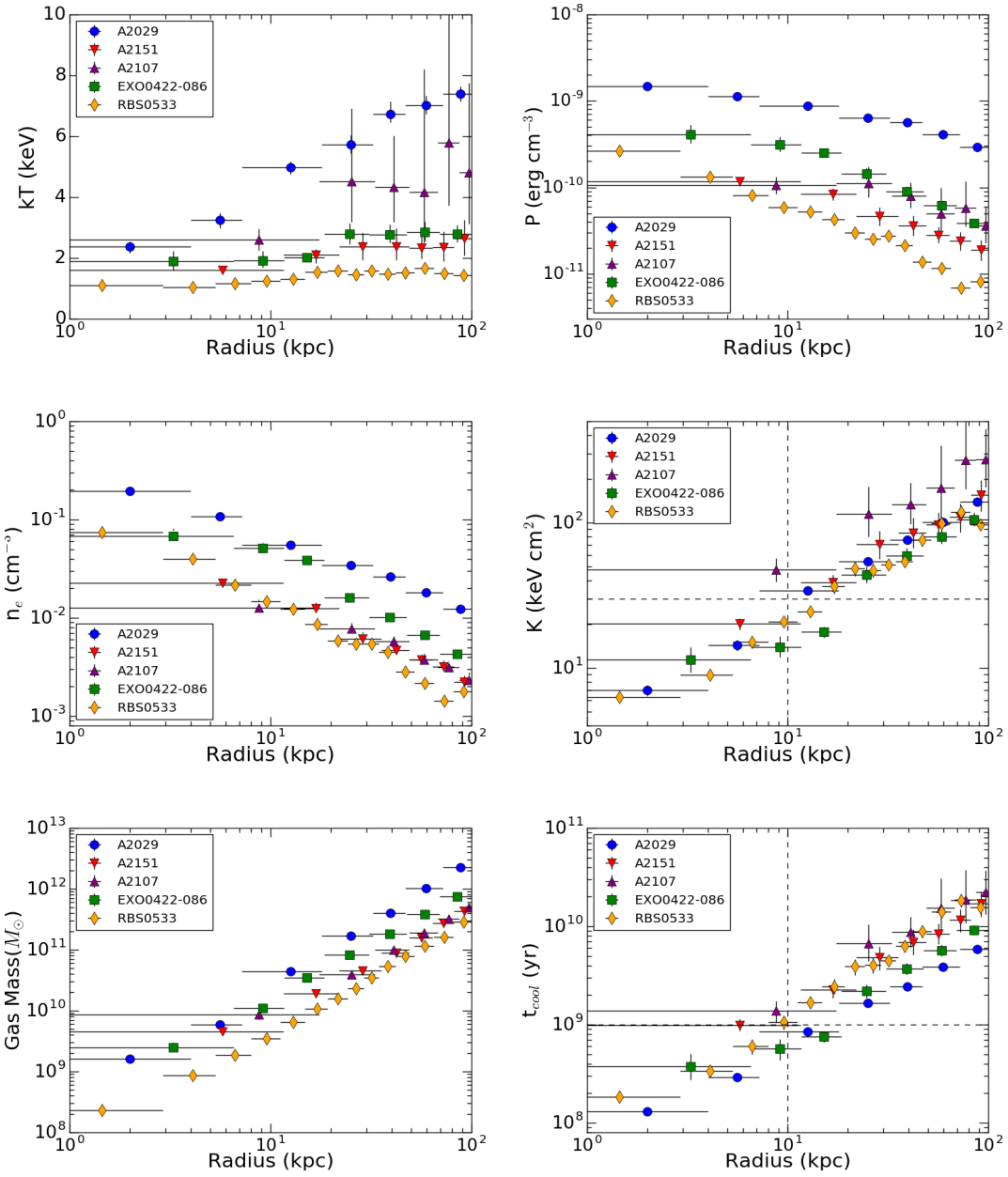


Figure 1.12: Deprojected temperature, pressure, density, entropy, gas mass, and cooling time profiles. The dashed horizontal lines represent the thresholds for the cooling time ($t_{cool} = 1.0 \times 10^9$ yr) and entropy (K= 30 keV cm$^2$).

and in hydrostatic equilibrium. In the next section, the fitting procedure is explained in detail, and mass and free-fall time radial profiles are derived.

### 1.3.5 Spectral Fitting of Mass Profiles

The stellar velocity dispersion is determined here using a velocity dispersion derived from the 2-Micron ALl Sky Survey (2MASS) K-band magnitude (2.17 $\mu$m). The K-band or the near-infrared (NIR) is a good tracer of the total stellar mass within a galaxy and is more insensitive to dust than are optical or ultraviolet tracers. In this thesis, the stellar velocity dispersion's found by Pulido et al. (2018) is adopted for A2029 and A2151. The methodology for obtaining such measurements is as follows.

The K-band luminosity is measured in the BCG which is extinction-corrected to account for absorption and scattering by gas and dust in the interstellar medium. Moreover, these observations have K-corrections to account for changes in the luminosity and colour of the galaxy between the time the light was emitted and the time the light is observed. The K-band luminosity is measured at the isophotal radius, $R_{K20}$, the radius where the surface brightness reaches 20 mag/arcsec$^2$. The enclosed stellar mass is calculated at this radius, and the equivalent stellar velocity dispersion is computed assuming a potential of the form in Equation 1.21. This velocity dispersion is the inferred velocity dispersion measured at $R_{\rm K20}$ if the BCG consisted only of stars (Hogan et al., 2017a). For A2107, RBS0533, and EXO0422-086, no K-band measurements of their BCG's exist, so values were adopted from the HyperLEDA database (Makarov et al., 2014) for the former two. A value of 250 km s$^{-1}$ was adopted for EXO0422-086 (Voit and Donahue, 2015b) which has neither HyperLEDA or K-band measurements available.

An ISONFWMASS(PHABS$\times$APEC) model are used to fit to spectra obtained in Section 1.2.2. Stable fits were found by freezing the redshift to the value of the cluster, freezing $\sigma_*$ to its inferred value described above. All remaining parameters were allowed to vary throughout fitting.

To compute the uncertainties in the NFW scale radius, $R_{\rm s}$, and the NFW potential, $\rm A_{NFW} = 4\pi\mu G\rho R_s^2$, XSPEC was used to create a Markov chain Monte Carlo (MCMC) simulation of 5000 iterations. The $1\sigma$ standard deviation is adopted as the uncertainty of the parameters, as well as in the mass profiles. The radial mass profiles for these clusters takes the form of the sum of the isothermal and NFW components respectively:

$$M_{\rm ISO} = \frac{2\sigma_*^2 R}{G}, \tag{1.22}$$

$$M_{\rm NFW} = 4\pi\rho R_S^3 \left[ \log\left(\frac{R_S + R}{R_S}\right) - \frac{R}{R_S + R} \right]. \tag{1.23}$$

The total cluster mass can then be computed at $R_{2500}$, the radius where the mean density is 2500 times that of the critical density, $\rho_c$,

$$M_{2500} = \frac{4\pi R_{2500}^3}{3}\bar{\rho}, \tag{1.24}$$

where $\bar{\rho} = 2500\rho_c$. The best fitting parameters are shown in Table 1.3. The ratio of cooling time to free-fall time is believed to be related to the thermally unstable cooling (Nulsen, 1986; Pizzolato and Soker, 2005a; McCourt et al., 2012), as such free-fall time profiles are derived for each object. The enclosed mass profiles obtained from fitting are used to calculate the local gravitational acceleration, $g = GM/R^2$, which can be used to calculate $t_{\rm ff}$:

$$t_{\rm ff}(R) = \sqrt{\frac{2R}{g}}. \tag{1.25}$$

The enclosed cluster mass profiles are shown in Figure1.13 and the free-fall time and $t_{\rm cool}/t_{\rm ff}$ profiles are shown in Figure 1.14. The minimum $t_{\rm cool}/t_{\rm ff}$ values lie between $20-50$, with A2029 residing at the lower end of this range and A2107 being at the higher end. The $\min(t_{\rm cool}/t_{\rm ff})$ agrees within a $1\sigma$ error for values calculated for A2029 (Hogan et al., 2017a; McNamara et al., 2016), A2151 (Pulido et al., 2018), and A2107 (Hogan et al., 2017a).

## 1.4 Quantitative Analysis

While inspection of images in Figure 1.7 and Figure 1.9 reveal that only RBS0533 has any obvious signs of a bubble, the remaining clusters, while appearing more relaxed than RBS0533, cannot be definitively ruled out. Indeed, cavities may exist in these systems but remain undetected. In Section 1.4.1 a method of searching for and quantifying the size of X-ray bubbles is introduced and used to confirm the existence of a cavity candidate North of RBS0533's centre which is evident as a depression in Figure 1.9. This method can can also be used to confirm the significance of structure in clusters, including sloshing features. In Section 1.4.2 a discussion on undetected cavities in clusters of galaxies follows, which discusses the detection rate in larger samples and addresses the inherent biases in sample selection.

Table 1.3: Mass Fitting Parameters

| Cluster | $\sigma_*$ (km s$^{-1}$) (1) | $A_{\rm ISO}$ (keV) (2) | $R_s$ (arcmin) (3) | $A_{\rm NFW}$ (keV) (4) | $R_{2500}$ (kpc) (5) | $M_{2500}$ ($10^{14}$ M$_\odot$) (6) |
|---|---|---|---|---|---|---|
| A2029 | $336 \pm 10^a$ | 0.694 | $5.35^{+0.39}_{-0.28}$ | $86.5^{+4.6}_{-4.2}$ | 693.4 | $5.1^{+0.20}_{-0.18}$ |
| A2151 | $219 \pm 4^a$ | 0.295 | $1.87^{+0.29}_{-0.13}$ | $9.7^{+0.5}_{-0.4}$ | 259.2 | $0.26^{+0.01}_{-0.01}$ |
| A2107 | $314 \pm 25^b$ | 0.608 | $6.32^{+1.80}_{-0.88}$ | $26.8^{+7.1}_{-3.5}$ | 414.6 | $1.05^{+0.22}_{-0.23}$ |
| RBS0533 | $306 \pm 14^b$ | 0.575 | $13.8^{+9.0}_{-5.4}$ | $4.3^{+2.3}_{-1.4}$ | 228.3 | $0.17^{+0.02}_{-0.02}$ |
| EX0422-086 | $250 \pm 15^c$ | 0.384 | $1.17^{+0.24}_{-0.17}$ | $12^{+0.91}_{-0.72}$ | 279.5 | $0.32^{+0.03}_{-0.03}$ |

**Note.** Columns are: (1) Equivalent stellar velocity dispersion, (2) Isothermal potential given by, $A_{\rm ISO} = \mu_0 m_p \sigma_*^2$, (3) NFW scale radius, (4) NFW potential given by, $A_{\rm NFW} = 4\pi\mu_0 m_p G\rho R_s^2$, (5) $R_{2500}$, (6) $M_{2500}$.
[a] $\sigma_*$ inferred from 2MASS isophotal K-band magnitude measurements.
[b] $\sigma_*$ measurements from HyperLEDA.
[c] Assuming $\sigma_* = 250$ km s$^{-1}$, following Voit and Donahue (2015b)

### 1.4.1 Surface Brightness Variations in the ICM

X-ray cavities typically have a surface brightness deficit of about $20-30\%$ relative to the surrounding medium. However, in Panagoulia et al. (2014), they showed that $\sim 20000$ counts within 20 kpc of the core is required for clear cavity detections. Only A2029, RBS0533, and EXO0422-086 satisfy this criteria. Calzadilla et al. (2018) studied the surface brightness fluctuations in A1664 to determine if two depressions surrounding the BCG are cavities or are due to noise. Through significance tests, they determined that the regions were significant fluctuations, and thus cavities.

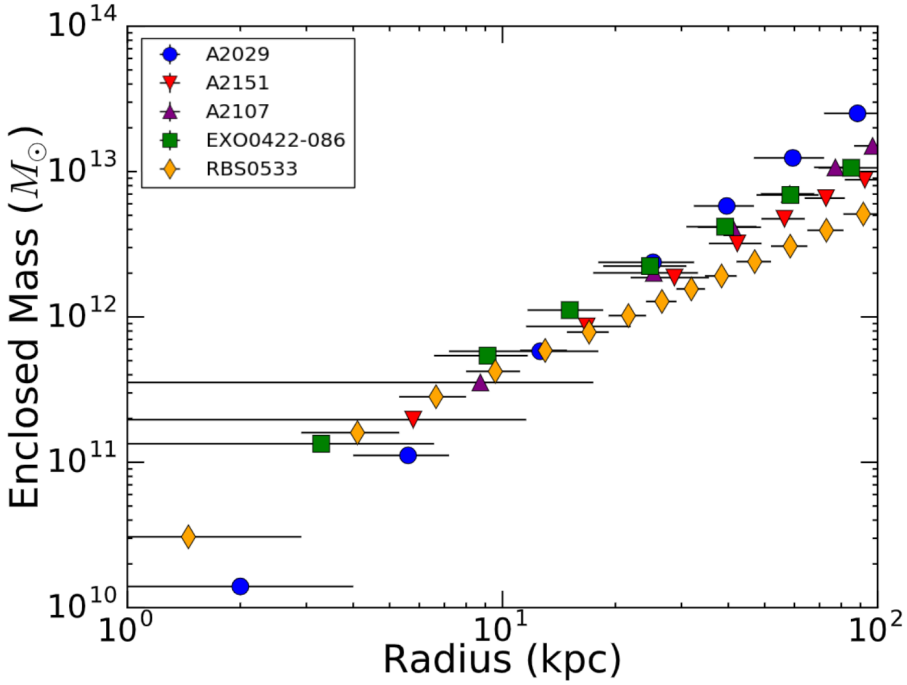


Figure 1.13: Enclosed mass within R, given by $M(< R) = M_{\rm ISO} + M_{\rm NFW}$ which were obtained from fitting, see text and Table 1.3.

In this Section, surface brightness fluctuations are investigated by comparing the counts in the images of Figure 1.7, $N_I$, to the counts in the best fitting $\beta-$model image, $N_M$. The model represents the undisturbed cluster atmosphere. The residual images in Figure 1.9 were used as a reference point for the location of potential bubbles in the ICM. Circular regions of radius $r$ were overlaid over these depressions at distance $R$ from the centre, and the signal-to-noise ratio, SNR, was calculated in these regions to determine their significance. The signal within each generated region is calculated as,

$$|S| = |N_I - N_M| \tag{1.26}$$

and the SNR within a region is given by,

$$\mathrm{SNR} = \frac{|\mathrm{S}|}{\sqrt{|\mathrm{S}| + 2\mathrm{N_M}}}. \tag{1.27}$$

$\mathrm{N}_M$ is calculated by fitting a double $\beta-$model and single $\beta-$model to the surface brightness profiles with both elliptical and circular annuli. Residual images reveal one

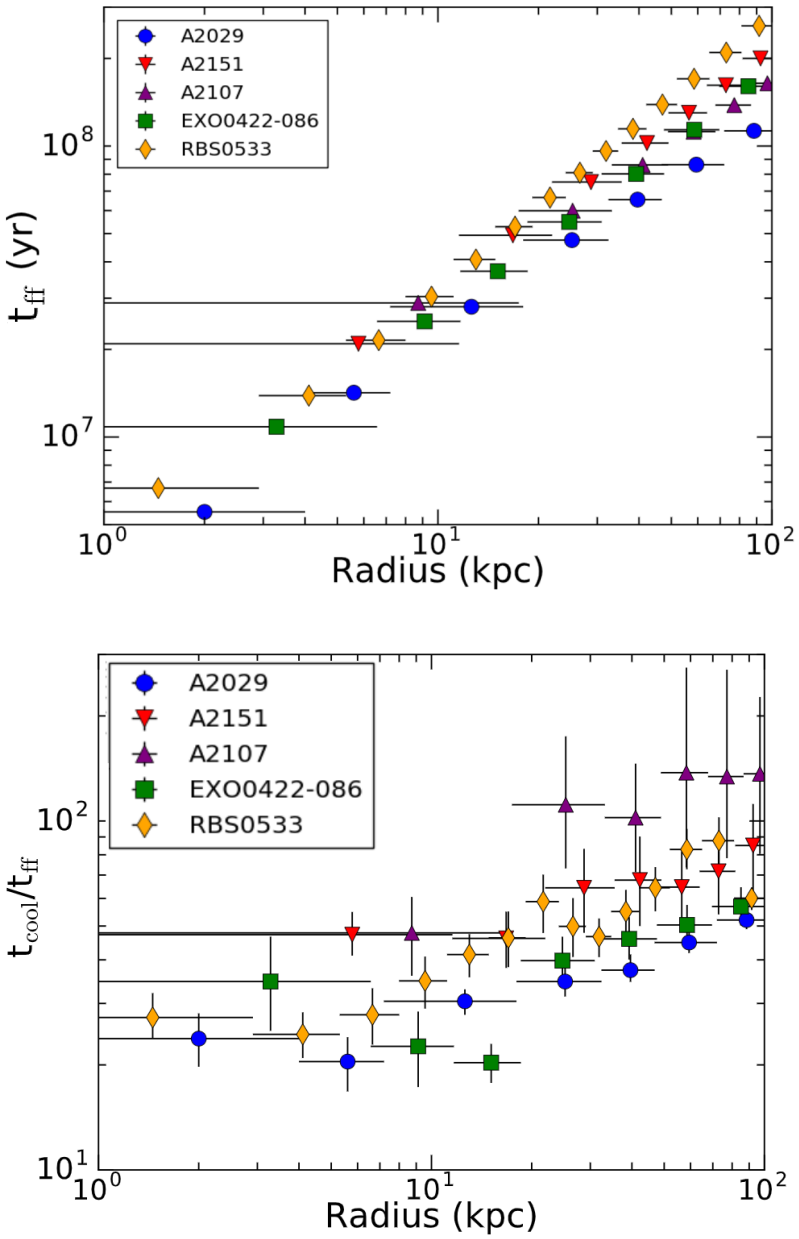


Figure 1.14: Top panel: Free-fall time profiles calculated using Equation 1.25. Bottom panel: The ratio of cooling time to free-fall time, the $\min(t_{\rm cool}/t_{\rm ff})$ lie between 20-50.

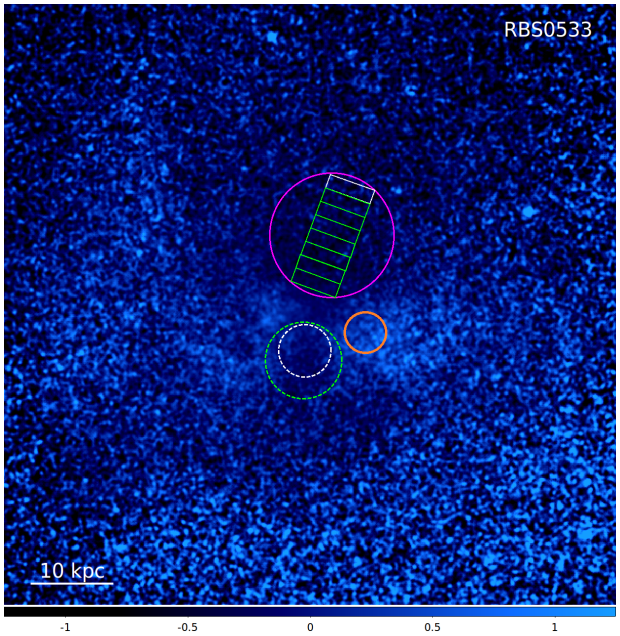


Figure 1.15: Model subtracted relative residual image of RBS0533 (same as in Figure 1.9) given by $(N_I - N_M)/N_M$. Overlaid are circular regions used in significance testing, see Table 1.4, where the magenta circle is the approximate location and size of an X-ray bubble. Since the bubble has no clear rims, rectangular regions are used to find the approximate edge of a bubble where its structure is barely detected (SNR $< 5$) which corresponds to the white rectangle, see text for more detail. This image is Gaussian-smoothed with a 3 arcsec kernel radius.

cluster, RBS0533, possesses bubble-like structure to the North of its centre. Since this bubble has no rims, making size estimates difficult, the size of the bubble was determined by calculating the SNR where the structure fades into the background (SNR $< 5$).

This was done by overlaying box regions with fixed length and width, corresponding to 5.7 kpc and 1.7 kpc, respectively. Regions are placed in succession of one another moving radially outwards from the centre, beginning at roughly 2.5 kpc where the depression is visible, see Figure 1.15. At approximately $R = 20$ kpc (the edge of white the rectangle), the SNR falls below 5. Since the shape of the bubble is also unknown, the bubble is estimated as being spherically symmetric which encloses the boxed regions (magenta circle), with size, $r = 7.5$ kpc, at distance $R = 10$ kpc from the centre.

One can obtain an estimate for the total energy required to inflate a bubble in the ICM,

which is given by its enthalpy,

$$E = \frac{\gamma}{\gamma - 1} pV, \tag{1.28}$$

where $p$ is the pressure of the cavity, $V$ is the volume of the cavity, and $\gamma$ is the ratio of specific heat capacities, which is 4/3 for a relativistic gas and 5/3 for a non-relativistic monatomic gas. Throughout this analysis, the cavity is assumed to be filled by a relativistic ideal gas, so $E = 4pV$. As mentioned in Section 1.1.3, the age of a bubble is best represented by the buoyancy time scale, $t_{\rm buoy}$, which is given by, (Bîrzan et al., 2004; Vantyghem et al., 2014),

$$t_{\rm buoy} \simeq R\sqrt{\frac{SC}{2gV}}, \tag{1.29}$$

where $S$ is the bubble's cross-section, $V$ is the volume of the bubble, $g$ is the local gravitational acceleration, and $C = 0.75$ is the drag coefficient (Churazov et al., 2001). The gravitational acceleration is estimated as $g = GM(< r)/R^2$, where $M(< r)$ is the total mass found in Section 1.3.5. The buoyancy time of the bubble then is $\sim 1.37 \times 10^7$ yr, which can be used to calculate the jet power, or mechanical power of the AGN that would be required to inflate a bubble of this size, given by:

$$P_{\rm jet} = \frac{4pV}{t_{\rm buoy}}. \tag{1.30}$$

For a cavity of radius $r = 7.5$ kpc at distance $R = 10.1$ kpc, the jet power is $3.9 \pm 0.2 \times 10^{43}$ erg s$^{-1}$. The SNR for the deficit in this circular region and for the other circular regions of interest marked in Figure 1.15. The best fit single and double $\beta-$model for elliptical and circular annuli are used to determine the deficits in these regions and the SNR is calculated within each region using Equation 1.27. The details of this are given in Table 1.4. Dashed colour regions to the South of the centre were found to be insignificant, and correspond to an excess of roughly 6% at most for the single circular $\beta-$model and a deficit close to 2% relative to the double elliptical $\beta-$model. There are discrepancies between the circular and elliptical double $\beta-$model for the larger dashed-green region. The SNR is relatively low for all models in these regions, which suggests that the structure observed within these regions is likely not real, or rather, it may be an artifact from the model.

The orange circle to the West of the centre is a region of excess, which reaches levels of about 39% and 47% relative to the model corresponding to SNRs of 13 and 15 for an elliptical and circular double $\beta-$model, respectively. This indicates that this structure is likely a real feature.

Table 1.4: **Signal-to-noise ratio for regions in RBS0533 fit with an elliptical $\beta-$model and circular $\beta-$model.**

| | | | Elliptical model | | | | Circular Model | | | |
|---|---|---|---|---|---|---|---|---|---|---|
| Region Colour | R | r | Single $\beta-$model | | Double $\beta-$model | | Single $\beta-$model | | Double $\beta-$model | |
| | (kpc) | (kpc) | Deficit (%) | SNR | Deficit (%) | SNR | Deficit (%) | SNR | Deficit (%) | SNR |
| (1) | (2) | (3) | (4) | (5) | (4) | (5) | (4) | (5) | (4) | (5) |
| Magenta | 10.1 | 7.5 | -29.4 | 26.0 | -31.0 | 27.6 | -28.5 | 25.1 | -30.0 | 26.6 |
| Dashed White | 4.5 | 3.2 | +2.5 | 1.6 | -2.4 | 1.6 | +5.1 | 3.1 | -0.2 | 0.1 |
| Dashed Green | 5.6 | 4.6 | +3.9 | 3.1 | -0.4 | 0.31 | +6.4 | 5.1 | +2.0 | 1.7 |
| Orange | 8.6 | 2.5 | +47.3 | 14.8 | +39.2 | 12.8 | +54.6 | 16.4 | +47.2 | 14.8 |

**Columns**: (1) Region Colour in the Figure 1.15, (2) Distance away from the cluster centre, (3) Size of region, (4) deficit of image relative to model ($N_I/N_M - 1$), (5) SNR given by Equation 1.27.

The region to the North of the centre is a significant depression. The magenta circle of size $r = 7.5$ kpc at a distance of $R = 10$ kpc, has a deficit reaching the levels of 31% with a SNR of $\sim 28$. This agrees fairly well across the elliptical and circular $\beta$-models and clearly shows that the structure encompassed by the circle is most likely real. Moreover, the surface brightness deficit within this region, for all of our models, is consistent with what is expected for a bubble relative to its surroundings.

The remaining clusters do not have significant structure associated with AGN feedback. Excluding A2029 and A2151, depressions in the images never dropped below 15%. Any significant depressions in these two clusters are mostly, in part, due to sloshing of intracluster gas. The sloshing feature in A2029 has a SNR $> 20$, making it a conclusive detection, whereas the sloshing feature in A2151 has a SNR $\lesssim 5$, making its detection uncertain.

### 1.4.2 Undetected Cavities

Excluding RBS0533, cavities may exist in these systems, but remain undetected. Several studies have investigated the statistical properties of cluster cavities that are drawn from the *Chandra* archive. One such survey found a cavity detection frequency of 41% for a sample size of 75 clusters (Bîrzan et al., 2012), while a sample of 133 systems biased towards cool-core clusters found a detection rate of 52% (Shin et al., 2016).

In the brightest 55 clusters sample (B55), it was shown by Dunn and Fabian (2006) that 20 of these clusters require heating to offset cooling. At least 14 of the 20 clusters have clear bubbles and only one of these does not harbour a central radio source.

Finally, Dunn and Fabian (2008) studied the 42 clusters from the B55 and brightest cluster samples with *Chandra* data. Of those, 23 have a central radio source. Defining cooling flow clusters as those with a significant central temperature drop and a short central cooling time, they found that 14 of the 42 clusters meet these criteria and 6 of those harbour bubbles.

Among the factors that govern the detection of cavities, high central surface brightness favours their detection in cool cores. Bîrzan et al. (2012) used simulation to define the properties of bubbles that remain undetected. They concluded that most bubbles are undetected when the angle between the bubble-to-core axis and line of sight is small, or when they lie at large distances from the core.

Although only one of the five objects in this sample have a possible X-ray bubble, excluding A2107, each of them possesses a central radio source as shown overlaid in Figure 1.16. The distribution of radio powers for this sample is consistent with expectations for cool core clusters (Hogan et al., 2015).

## 1.5 Uplifted Gas

Chemical enrichment of the ICM is thought to have occurred at earlier times, primarily from type II and type Ia supernovae (SNe) (Sato et al., 2007), where the former is responsible for the creation of $\alpha$ elements (i.e. O, Mg, Si, Ca, etc) and the latter primarily creates the heaviest elements such as iron. The ejecta from SNe raised the heavy element abundance of the ICM to an average of 1/3 of the solar value (Mushotzky et al., 1996; Mushotzky and Loewenstein, 1997). Although in cool-core clusters within the vicinity of the BCG, metallicities often rise approaching solar values (Allen and Fabian, 1998; Fukazawa et al., 1994; De Grandi et al., 2004). Gas in cool-cores has likely been enhanced by stars associated with BCGs, which means its metallicity distribution should reflect the distribution of light.

However, several studies have also shown that the metal abundance of type Ia ejecta have different radial distributions than the stellar light profiles of BCGs (Rebusco et al., 2005; David and Nulsen, 2008). Under the assumption that heavy elements are produced primarily by stars, this implies that ejecta are displaced from the galaxies by a different mechanism. The most likely mechanism is turbulence induced by mergers (Sharma et al., 2009), or outflows from AGN (Kirkpatrick et al., 2009).

In this Section, evidence for uplifted gas from AGN outflows are investigated in the spoiler clusters. In Section 1.16, two-dimensional metallicity maps for the clusters are created to investigate the distribution of abundance in the spoiler clusters. In Section 1.5.2 thermodynamic profiles are extracted along the direction of radio jets, and in a direction that is not aligned with these jets to explore the possibility of uplift. In Section 1.5.3, statistical tests are performed on the profiles extracted in Section 1.5.2, to further constrain conclusions on any observed trends in abundance.

### 1.5.1 Metallicity Maps

To search for uplifted gas in our clusters, metallicity maps are first created using the contour binning algorithm, CONTBIN (Sanders, 2006). Cluster images were binned using a minimum signal-to-noise ratio (SNR) of 70 per bin to maximize the number of bins generated while retaining high enough count rates that uncertainties in metallicity do not dominate. No attempts were made to create maps for A2107 as its exposure time is too short, and thus its low number of counts would not allow us to generate enough bins with the required SNR for any meaningful analysis.

Spectra were extracted within each bin and fitted with a PHABS(APEC) model. Temperature, metallicity, and normalization were allowed to vary. Column densities were frozen at the value obtained from the LAB Survey (Kalberla et al., 2005). The resulting metallicity maps are shown in Figure 1.16

Higher metallicity gas aligned parallel and antiparallel to the jet axis is a strong indicator of metal-enriched gas being uplifted. The slightly asymmetric map near the centre of RBS0533 hints to this mechanism without being prominent enough to be deemed significant.

It is difficult to draw conclusions about A2151 and EXO0422-086. On one hand, it appears that higher metallicity gas appears to lie along the jet axis as seen in Figure 1.16. On the other hand, spatial bins in these clusters are considerably larger than in abundance maps of A2029 and RBS0533. Thus, it is difficult to see variations in abundances, as larger radial bins will tend to average away any small scale fluctuations in metallicity in the ICM (Kirkpatrick and McNamara, 2015). Moreover, the exposure time of these clusters (especially EXO0422-086) is shallow in comparison to RBS0533, which makes it harder to generate smaller bins with a high enough SNR that uncertainties do not dominate.

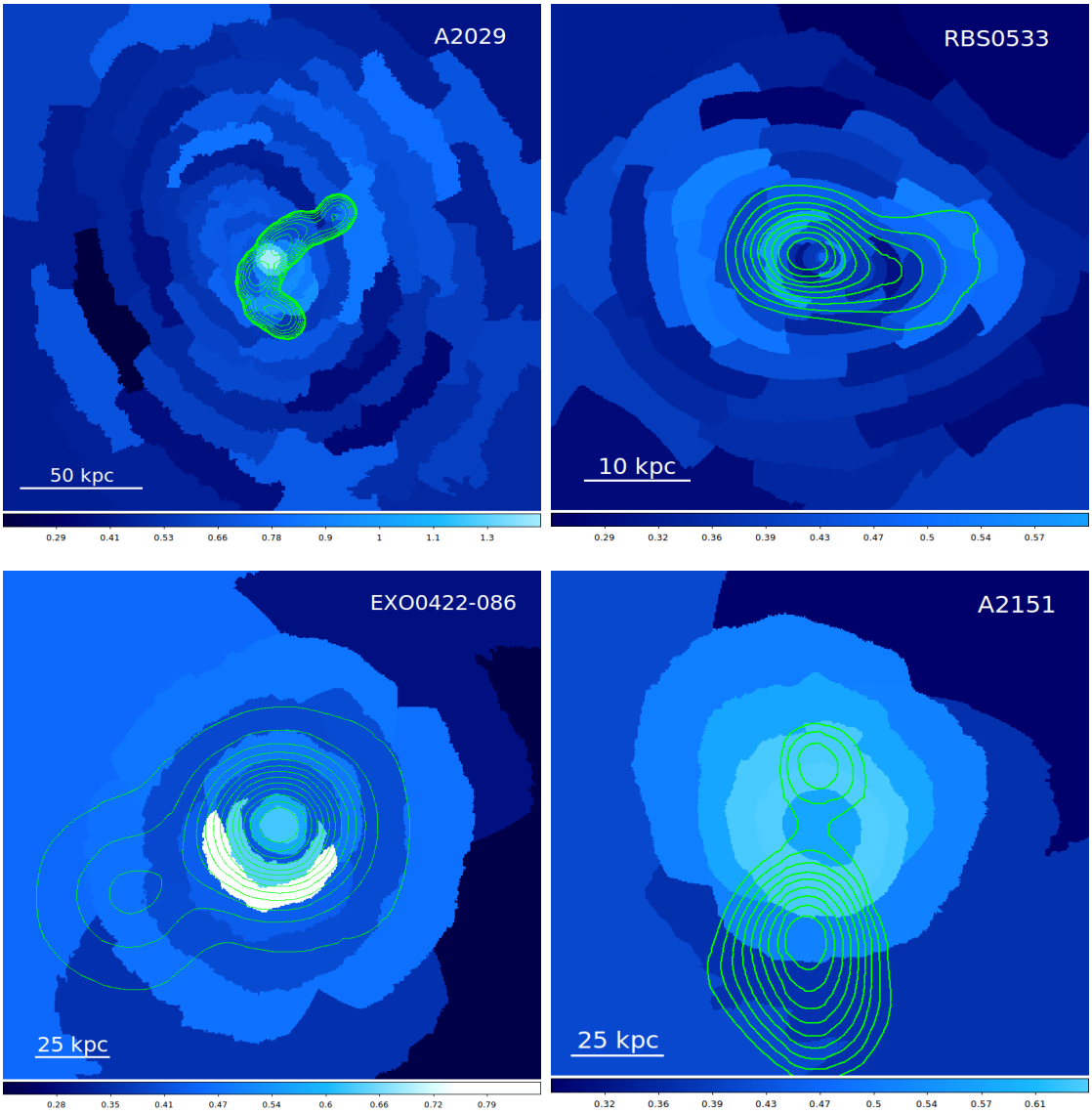


Figure 1.16: Metallicity maps of each cluster. Point sources were excluded from the images, where the colour bar is given in units of $Z_{\odot}$. The green contour lines are the radio data from the NRAO and VLA first survey. These maps show no evidence of metal-enriched plasma lying preferentially along jet axis.

### 1.5.2 Metallicity Profiles

To further constrain these findings, spectra were extracted from the profiles of annular sector bins with openings lying between 50 and 90 degrees. One of these profiles is along where the extended radio emission from the jet is located ("along-jet"). Extracted spectra in these regions are assumed to reflect the impact of the AGN on the gas. Other profiles are extracted along a direction orthogonal to or offset from the jet axis ("off-jet") and represents the undisturbed atmosphere. Spectra from these profiles are assumed to be representative of the average prior AGN outbursts. Extracted spectra were fit in the same way as was done to create the maps in Figure 1.16. The results of this analysis are shown in Figure 1.17.

A2029 demonstrates slight evidence of a trend in higher metallicity gas along the jet-axis, but only in bins between approximately $20-60$ kpc outward from its centre. It should be noted that the measured iron radius in this cluster is $\approx 43$ kpc, which is substantially smaller than in Kirkpatrick and McNamara (2015), where they found it to be $\approx 90$ kpc. There are two important reasons as to why these measurements could disagree. Firstly, they generate a different number of bins, which leads to differences in spatial scales of the bins. Secondly, the angular sizes of their bins are different from the bins used in this analysis, which leads to a difference in counts within regions and thus a difference in measured spectra. Lastly, they fit spectra using a WABS(MEKAL) model which will yield slightly different values for metal abundance than fitting spectra with a PHABS(APEC) model.

### 1.5.3 Statistical T-tests and KS-tests

To determine if these two profiles in Section 1.5.2 differ significantly, and thus the likelihood that an abundance excess along the jet axis is significant, two statistical tests are performed on each of the clusters two abundance profiles. The results of both statistical tests are shown in Table 1.5. In the first test, the means of both profiles are compared and used to calculate the liklihood that they are drawn from the same distribution using a two-tailed $t$-test. Statistical tests are performed at the 95% significance level ($\alpha = 0.05$) with the null hypothesis that differences between mean profile abundances are insignificant. In each of the clusters the null hypothesis cannot be rejected at this significance level.

In the second statistical test, a two-sample Kolmogorov-Smirnov (KS) test is performed to determine if both the along-jet and off-jet metallicity profiles are independent of one another, or come from the same distribution. Again, a significance level of $\alpha = 0.05$, is

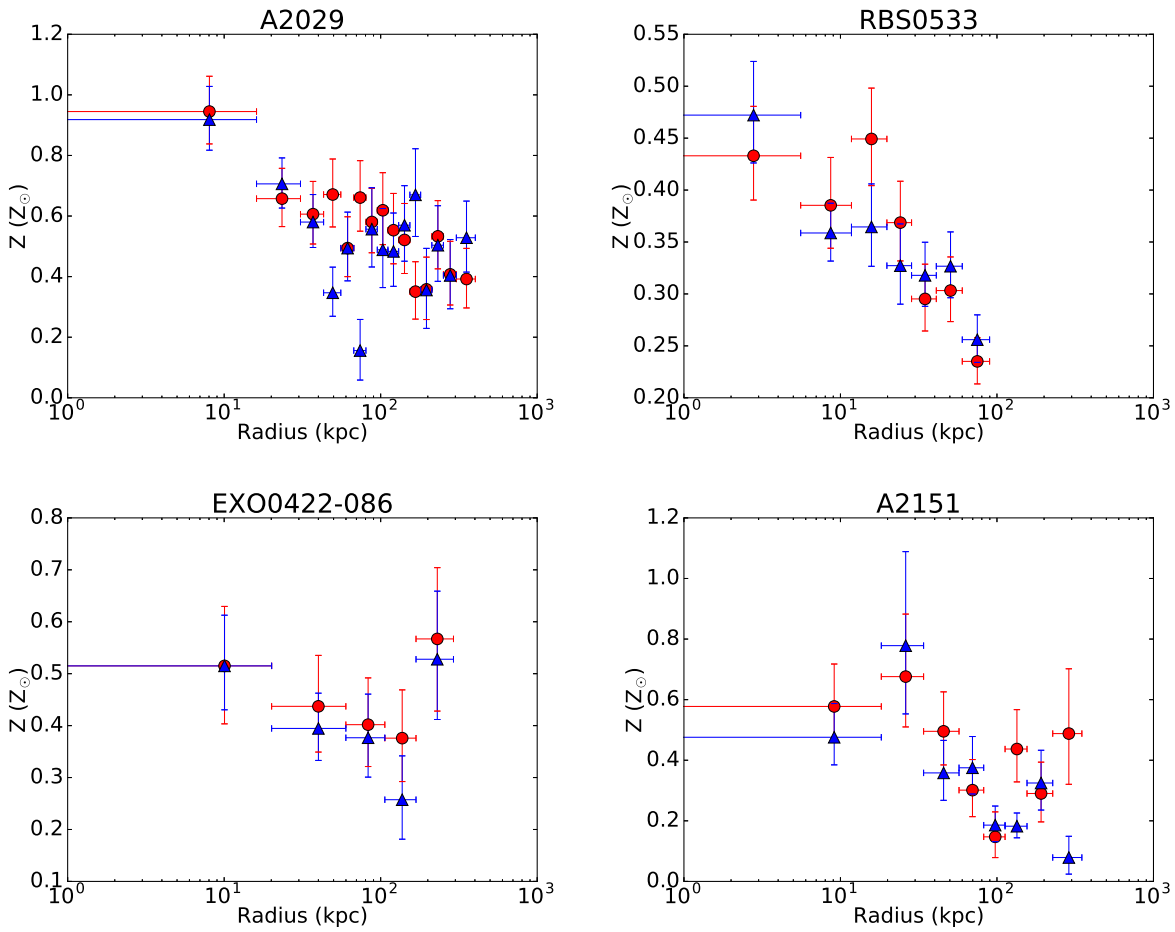


Figure 1.17: Metallicity profiles for the spoiler clusters. Top row from left to right: A2029, RBS0533. Bottom row from left to right: EXO0422-086, A2151. Spectra extracted along the jet axis are represented by red circles, and spectra orthogonal or off-jet are illustrated by blue triangles. These profiles show no evidence that metal-enriched gas preferentially lies along the jet axis, which is consistent with Figure 1.16. All errors are shown at the $2\sigma$ level.

Table 1.5: Summary of $t$-tests and KS-tests

| | $t$-test | | KS-test | |
|---|---|---|---|---|
| Cluster | $p$-value | Significant? | $D_{KS}$ | Same Sample? |
| A2029 | 0.52 | No | 0.0506 | Same |
| RBS0533 | 0.65 | No | 0.0191 | Same |
| EXO0422-086 | 0.40 | No | 0.146 | Same |
| A2151 | 0.42 | No | 0.168 | Same |

Results of our $t$-test and KS-test indicate no significant differences between along-jet and off-jet profiles in each of the clusters.

chosen with a null hypothesis, that both distributions are drawn from the same parent sample. The null hypothesis is rejected at our significance level if the calculated KS-statistic, $D_{KS}$, satisfies the condition given by $D_{KS} > \sqrt{-\frac{n+m}{2nm}\ln(\alpha)}$, where $n$ and $m$ are the sizes of the along-jet and off-jet profiles, respectively. Similarly to the $t$-test, the null hypothesis is unable to be rejected in any of these clusters.

At the 95% level, there is no significant difference between metallicity profiles in any clusters and thus, no evidence of uplifted metal-enriched gas. Indeed, extracting spectra along random directions not aligned with the jet axis, generally yield profiles that show no evidence of trends in this sample. Subsequent statistical analysis of these profiles only further confirms these results.

## 1.6 Discussion

In this Section, the discussion of thermally unstable cooling in clusters of galaxies, which was briefly discussed in Section 1.1.4, is continued. However, this is discussed mostly within the context of observations and simulations in Section 1.6.1. Finally, in Section 1.6.2 it is shown that all of the quoted measurements of H$\alpha$ luminosity in the ACCEPT database for these objects contradict observations in studies and literature.

### 1.6.1 Thermally Unstable Cooling

Central galaxies located at the bases of hot atmospheres are often associated with molecular clouds, star formation, and nebular emission. *Chandra* observations have shown that they are prevalent when systems lie below the central cooling time and entropy thresholds (1 Gyr and 30 keV cm$^2$ respectively), while those above are usually devoid of cool gas and star formation (Cavagnolo et al., 2008; Rafferty et al., 2008).

On a more fundamental level, hot atmospheres should be susceptible to thermally unstable cooling when the ratio, $t_{\rm cool}/t_{\rm ff}$, falls below unity (Nulsen, 1986; Pizzolato and Soker, 2005a; McCourt et al., 2012). In this context, the cooling time and entropy thresholds would be necessary but insufficient criteria. However, the local value of $t_{\rm cool}/t_{\rm ff}$ almost never lies below 10, even in systems experiencing vigorous star formation (Hogan et al., 2017b). Others have suggested that thermally unstable cooling occurs when this ratio lies well above unity, in the range between $10-30$ (McCourt et al., 2012; Sharma et al., 2012; Gaspari et al., 2012).

Inspection of Figure 1.12 & Figure 1.14 indicate that both the cooling time threshold and criterion satisfied and that the $t_{\rm cool}/t_{\rm ff} \sim 20-50$, the central galaxies in this sample should be thermally unstable and should be forming stars and shining by nebular emission. They are not. This failure to respond to both criteria calls for a third possible criterion, possibly uplift, which has been investigated in detail here.

In Section 1.4.1, it was shown that only RBS0533 has surface brightness depressions consistent with an X-ray bubble. However, it lacks bright rims composed of low entropy gas lifted from the inner region of the cluster. Furthermore, RBS0533 and the remaining clusters show no other evidence of substantial uplifted atmospheric gas that would trigger thermally unstable cooling once the gas reaches an altitude where $t_{\rm cool}/t_{\rm ff}$ falls below unity. Therefore, the observations are consistent with the hypothesis that uplift may be a significant factor driving thermally unstable cooling. This investigation does not constitute proof, but may indicate we are on the right track.

Another factor that may trigger thermally unstable cooling is mild atmospheric turbulence (Gaspari et al., 2018; Voit, 2018). Turbulence may be induced by the peculiar motion of the central galaxy and mergers. However, in this context the driving mechanism would most likely be the central AGN. The absence of X-ray bubbles would imply the absence of a mechanism to drive the turbulence imparted on the lifted gas. The sloshing spiral in A2029 seen in Figure 1.9 is evidence of a merger, and may indicate that it produced insufficient turbulence to trigger instabilities.

Low atmospheric turbulence then, may also be a factor leading to the thermal stability

of these systems. This hypothesis will be tested with the X-ray Imaging and Spectroscopy Mission (*XRISM*) and future X-ray observatories equipped with micro-calorimeter spectrometers

### 1.6.2 Absence of Cold Gas

These objects were selected on the basis of having upper limits on H$\alpha$ luminosity as listed in the ACCEPT database (Cavagnolo et al., 2008). As such, an exhaustive literature search for more recent nebular and molecular mass measurements followed.

ACCEPT lists RBS0533's H$\alpha$ luminosity as $L_{\mathrm{H}\alpha} < 0.016 \times 10^{40}$ erg s$^{-1}$. Two studies probing NGC 1550's CO emission, which is RBS0533's BCG, are in tension. O'Sullivan et al. (2018) detected no CO(2-1) or CO(1-0) emission, arriving at an upper limit for molecular hydrogen of $\mathrm{M_{H2}} < 0.47 \times 10^8$ $\mathrm{M_\odot}$.

However, (Nakanishi et al., 2007) claimed a detection of CO(3-2) deriving a molecular gas mass of $\mathrm{M_{H2}} = 4.3 \times 10^8$ $\mathrm{M_\odot}$. Clearly these measurements are inconsistent. The apparent CO(3-2) line is broad, spanning a significant fraction of the receiver's $\sim 445$ km s$^{-1}$ bandwidth, leaving little room for the baseline continuum to be evaluated. Taking this all into account, the (O'Sullivan et al., 2018) upper limit is adopted, indicating RBS0533 is largely devoid of cold gas.

RBS0533's central cooling time and entropy both lie below their respective thresholds ($10^9$ yr and 30 kev cm$^2$), respectively. It was shown in Section 1.4.1 that its atmosphere harbors an X-ray bubble, so the absence of cold gas is intriguing but not necessarily inconsistent with the hypothesis that thermally unstable cooling is stimulated by uplift.

McNamara et al. (2016) suggested that bubbles must lift cool, atmospheric gas to an altitude where $t_{\mathrm{cool}}/t_{\mathrm{I}} \lesssim 1$. The cooling time of the atmospheric gas at the center of RBS0533 is $\sim 10^8$ yr. Based on Figure 1.14, this gas must be lifted to an altitude of nearly 40 kpc to meet this cooling criterion. However, the observed bubble, at least in projection, extends to roughly half this distance. Therefore, it is likely the bubbles have not lifted enough atmospheric gas to stimulate thermally unstable cooling at an observable level.

A2151 has an H$\alpha$ measurement in the ACCEPT database of $L_{\mathrm{H}\alpha} < 0.141 \times 10^{40}$ erg s$^{-1}$. McDonald et al. (2011) detect H$\alpha$ in the BCG, NGC 6041, with a luminosity of $L_{\mathrm{H}\alpha} \sim 3 \times 10^{38}$ erg s$^{-1}$. Therefore, NGC 6041 has a detectable level, albeit, a modest level of molecular gas. However, emission at this level lies well below the luminosity where the cooling time threshold seen in Cavagnolo et al. (2008) becomes prominent at, $L_{\mathrm{H}\alpha} \sim 10^{41}$ erg s$^{-1}$

Table 1.6: **Cold gas measurements for the spoiler clusters; A comparison of H$\alpha$ measurements from the ACCEPT database versus other sources.**

| Cluster | BCG | $SFR_{UV}$ ($M_\odot$ $yr^{-1}$) | $L_{ACCEPT,H\alpha}$ ($10^{40}$ erg $s^{-1}$) | $L_{H\alpha}$ ($10^{40}$ erg $s^{-1}$) | $SFR_{H\alpha}$ ($M_\odot$ | $M_{H_2}$ ($10^8$ $M_\odot$) | Ref. |
|---|---|---|---|---|---|---|---|
| (1) | (2) | (3) | (4) | (5) | (6) | (7) | (8) |
| A2029 | IC 1101 | $< 1.72$ | $< 0.643$ | $< 0.44$ | $< 0.03$ | $< 17$ | [1][a], [2][b] |
| A2151 | NGC 6041 | $< 0.38$ | $< 0.141$ | 0.03 | 0.001 | $< 3.1$ | [3][a], [2][b] |
| A2107 | UGC 09958 | $< 0.57$ | $< 0.179$ | – | – | – | – |
| RBS0533 | NGC 1550 | $< 0.14$ | $< 0.016$ | – | – | $< 0.47$ | [4][b] |
| EXO0422-086 | MCG-01-12-005 | $0.4 \pm 0.09$ | $< 0.011$ | $< 0.014$ | $< 0.0004$ | – | [5][a] |

**Columns**: (1) Cluster, (2) BCG, (3) Ultraviolet SFR from Hoffer et al. (2012), (4) ACCEPT database H$\alpha$ luminosity (Cavagnolo et al., 2008), (5) H$\alpha$ luminosity, (6) H$\alpha$ luminosity is used to calculate $SFR_{H\alpha} = 7.9 \times 10^{-42} L_{H\alpha}$ (Kennicutt, 1998), (7) Molecular gas measurement from CO observations, (8) reference to [a]$L_{H\alpha}$ and [b]$M_{H_2}$ measurements: [1] McDonald et al. (2010), [2] Salomé and Combes (2003), [3] McDonald et al. (2011), [4] O'Sullivan et al. (2018), [5] Cavagnolo et al. (2009).

A detection of this magnitude is not unexpected for the accumulation of normal stellar mass loss from stellar winds, and external accretion that may be unrelated to uplift and thermally unstable cooling. In A2107, we find no measurements for cold gas and so the ACCEPT upper limit is adopted. In A2107, no measurements for cold gas are found and so the ACCEPT upper limit is adopted.

EXO0422-086's H$\alpha$ luminosity, $< 0.014 \times 10^{40}$ erg $s^{-1}$ (Cavagnolo et al., 2009), agrees reasonably well with the value quoted in ACCEPT, $< 0.011 \times 10^{40}$ erg $s^{-1}$. This is also the only cluster in the sample with a detection for $SFR_{UV}$ of $0.4 \pm 0.09$ $M_\odot$ $yr^{-1}$ (Hoffer et al., 2012).

In A2029, the H$\alpha$ measurement in the ACCEPT database tabulated as $L_{H\alpha} < 0.643 \times 10^{40}$ erg $s^{-1}$. McDonald et al. (2010) also found an upper limit measurement of $< 0.441 \times 10^{40}$ erg $s^{-1}$. In Figure 1.18, the values in Table 1.6 are plotted against the entropy and cooling time with values from literature over plotted from Cavagnolo et al. (2008) and Hogan et al. (2017b), respectively. These plots show that the spoiler clusters all lie below the respective cooling time and entropy thresholds, yet there is no clear H$\alpha$ threshold.

Lastly, the lack of bubbles and other activity associated with A2029's central galaxy

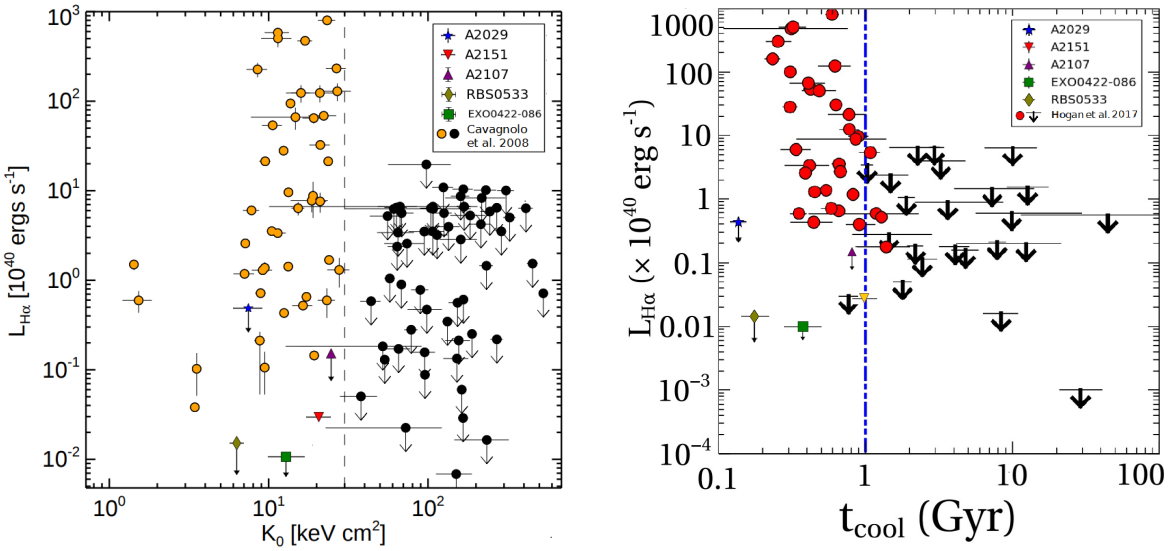


Figure 1.18: **Left**: The central entropy index of the spoiler clusters plotted against the H$\alpha$ luminosity. Literature values from Cavagnolo et al. (2008) are overlaid, where orange circles are H$\alpha$ detections and black circles are upper limits. **Right**: The minimum cooling time ($R < 10$ kpc) of the spoiler clusters plotted against the H$\alpha$ luminosity in Table 1.6. Literature values from Hogan et al. (2017b) are overlaid, where red circles are H$\alpha$ detections, and black arrows are upper limits. In both plots, $L_{H\alpha}$ measurements from ACCEPT are shown for A2107 and EXO0422-086.

is puzzling. Its short central cooling time and bright, cuspy X-ray emission is similar to other clusters replete with billions of solar masses of molecular gas and star formation at rates of tens of solar masses per year, yet its BCG is dormant. Nevertheless, its central radio source is relatively powerful, rivalling other systems with substantial X-ray bubbles.

The absence of bubbles in the presence of a strong radio source[1], $P_{1.4} \sim 10^{41}$ erg $s^{-1}$ (See Appendix A.1) with no lobes may indicate that this cluster hasn't reached a phase where it can buoyantly lift bubbles or that some radio sources with powerful synchrotron emission lack the mechanical power seen in other systems with comparable synchrotron luminosities. Croston et al. (2018) have pointed out that Fanaroff & Riley class (FR) I and II radio galaxies have different particle contents, with FRIs having higher jet (mechanical) power for their synchrotron luminosities than FRIIs. Perhaps A2029's radio source is composed of light particles akin to an FRII radio source rather than a FRI which is commonly found

[1]The radio power measured at 1.4 GHz from (Condon et al., 1998)

at the centers of clusters.

## 1.7 Conclusions

In this an analysis of five objects were examined using *Chandra* X-ray data. In this final Section, the main results are summarized along with the details of future work.

### 1.7.1 Summary

In this thesis, the properties of five galaxy clusters have been studied in detail, which were selected on the basis of having upper limits on cold gas as listed in the ACCEPT database yet with short central cooling times. Projected and deprojected thermodynamic profiles reveal that within the central 10 kpc of each cluster, the atmospheric cooling times and entropys lie below their respective thresholds of $10^9$ yr, and 30 keV cm$^2$, below which the presence of cool gas and star formation are common. However, these clusters are lacking any significant H$\alpha$ detections. Here, the hypothesis of uplift for the origin of cold gas as proposed by McNamara et al. (2016) was tested.

Only one cluster, RBS0533, has structure which is consistent with an possible X-ray cavity. This feature is a 31% deficit in Figure 1.7 relative to the elliptical double $\beta-$model, with a SNR of $\sim 28$. While 1/5 of the clusters objects show evidence of a cavity, which is below the expected fraction for a random sample, four of the five clusters have radio emission as shown in Figure 1.16 which is consistent with systems that have short central cooling times. The absence of H$\alpha$ emission in RBS0533 can perhaps be explained by the fact that it has no bright rims, which may indicate that it is unable to effectively lift gas. This discovery prompted a comprehensive search for cold gas beyond the ACCEPT database. The search for cold gas including H$\alpha$ and CO measurements show that all objects excluding A2151 and A2107 have upper limit detections on said quantities, where the former has an H$\alpha$ detection and the latter has no measurements of either.

Thermodynamic profiles extracted along and off of the jet axis shows no evidence of uplift or that higher metallicity gas lies preferentially along the jet-axis. This is clearly evident in our abundance maps and metallicity profiles within Figure 1.16 and Figure 1.17, respectively, and was confirmed more rigorously through statistical analyses using a $t$-test and KS-test.

### 1.7.2 Future Work

This work attempted to confirm the theory put forward by McNamara et al. (2016), in which cold gas condenses in the wakes of bubbles, or that cold gas is uplifted by buoyantly rising X-ray bubbles, or a combination of the two. It was shown that these observations are still consistent with this hypothesis. Although, the investigation does not constitute definitive proof, it demonstrates that we're on the right track.

This work could be improved by obtaining more H$\alpha$ or CO data for these objects, especially in RBS0533, and determining if they have detections. Ideally, by looking for signatures of bubbles or cavities in a larger sample of objects below the cooling time and entropy thresholds, that have no listed H$\alpha$ measurements would be the most effective way to prove or disprove this theory. Moreover, obtaining deeper *Chandra* observations for A2107, whose available exposure time totals a meager $\sim$ 35 ks. This would substantially improve the analysis and allow for more bins below 10 kpc for spectral analysis, and also allow for the creation of metallicity maps, and extraction of metallicity profiles along and off of the jet axis.

# Chapter 2

# Filter Calibrations for the X-ray Imaging and Spectroscopy Mission

## 2.1 Introduction

The predecessor of the X-ray Imaging and Spectroscopy Mission (*XRISM*) was the *Hitomi* mission, previously known as *Astro-H*, which was launched from the Tanegashima Space Center, Japan, on February 17, 2016. An important instrument installed on Hitomi was the Soft X-ray Spectrometer (SXS), a microcalorimeter array that is cooled to 50 mK which provides high resolution non-dispersive spectroscopy from 0.3 to 12 keV. This instrument enabled plasma diagnostics in this energy range, and includes K-shell transitions of abundant elements from C through Ni, as well as L-shell transitions of elements, including roughly 3 eV spectral resolution at the Fe K-edge.

The SXS microcalorimeter array consisted of ion-implanted Si thermistors and HgTe thermalizing X-ray absorbers that operate at temperatures of 50 mK (Kilbourne et al., 2018). Because of this low temperature, the optical path of the SXS included a set of five thin-film aluminized polyimide filters which are anchored to shield the detector from long wavelength thermal radiation and optical and UV photons from the sky while allowing transmission in the soft X-ray band (Kilbourne et al., 2018). This instrument unfortunately was lost on March 26, 2016. The loss of *Hitomi* motivated the creation of a X-ray telescope mission, *XRISM*. A schematic of the aperture assembly in Hitomi is shown in Figure 2.1, for which *XRISM* will be based on. Like *Hitomi*, *XRISM* will have a set of five optical blocking filters. As these are extremely fragile, four of each type of filter are fabricated and calibrated as backups for any that may be damaged.

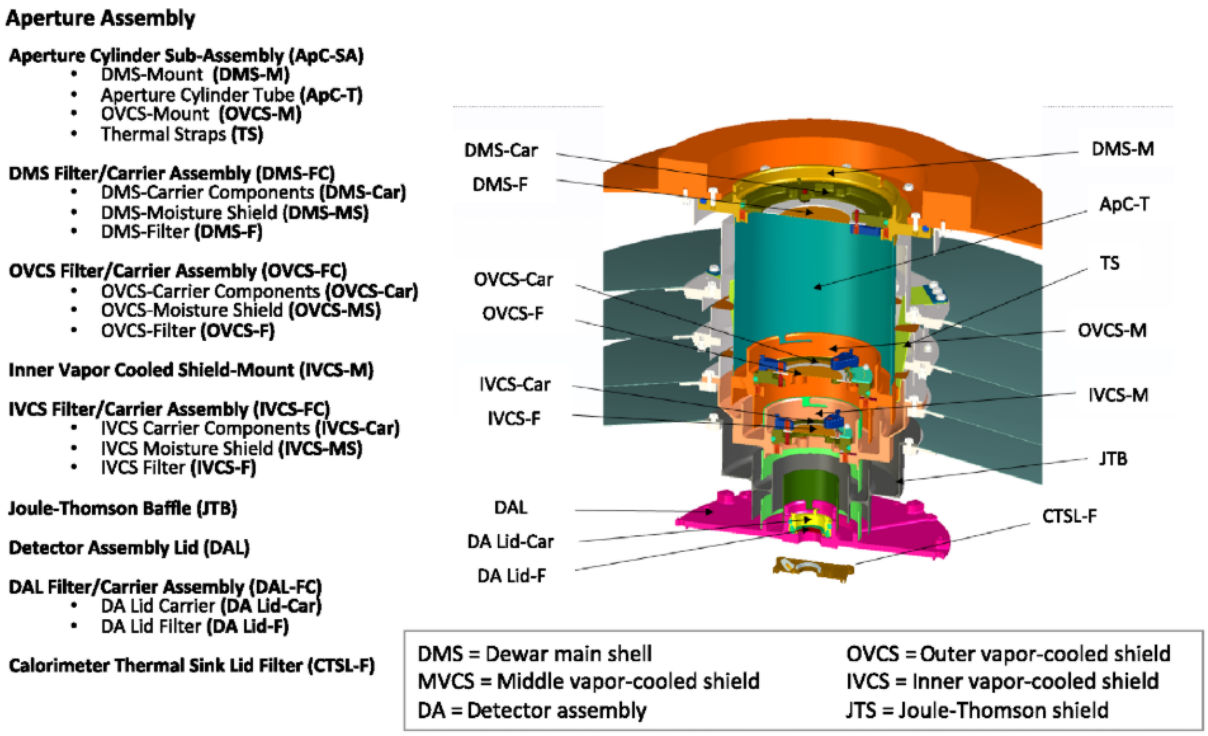


Figure 2.1: Shown here is the *Hitomi* schematic for the arrangement of the aperature assembly (ApA) and blocking filters (BF) taken from Kilbourne et al. (2018). The position of installed flight carriers are installed and the fixed calorimeter thermal sink filter are shown. The arrangement of the *XRISM* ApA and BF's will largerly follow that of *Hitomi*.

Like the SXS in *Hitomi*, the instrument on *XRISM*, named Resolve, is based off the SXS, and will include a set of Al/polyimide thin-film optical blocking filters mounted inside the SXS dewar. Throughout the course of my thesis I participated in the transmission calibration of several optical blocking filters at the Canadian Light Source and the Advanced Light Source located in Saskatoon and Berkeley, respectively.

In Section 2.2, the basic processes through which radiation interacts with matter and the fundamentals of absorption edges of elements are described. In Section 2.3, the motivation of optical blocking filters to be installed in Resolve are discussed including their composition and expected absorption features. In Section 2.4, a summary of how synchrotron facilities function are explained as well as the beamline used throughout the experiment to take measurements are introduced. In Section 2.5, the calibration process used to take measurements are summarized along with details pertaining to modelling used to estimate

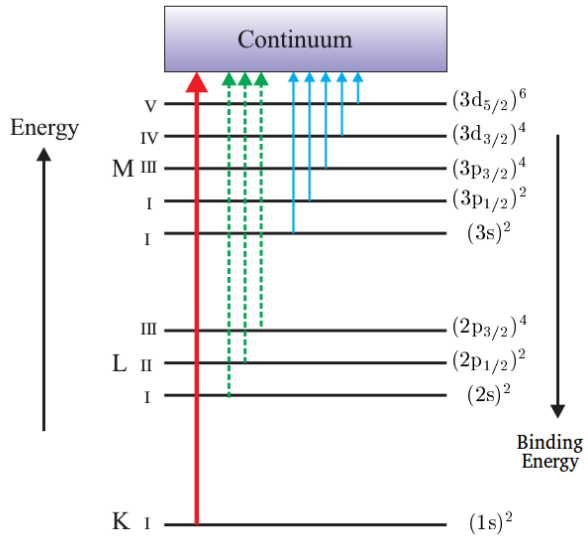


Figure 2.2: A summary of absorption edges where electronic shells are labelled, taken and adapted from (Als-Nielsen and McMorrow, 2011).

parameters of the calibrated filters such as the filter thickness.

## 2.2 EXAFS and XANES

The spectrum of X-rays extends from 100 eV to 100 keV, and can be divided into two categories: The soft X-ray (SXR) region which extends from 100 eV to 10 keV, and hard X-rays which covers the rest of this range and is widely used for imaging such as in dental X-rays, and airport security. As the spectrometer to be installed on *XRISM* is the Resolve instrument, which is based off the SXS, only the former region will be discussed in length here.

The SXR region is characterized by primary resonance lines and absorption edges of most low and intermediate $Z$ elements. Where, $Z$, is the number of protons in the nucleus or the atomic number. The K-edge, L-edge, and M-edge are absorption edges that are associated with the removal of a core electron by photoabsorption from the most tightly bound atomic states (principal quantum numbers of n=1, 2, and 3 respectively) as shown in Figure 2.2 (Attwood, 2000).

Shown in Figure 2.3(a) is the process for an electron collision induced ionization. A primary electron incident on an atom with several orbiting electrons around a positively charged nucleus, which has sufficient energy, $E_p$, to remove an electron during a close encounter. The incident electron is scattered off of this core electron with some angle, and with a reduced energy ($E'_p$). The difference in $E_p - E'_p$ is mostly due to overcoming the binding energy of the core electron, and partly due to supplying the now free core electron with kinetic energy, $E_s$. The atom then is left with a vacancy in its core.

In Figure 2.3(b), another process known as photoionization/photoabsorption is shown. Here a photon with sufficient energy is absorbed by the atom, transferring its energy to an emitted photoelectron with energy equivalent to the difference in the initial energy and the binding energy of the electron in its particular shell. Obviously, an electron in the K-shell has a higher binding energy than an electron in the L-shell, and so it will emerge with less kinetic energy than would an L-shell electron.

Both of these ionization processes leaves the atom with a vacant spot in its core shell. The atom will then rearrange itself into a lower energy state so that electrons from a higher orbital fill this gap by one of two processes. In Figure 2.3(c), the atom rearranges itself in a process known as fluorescence, where an electron's transition from a higher orbital to the vacant one is accompanied by the emission of a photon with energy equal to the difference between the energies of the initial and final atomic state. A competing effect shown in Figure 2.3(d) causes the atom to rearrange itself through the emission of a second Auger electron. Which process is most dominant depends on the atomic number of the atom; A higher Z tends to increase the probability of fluorescent emission, whereas a lower Z is dominated by the Auger emission process (Als-Nielsen and McMorrow, 2011).

When observing an emission spectrum of a material, the two major features are due to characteristic line emission and bremsstrahlung emission. The latter is a German word which translates to "braking radiation" in English. This process can be described by a simple scenario. Suppose an electron with velocity, $v$, approaches a proton or nucleus. At its closest approach, b (sometimes called the impact parameter), the electron will decelerate causing a loss of kinetic energy, which is converted into radiation (i.e. emission of a photon). If the number of incident photons is large, with various impact parameters, then this creates a broad emission continuum.

Historically, the process of photoabsorption, Figure 2.3(b), has been observed by passing radiation through thin films and observing the resultant decrease in intensity as a function of the films thickness (Rothschild et al., 1997; Rothschild, 1998). The change in intensity, $I'$, of radiation through a material of thickness $t$, is given by (Attwood, 2000; Als-Nielsen and McMorrow, 2011),

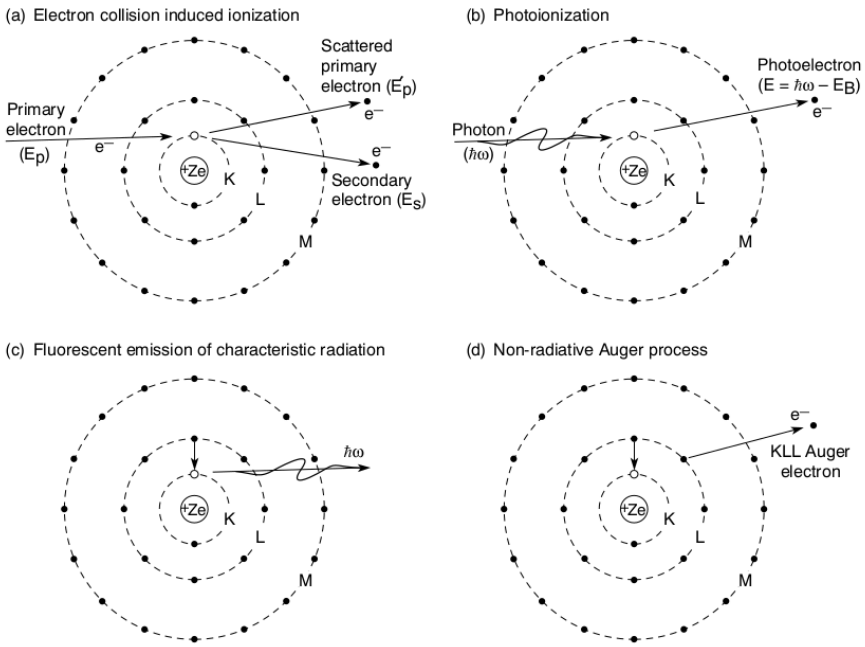


Figure 2.3: Figure taken from (Attwood, 2000). (a) An incident primary electron of energy $E_p$ is scattered by an atom as it releases a core electron from the K-shell. (b) In another process known as photoionization, a photon with energy, $h\omega$, is absorbed by an atom causing a photoelectron to be emitted. (c) The atom now with a vacancy in its shell may experience fluorescent emission, where an electron from a higher orbital fills the hole and emits a photon with energy $h\omega$. (d) In another process, the atom rearranges itself by the emission of an Auger electron which allows another electron to fill the vacant spot in the shell.

$$\frac{dI'}{dt} = -I'\rho\mu, \tag{2.1}$$

where $\rho$ is the mass density, and $\mu$ is the mass-absorption coefficient whose value is dependent on the photon energy and depends on the element in question. A figure of $\mu$ for different elements is shown in Figure 2.4. Integrating the equation by separation of variables yields,

$$\frac{I}{I_0} = e^{-\rho\mu t}, \tag{2.2}$$

where $I_0$ is the incident intensity, and $I$ is the intensity after transmitting through the material. The ratio of $I/I_0$ is the approximate transmission, $T$, of radiation through the material,

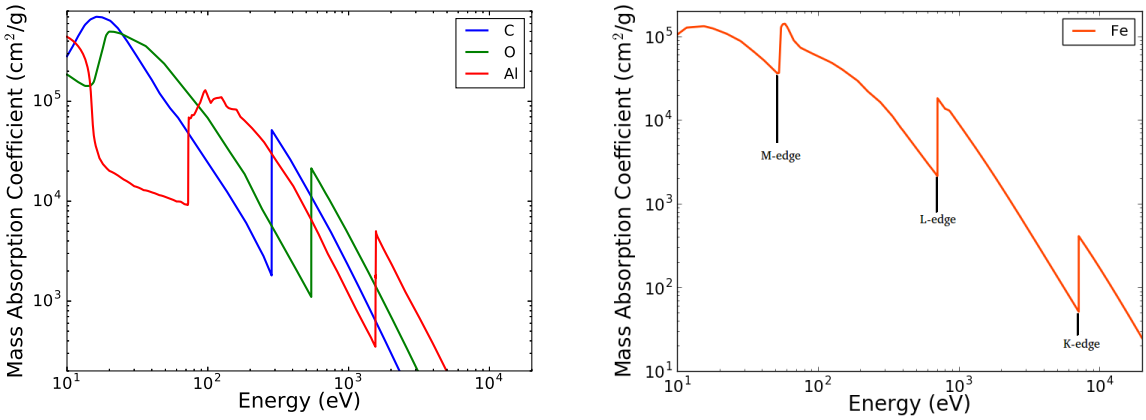


Figure 2.4: Mass Absorption Coefficient at different energies, data taken from CXRO. Left: For elements Carbon (blue), Oxygen(green), and Aluminum (red). Right: Iron, where the different edge structures are labelled

$$T = e^{-\rho\mu t} \tag{2.3}$$

This same expression can also be written in terms of the photo absorption cross-section per atom, $\sigma_a$ by,

$$T = \exp\Big(-t\frac{\sigma_a \rho N_A}{M}\Big), \tag{2.4}$$

where $N_A$ is Avagadro's number, and $M$ is the molar mass. The main difference between Equation 2.3 and Equation 2.4 is that the former is derived experimentally from atoms within a particular solid material. The latter however has $\sigma_a$, which is calculated for single isolated atoms, and is beneficial, in that it includes information about the contributions from each atomic subshell as shown for a copper atom in Figure 2.5 (Attwood, 2000). The absorption cross-section develops structure for photon energies in the vicinity of an absorption edge which are known as the extended X-ray absorption fine structure (EXAFS) and the X-ray absorption near-edge Structure (XANES). For instance, in the bottom panel of Figure 2.6, the spectrum for a normalized absorption coefficient of iron oxide (FeO) is shown at different energies. The K-edge here can be seen at $\sim$ 7150 eV. Also shown are the EXAFS and XANES region of the spectrum.

Table 2.1: **Summary of Past Calibration Runs**

| Date of Calibration | Synchrotron | Filters Calibrated |
|---|---|---|
| Dec 12 − Dec 16, 2018 | ALS | DA, CTS, and witness samples |
| Jan 28 − Feb 8, 2019 | CLS | Flight-candidate mesh filters (one of each type) and witness samples and telescope thermal shield and witness samples |
| May 8 - May 10, 2019 | ALS | Flight-candidate mesh filters (IVCS, DMS, OVCS) and thermal shield |

A summary of the past calibration runs that I participated in throughout the course of my thesis.

The structure seen within the regions surrounding the absorption edge (±10 eV) is the XANES region. This XANES region physically corresponds to the transition of core electrons to vacant states below the continuum of free electron states. Since the density of bound states close to this edge may be higher than the density of unbound states, the absorption has a peak. For slightly higher photon energies above the edge ($10 - 50$ ev), photoionization causes photoelectrons to be ejected from the atom, which propagates outwards as a spherical wave. This wave may be back scattered by neighbouring atoms producing an oscillation in the absorption coefficient, $\sigma_a$. This low energy photoelectron then undergoes multiple scattering (Als-Nielsen and McMorrow, 2011), and as a result this region is sometimes referred to as the near edge X-ray absorption fine structure (NEXAFS) regime.

At photon energies exceeding 50 eV from the edge, photoelectrons have sufficient energy that single scattering events begin to dominate, this is the EXAFS region.

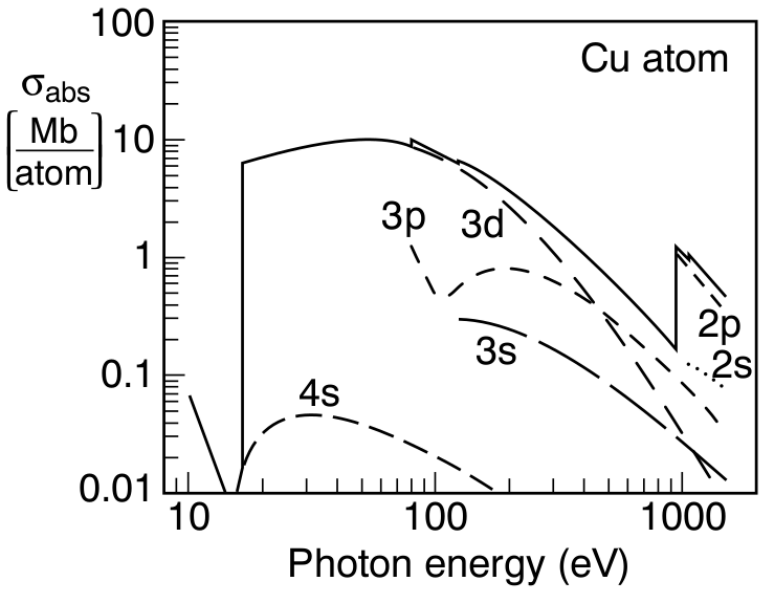


Figure 2.5: Photoabsorption cross-section for a copper atom taken from (Attwood, 2000). Shown as a black solid line is the total cross-section for the atom, with several of its contributions from atomic subshells labelled as dashed and dotted lines.

## 2.3 Optical Blocking Filters

The filters to be installed in Resolve are comprised of two groups. The first includes, the calorimeter thermal sink (CTS), and detector assembly (DA) filters, which are composed of an aluminumized polyimide film mounted on an aluminum ring, which will both be installed in the DA. The second group consists of the inner vapor cooled shield (IVCS), the outer vapor cooled shield (OVCS), and the Dewar main shell (DMS) filters, which are composed of a thin aluminized polyimide film mounted on a hexagonal silicon mesh structure, each of which is to be installed in the aperture assembly. Silicon meshes are composed of a coarse and a fine hexagonal grid. A brief summary on the dates of these calibration runs, the synchrotron they were performed at and the filters that were measured are shown in Table 2.1

In this report, the focus is entirely on two filters from the second group, which are so named: OVCS-7, and IVCS-6. Photoelectric absorption edges are expected in the aluminized polyimide film at the C K-edge (284 eV), N K-edge (410 eV), O K-edge (543 eV), and Al K-edge (1560 eV). Measurable EXAFS is expected in all of these edges which re-

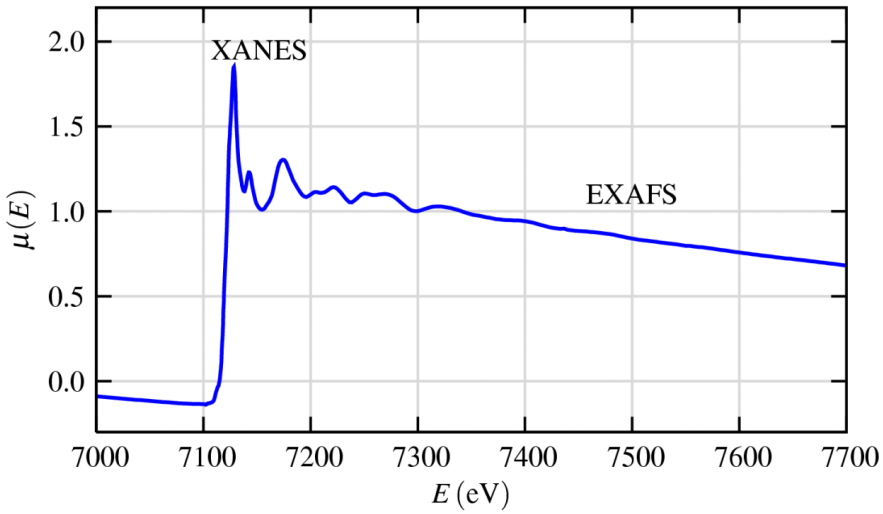


Figure 2.6: The absorption spectrum as a function of photon energy for iron oxide (FeO), where $\mu$ is normalized to a single absorption event (Newville, 2004).

quires high spectral resolving power in calibration measurements. The Resolve instrument will have spectral resolution close to 5 eV such that, measurements of the filter transmission near these edges is done with spectral resolution of 1-2 eV when ever possible. The fine Si mesh is slightly transparent at energies below the Si K-edge (1839 eV), although, it is opaque at energies above the Si K-edge, such that no EXAFS will appear in the SXS effective area. In the next Section, synchrotron facilities used for measurements are briefly described.

## 2.4 Synchrotron Facilities and Beamlines

Metrology beamlines were used to measure the X-ray transmission and physical properties of a small subset of the Resolve EM optical blocking filters. These synchrotron facilities include: the Canadian Light Source (CLS) in Saskatoon, Saskatchewan affiliated with the University of Saskatchewan, and the Advanced Light Source (ALS) in Berkeley Labs located in Berkeley, California. Here, the basics behind how synchrotron facilities function are discussed in Section 2.4.1. In Section 2.4.2 the specifics behind the beamline used during the better part of the experiment are explained.

### 2.4.1 Synchrotron Facilities

The basic means by which a synchrotron facility functions is widely the same across multiple synchrotrons, with some small differences. In general all processes are done under vacuum conditions. At the CLS[1], in order to **obtain** electrons with energies in the X-ray region, an electron gun is utilized, which uses a tungsten oxide disk as a cathode (electrical conductors that allow electrons to flow through them), similar to an incandescent light bulb. As electrons flow through the cathode, it becomes heated to high temperatures ($\sim$ 1200 K), giving enough thermal energy to some electrons, allowing them to leave the surface of the cathode (this process is somewhat analogous to boiling a pot of water). At the same time, a strong but fleeting voltage of about 200 kV is applied to a nearby screen (about 125 times per second) giving it a positive charge, which pulls escaping electrons away from the cathode. Electrons attracted to the screen are further repelled by electrons on the surface of the cathode. These electrons are then accelerated towards a Linear Accelerator (LINAC). This essentially acts to create pulses of electrons that enter the LINAC every second (Cutler et al., 2017).

The LINAC is composed of a series of radio frequency cavities (RFCs) with fields maintained at 2.856 GHz. These cavities accelerate electrons to energies of 250 MeV, with velocities approaching the speed of light ($\sim 0.9999c$). Electrons travel from the LINAC to the booster ring where another special RFC is used to raise the energy of electrons from 250 MeV to 2.9 GeV. As bunches of electrons ($\sim 3 \times 10^8$) circulate this 103 m booster ring nearly 1.5 million times in 0.6 seconds, an injection system transfers electrons into the 171 m storage ring. During normal operation, injections of long pulses of electrons produce a 420 ns pulse train into the storage ring, where pulses are supplied once every second by the LINAC.

While referred to as circular, the storage ring is actually composed of 12 straight sections which have several bending magnets that cause an electrons path to be bent, thus causing it to emit photons via synchrotron radiation. After some time, enough electrons are accumulated in the storage ring, reaching a circulating current of about 250 mA. Once currents reach this level the synchrotron may operate for several hours and the LINAC is turned off. However, overtime electrons stored in the ring will decline as vacuums are imperfect, so collisions between electrons causes their abundance to decrease over time (4 to 12 hours). As a result, the CLS must periodically refill the ring with more electrons (Cutler et al., 2007).

This method of injection is the known as 'refilling,' although other facilities use a

[1]For a more in depth description, see https://www.lightsource.ca/inside_the_synchrotron.com

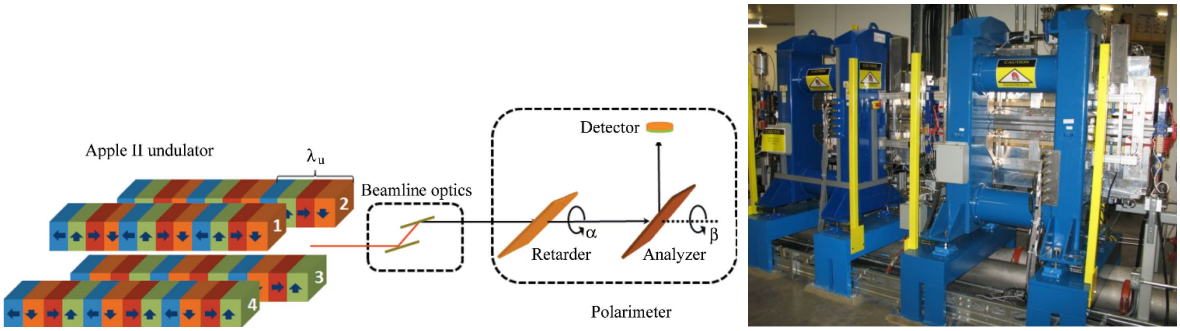


Figure 2.7: **Left:** A typical schematic of an EPU where an incident electron is accelerated through the undulator schematic. **Right:** The EPU at the a REIXS beamline in the CLS.

different injection method. For instance, the ALS uses a 'top off' method where their storage ring is nominally maintained at 500 mA. In this method of injection, when the current drops below some threshold ($\sim$ 480 mA), electrons are automatically injected into the storage ring by a very similar process to the one described previously. This injection method is substantially more difficult to maintain, but generally is less detrimental to the user.

When electrons are circulating the storage ring, at each turn they produce photons, and at each turn there is also a photon port. This allows light to travel down the beamlines toward end stations. Each beamline is equipped with an optics hutch where synchrotron light is focused and a specific wavelength is selected using a monochromator that separates light using optical dispersion or a diffraction grating; an experimentation hutch where appropriate techniques for that a particular end station lie; a work station where users can operate the beamline (Cutler et al., 2017).

### 2.4.2 REXIS Beamline

During my work on XRISM, the Resonant Elastic and Inelastic X-ray Scattering (REIXS), and the Industry, Development, Education, and Students (IDEAS) endstation were used at the CLS, however only the former will be discussed here. REXIS is a state-of-the-art X-ray scattering facility with high flux ($2 \times 10^{11} - 1 \times 10^{12}$ photon/s), high spectral resolution and full polarization control. It operates using energies between $80 - 2000$ eV with a beam size of $250 \times 150$ $\mu$m (and may be adjusted to smaller a size of $10 \times 50$ $\mu$m) using an Apple II-type elliptically polarizing undulator (EPU) (Cutler et al., 2017).

An undulator is a series of dipole magnets placed in a certain structure as shown in left side of Figure 2.7. The static magnetic field produced by the magnets will alternate along a length of the undulator with wavelength $\lambda_u$. The polarization may also be controlled which gives users high intensity X-rays with narrow energy ranges. An image of the EPU at the beamline is shown in the right panel of Figure 2.7.

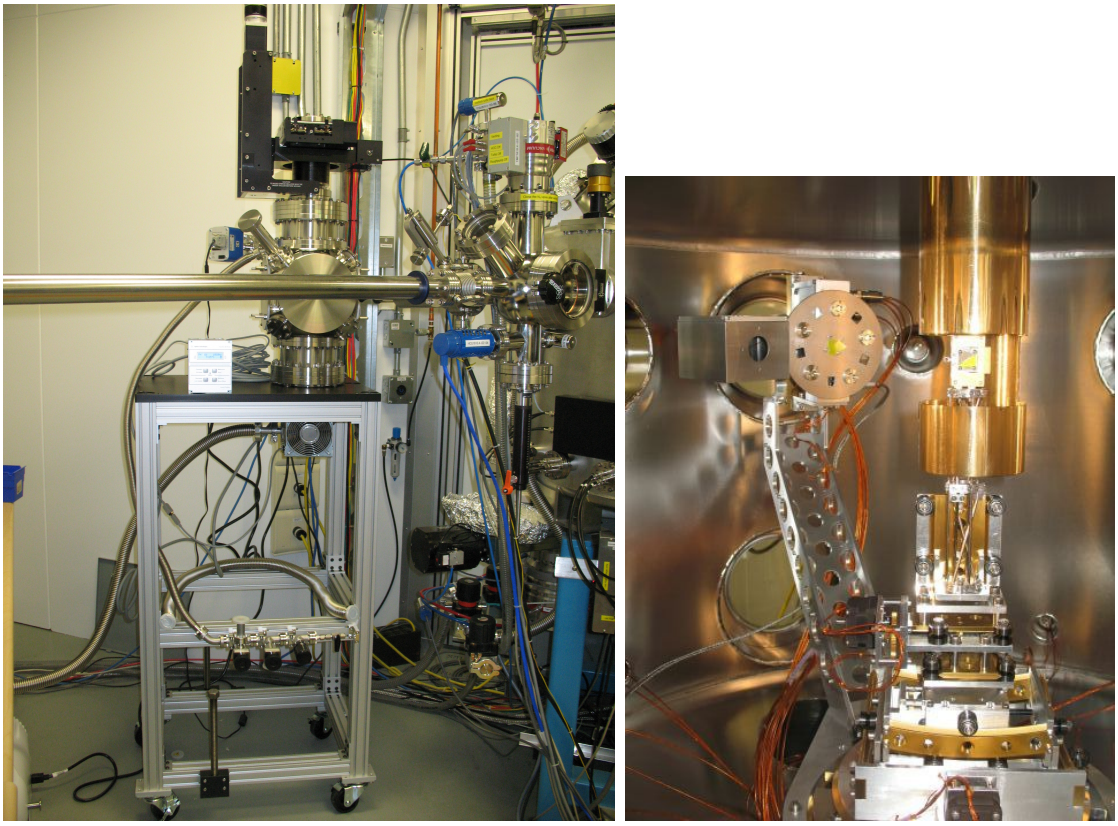

Figure 2.8: **Left**: An outside look of the satellite commissioned endstation where filters were mounted at the CLS during calibration runs. **Right**: An inside look of a sample chamber where filters are mounted.

## 2.5 Calibration of Optical Blocking Filters

The Resolve aperture will consist of several aluminized polyimide optical blocking filters, a few of which will be discussed in detail, specifically outer-vapor cooled shield (OVCS-7A),

and the inner-vapor cooled shield (IVCS-6).

These filters are nearly 200 nm in thickness which are supported by silicon meshes that are micromachined using silicon-on-insulator (SOI) wafers that are attached to the meshes using epoxy. The mesh consists of nearly 225 micron thick "coarse" hexagonal mesh with cells spaced by 5.28 mm within which there was a 25 micron thick "fine" hexagonal mesh with a cell spacing of 0.33 mm as shown in the right panel of Figure 2.9.

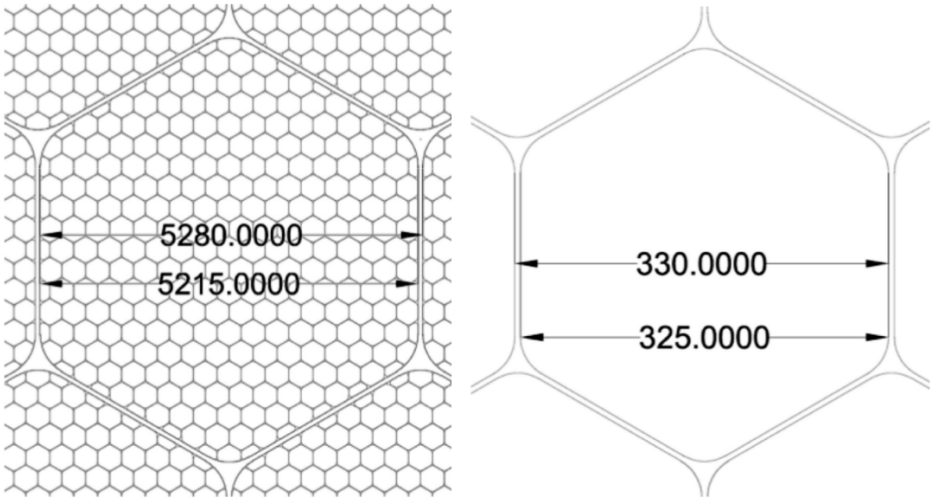


Figure 2.9: Figures taken from (Eckart et al., 2018), but are still representative of the filters used in this calibration project. **Left:** The dimensions of the coarse mesh in microns where each cell is spaced by 5.28 mm. **Right:** The dimensions of the fine mesh in microns which corresponds to one of the cells in the left figure, where cells are spaced by 0.33 mm.

The transmission of these filters were measured at the CLS in 2019. The REXIS beamline was used to constrain the broadband filter transmission; the fine K-edge structure of C, N, O, and Al. All edge structure measurements were done with higher spectral energy resolution than broadband structure scans.

A new satellite endstation was commissioned for calibration of the Resolve filters. The sample (filters) are mounted in a vacuum chamber as shown in Figure 2.8, which are pumped down to vacuum pressures of $5 \times 10^{-7}$ Torr before measurements were taken. The temperatures inside the sample chamber was fixed at room temperature and not adjusted through measurements. A photodiode detector was used to measure the current from the beam, which also has multiple filters available including: V, Cr, Fe, and Ni. The

advantage of using these filters is that they suppress higher order contamination and allow for calibration scans of their respective shell edges (i.e. the Fe L-edge at 707 eV).

Position scans prior to calibration measurements ensured that the beam avoided the coarse mesh bars of the filters (left image in Figure 2.9). Once the correct position was found, spectral scans were performed on IVCS-6 and OVCS-7(A) in the energy range of 260eV − 2000eV. This was done in multiple steps to switch in the correct higher order suppression (HOS) filters and to reduce the strain on the monochromator. The Resolve optical blocking filters are mounted on calibration holders as shown in Figure 2.10 which were installed in the vacuum sample chambers shown in Figure 2.8. For both of these filters, the transmission was measured at different locations to confirm their spatial uniformity.

The transmission of each filter was determined by measuring the amount of current using the photodiode detector in the absence of filters, $I_0$, which is convenient to measure, as mounting plates used at the CLS have a hole which the beam can be transmitted through as shown in the bottom image of Figure 2.8. Then, by directing the beam through one of the filters and measuring the current, $I$, and normalizing both measured currents, one can obtain the transmission of an individual filter by,

$$T = (I/X)/(I_0/X_0), \tag{2.5}$$

where $X$ and $X_0$ are the respective normalizations used for spectral energy scans of the filter and open hole. The normalization technique used throughout calibrations varied, but the technique which minimized noise in the transmission measurements was generally adopted. One such normalization technique is to use the circulating current or ring current of the CLS to normalize photodiode measurements. An advantage of this is that ring current is fairly steady between measurements as it decays slowly with time. A disadvantage of using the ring current is that transmission scans won't reflect fluctuations in the energy dependence of the beamline. As such, a thin gold mesh may be used to normalize scans, which is placed between the source and where the sample is placed in the chamber. The beam transmits through this mesh creating a current that is measured.

During our calibration, a specific strategy was adopted when performing energy scans over the filters and open hole positions. Full energy scans were broken up into six energy scans for the purposes of switching the appropriate HOS filters to make calibration scans of over appropriate edge structure, and to reduce the strain on the monochromator, which is prone to overheating when used continuously to change the beam energy. The details of this are tabulated in Table 2.2. Finally, after performing all of the tabulated scans, one can use Equation 2.5, to obtain the transmission as shown in Figure 2.11. Here, full energy scans were performed on two coarse mesh cells within each filter. These plots indicate that both filters are relatively uniform with a difference in transmission of at most 1.5%.

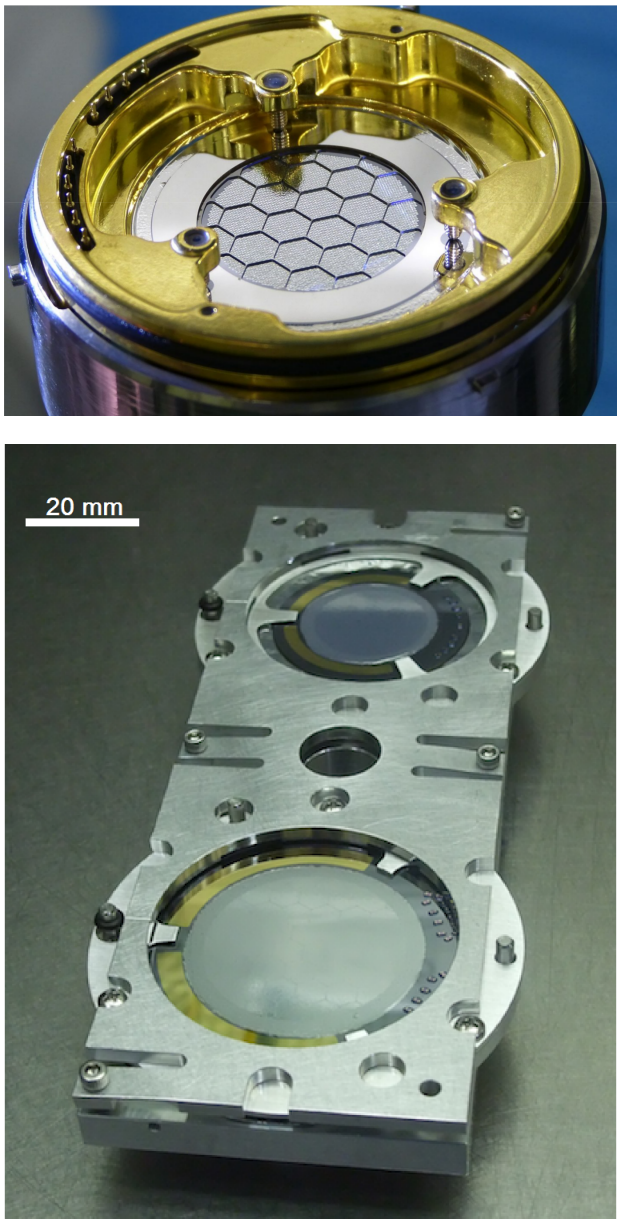


Figure 2.10: **Top**: An IVCS blocking filters where the fine mesh is visible taken from Kilbourne et al. (2018). **Bottom**: Two SXS optical blocking filters that are mounted in calibration holders at the top and bottom of the plate which are very similar to the ones installed in sample chambers at the CLS Eckart et al. (2018).

Table 2.2: **CLS Spectral Scan Measurements**

| Energy Scan Range | 260 – 360 eV | 290 – 440 eV | 360 – 500 eV | 480 – 850 eV | 800 – 1600 eV | 1500 – 2000 eV |
|---|---|---|---|---|---|---|
| HOS Filter | Vanadium (Va) | Chromium (Cr) | Iron (Fe) | Nickel (Ni) | None | None |
| Steps | 25 | 15 | 10 | 30 | 31 | 19 |
| Exposure Time (s) | 10 | 10 | 10 | 10 | 10 | 10 |

A summary of the general steps taken for full energy scans conducted on IVCS-6 and OVCS-7A. The first row indicates the energy range for each scan. The second shows the HOS filter used to reduce contamination from higher order harmonics. The third row indicates the number of steps in the energy range of row one. The last row indicates the exposure time per step or the amount of time each step is measured. Exposure times are long to reduce the strain on the monochromator.

To further constrain the spatial uniformity of the filters, filters are mapped using mesh scans which varies the position of the beam across the filters at fixed energies, and can be used to calculate the transmission across the whole filter as shown in Figure 2.12 and Figure 2.13. Here these are shown with an arbitrary position axis which are in units of millimeters. These axes represent the position of the sample within the chamber, which in a Cartesian two dimensional plane, would represent the x and y axes within the sample chamber. While the z axis (which was not changed) represents the axis along the direction of the beam. Here the location of coarse mesh cells used for full energy scans are shown. Embedded on these maps, within the coarse mesh cells are locations of 5x5 mesh scans (shown as x's) performed over both coarse cells in both filters to show the relative transmission of the fine mesh. These maps show that differences in transmission of coarse mesh cells are at most 1.5%, but otherwise agree quite well across cells, especially at higher energies.

In Eckart et al. (2018), they fit a model to their data which was comprised of a silicon mesh with a uniform Al and polyimide film. They found that this was insufficient to match the data. Subsequent inspection of filters indicate that the epoxy which binds the mesh to the filters beyond the 5 $\mu$m fine wide mesh bars was non-uniform across each filter. They found that including a component describing a partial covering fraction due to the coarse (mesh filling fraction) and fine mesh (epoxy filling fraction) improved the model's fit to the data. In this calibration of the *XRISM* filters, the same model is used to fit to our data.

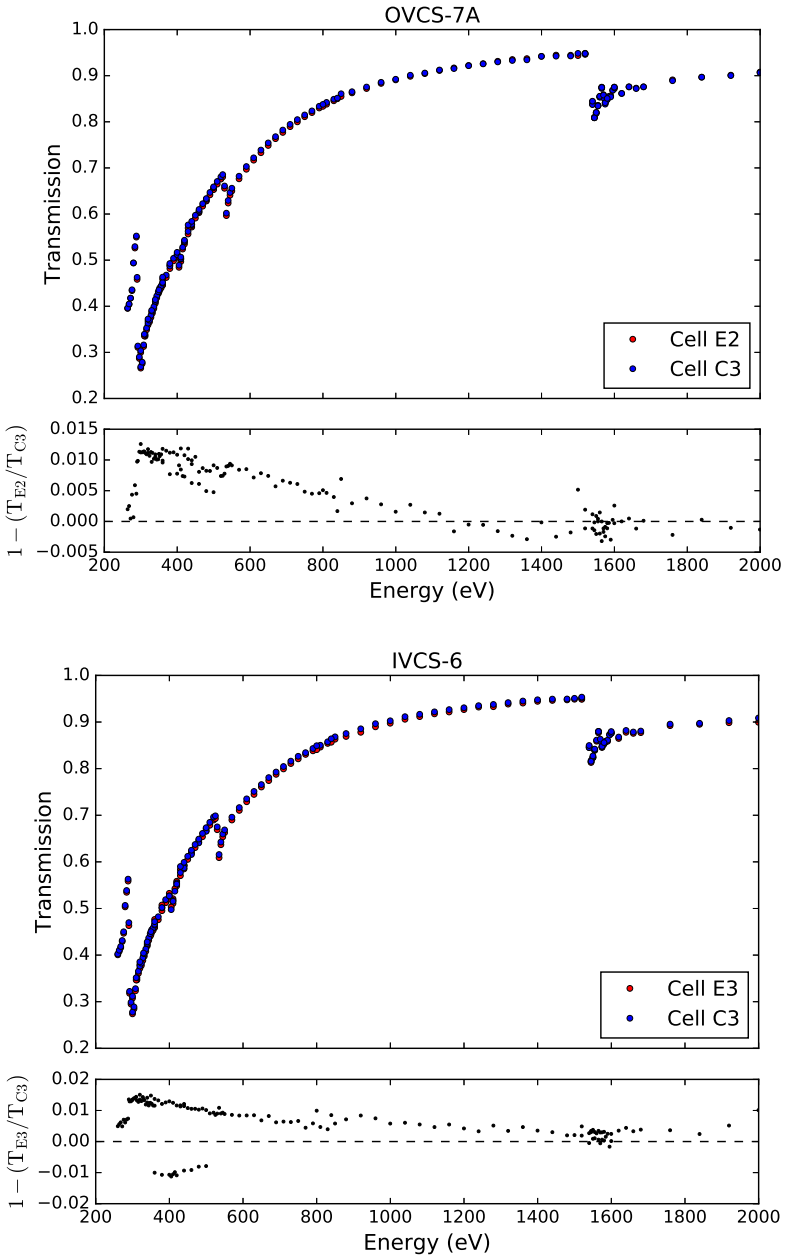


Figure 2.11: Full energy transmission scans of OVCS-7A and IVCS-6 (top to bottom respectively) of two different coarse mesh locations in each filter. Coarse mesh locations were chosen to minimize translation of mounted filters while being distant enough to probe the uniformity of the filters. Bottom panel of each plot shows the transmission fractional difference between cells labelled C3, $T_{C3}$, and the cells labelled E2, $T_{E2}$, and E3, $T_{E3}$.

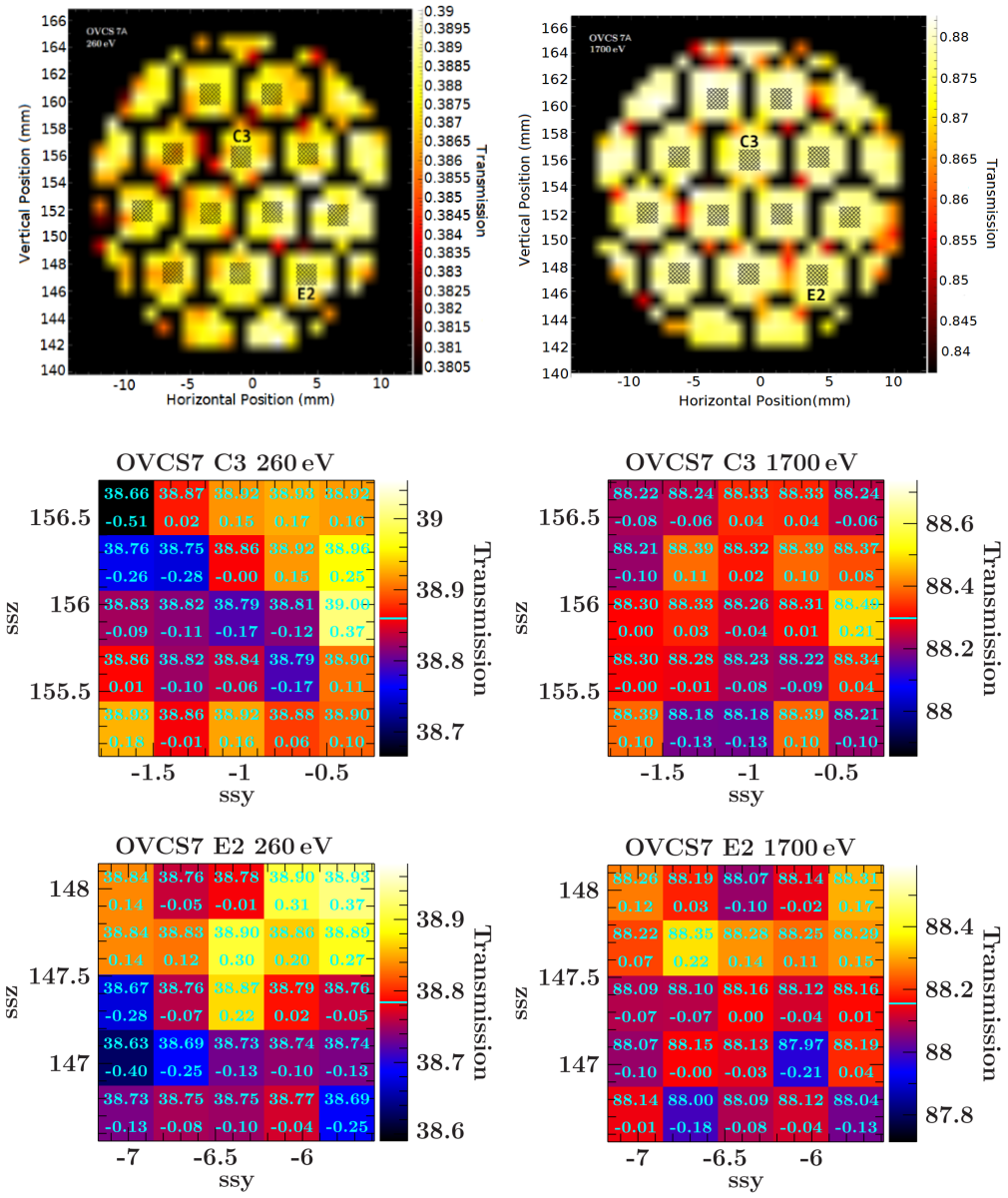


Figure 2.12: Top row are spatial uniformity maps of the OVCS-7A at 260 eV and 1700 eV. These are shown with arbitrary position axis, where the horizontal and the vertical position of the sample in the chamber are shown in units of millimeters. The crosses ('x') represent the positions of 5x5 mesh scans shown in the middle and bottom row. The top number in each cell shows the transmission at that position, with the bottom number showing the average percentage difference, $(T/T_{\text{avg}} - 1) \times 100\%$.

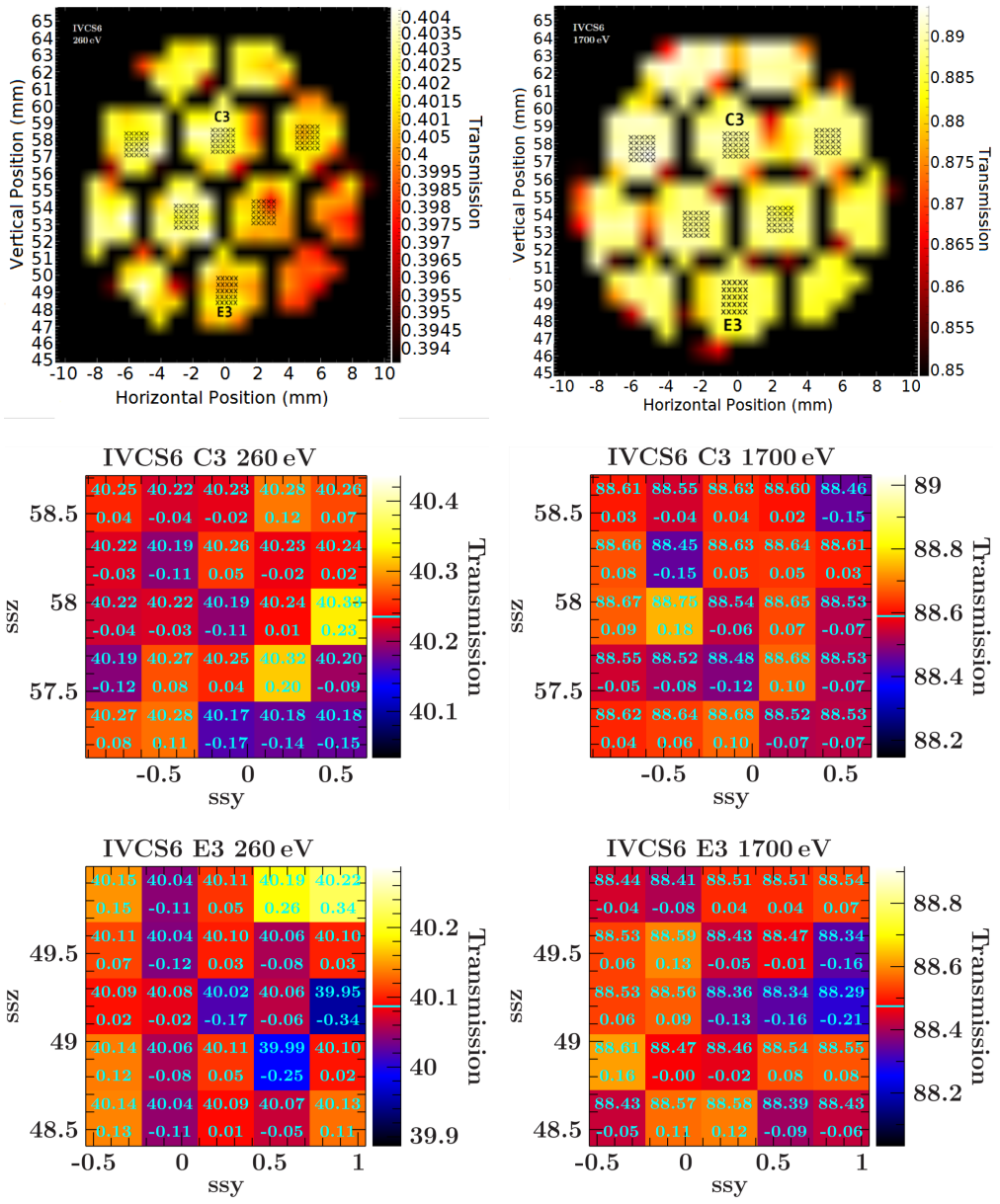


Figure 2.13: Continued−Spatial uniformity maps of IVCS-6. Everything is the same as in Figure 2.12

### 2.5.1 Modelling and Filter Parameters

The broadband measurements of the filters are modelled with free parameters for the polyimide thickness, Al thickness, the surface oxide contamination on the Al films, as well as the mesh filling fraction, epoxy filling fraction, and the epoxy thickness. Broadband transmission scans shown in Figure 2.11 are used as an input to the modelling. The atomic transmission models use absorption cross sections from Henke et al., which are interpolated to match the energies of transmission scans. The absorption coefficients due to the individual components of the polyimide films (C, N, O, H) are taken from Figure 2.4, whereas the absorption coefficient for the aluminum films and excess surface oxide residing on these films, $\Sigma_O$, are taken from Figure 2.14.

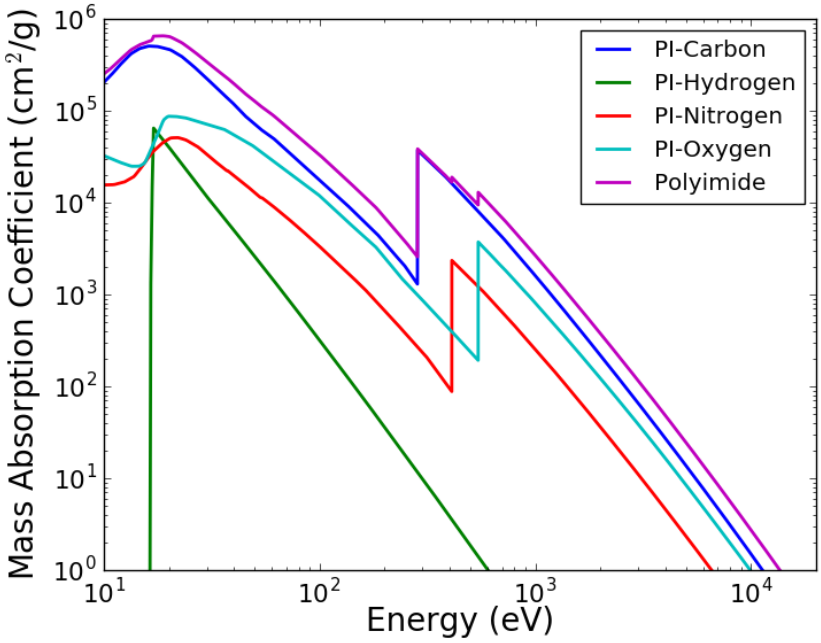


Figure 2.14: The absorption coefficients for the individual components of polyimide, which has a stoichiometry of $C_{22}H_{10}N_2O_4$. The sum of the individual components recover the magenta curve.

The transmission through the Al films was obtained by varying the surface density of Al, $\Sigma_{Al}$, and is given by,

$$T_{\mathrm{Al}} = \exp\left(-\Sigma_{\mathrm{Al}}\mu_{\mathrm{Al}}\right). \tag{2.6}$$

Assuming a mass volume density for Al, $\rho_{\mathrm{Al}} = 2.7$ g cm$^{-3}$, one can obtain the thickness of the aluminum film by,

$$t_{\mathrm{Al}} = \frac{\Sigma_{\mathrm{Al}}}{\rho_{\mathrm{Al}}}. \tag{2.7}$$

To model the transmission through the polyimide film requires that the individual components be modelled to obtain the purple curve in Figure 2.14, with the areal density of polyimide being varied, $\Sigma_{\mathrm{PI}}$, such that the transmission is given by,

$$T_{\mathrm{PI}} = \exp\left(-\Sigma_{\mathrm{PI}}\mu_{\mathrm{PI}}\right). \tag{2.8}$$

Assuming a mass volumetric density of, $\rho_{\mathrm{PI}} = 1.43$ g cm$^{-3}$, the thickness of polyimide is given by,

$$t_{\mathrm{PI}} = \frac{\Sigma_{\mathrm{PI}}}{\rho_{\mathrm{PI}}}. \tag{2.9}$$

Through the same processes as described above, the transmission through the surface oxygen on Al films is obtained by,

$$T_{\mathrm{O}} = \exp(-\Sigma_{\mathrm{O}}\mu_{\mathrm{O}}). \tag{2.10}$$

The hexagonal Si coarse and fine mesh thicknesses were fixed to their respective values of 225 $\mu$m and 25 $\mu$m. The transmission through these meshes is obtained by varying the filling fraction of both of coarse and fine mesh cells, $f$. The filling fraction may be thought of as the fraction of the filter covered or blocked by the bars of these meshes. The transmission due to either the coarse or fine mesh is given by,

$$T_{\mathrm{Mesh}} = (1 - f) + f\exp(-\Sigma_{\mathrm{Si}}\mu_{\mathrm{Si}}), \tag{2.11}$$

where $\Sigma_{\mathrm{Si}}$ (in units of g cm$^{-3}$) is obtained using, $\Sigma_{\mathrm{Si}} = 10^{-4}\rho_{\mathrm{Si}}t_{\mathrm{Si}}$, assuming that $\rho_{\mathrm{Si}} = 2.33$ g cm$^{-3}$ and $\mathrm{t_{Si}} = 25$ $\mu$m. The modelling of epoxy assumes a distribution of thicknesses, $0 < t < t_{\mathrm{max}}$, with a total epoxy filling fraction, $f_{\mathrm{ep}}$. The distribution of epoxy throughout modelling was chosen to be linear, but as explained in Eckart et al. (2018), the model

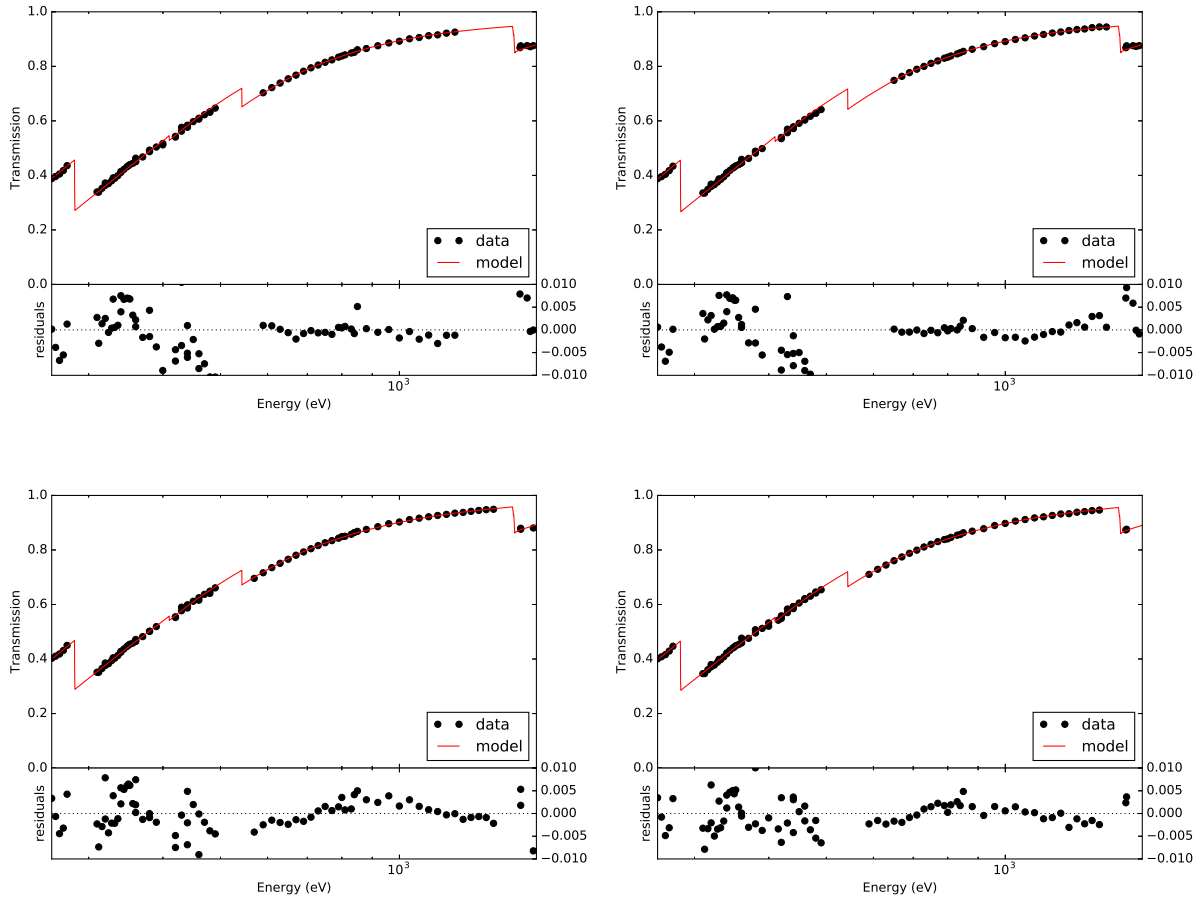


Figure 2.15: The models used to fit the data and obtain filter parameters in Table 2.3, the model has no edge structure included in it, hence the exclusion of points at edges. The top row from left to right are the models for cells C3 and E2 for OVCS-7A. The bottom row from left to right are the models for cells C3 and E3 for IVCS-6.

transmission is not significantly affected by the chosen distribution of epoxy. Assuming that epoxy has the same stoichiometry as polyimide, with a mass volume density of 1.43 g cm$^{-3}$. The epoxy surface density, $\Sigma_{\text{ep}}$, and $f_{\text{ep}}$ are modelled as free parameters with the transmission through epoxy given by,

Table 2.3: **Best Fitting Film and Mesh Parameters**

| Filter | Scan | $t_{Al}$ (Å) | $t_{PI}$ (Å) | $\Sigma_O(10^6$ g cm$^2)$ | Fine Mesh Epoxy | | Fine Mesh | | Coarse Mesh | |
|---|---|---|---|---|---|---|---|---|---|---|
| | | | | | $f_{ep}$ | t($\mu$m) | f | t($\mu$m) | f | t($\mu$m) |
| IVCS-6 | Cell C3 | $843.6 \pm 6.1$ | $980.9 \pm 17.2$ | $2.20 \pm 0.3$ | 0.040 | 8.33 | 0.0127 | 25 | 0.0180 | 225 |
| | Cell E3 | $844.5 \pm 6.3$ | $998.6 \pm 19.1$ | $2.39 \pm 0.3$ | 0.045 | 8.33 | 0.0142 | 25 | 0.0182 | 225 |
| OVCS-7A | Cell C3 | $925.9 \pm 5.0$ | $950.3 \pm 23.3$ | $2.00 \pm 0.5$ | 0.013 | 8.91 | 0.0290 | 25 | 0.0307 | 225 |
| | Cell E2 | $925.9 \pm 11.3$ | $965.9 \pm 24.6$ | $1.99 \pm 0.6$ | 0.012 | 8.43 | 0.0275 | 25 | 0.0314 | 225 |

**Columns** from left to right are: The optical blocking filter, the corresponding coarse mesh cell used in modelling, thickness of aluminum, thickness of polyimide where it's assumed to have the same composition as polyimide with, $C_{22}H_{10}N_2O_4$, the areal density of excess oxygen as specified by Luxel Corp. The fine support mesh filling factor and thickness, the maximum epoxy filling factor and thickness, as well as the coarse mesh filling factor and thickness. All filling factors are determined via fitting using modelling described in Section 2.5.1.

$$T_{ep} = 1 - f_{ep}\left[1 - \frac{2}{\Sigma_{ep}\mu_{PI}} + \left(\frac{2}{\exp\left(-2\Sigma_{ep}\mu_{PI}\right)}\right)\left(1 - \exp\left(-\Sigma_{ep}\mu_{PI}\right)\right)\right]. \tag{2.12}$$

All measurements were made at room temperature, and the model includes no changes to the fine structure due to the filter temperature. Moreover, this model contains no edge structure due to the epoxy and mesh covering fractions. For this reason, points around the edge are removed from the model during fitting to obtain the most accurate values for fitted parameters. The best fitting model for both cells in each filter are shown in Figure 2.15. The best fitting film and mesh parameters are shown in Table 2.3.

The model parameters for both coarse mesh cells agree fairly well with each other in both filters, with the largest discrepancies seen in the fine mesh filling fraction and thickness of polyimide for IVCS-6 and OVCS-7A, respectively. Although these are minimal, with the largest difference in $t_{Al}$ being about 2%. Compared to the previous calibration of *Hitomi* (Eckart et al., 2018), the model thicknesses of aluminum and polyimide are both lower than expected for the IVCS and OVCS filter, although the surface oxide component is similar. The epoxy filling fraction is high in IVCS-6 ($\sim 4\%$) in both cells compared to the

calibration of previous IVCS flight filters (1.6%), yet is lower than non-flight EM filters (11.5%) (Eckart et al., 2018). The best-fitting model filling fractions for OVCS-7A also agrees fairly well with previous calibrations of OVCS filters (Eckart et al., 2018). These models show that filters are within the expected tolerance range for filling fractions, but differ slightly in terms of polyimide and aluminum thicknesses.

## 2.6 Conclusions

In this chapter, I presented my work during a calibration of two optical blocking filters. In this final section, the results of calibration are summarized along with notes on the future goals before *XRISM*'s expected launch in 2020.

### 2.6.1 Summary

The calibration of IVCS-6 and OVCS-7A to be installed on Resolve was performed at the CLS between January 28 to February 8 in 2019. A satellite endstation was commissioned and installed at the REXIS beamline to be used during calibration, as shown in Figure 2.8. Full energy scans were conducted over two coarse mesh cells in IVCS-6 (C3, E2) and OVCS-7A (C3, E3) in the energy range of 260-2000 eV. This was done in multiple steps to switch in different HOS filters and to reduce the strain on the monochromator. The resulting transmission through both coarse cells were plotted and shown over the full energy range in Figure 2.11.

To confirm the spatial uniformity of filters, mesh scans were conducted over the full filter showing the transmission through coarse cells, as well as over the fine mesh within coarse cells at fixed energies of 260 eV and 1700 eV. This is shown in Figure 2.12 and Figure 2.13. These maps, and the full energy scan suggest that differences in transmission across the optical blocking filters are at most 1.5%.

Full energy scans shown in Figure 2.15 were modelled and used to fit for filter parameters. These include the thickness of polyimide, aluminum, surface oxide, epoxy, as well as filling factors of the coarse mesh, fine mesh, and epoxy. The results of these are shown in Table 2.3. Compared to the modelling of previous IVCS and OVCS filters during *Hitomi*, the filling factor for OVCS-7A agrees well with previous calibrations. On the other hand, the epoxy filling factor for IVCS-6 is about 2% higher than in modelling of previous IVCS filters. Moreover, modelling of aluminum and polyimide thicknesses are both lower than expected for IVCS and OVCS filters, although the surface oxide component agrees well.

### 2.6.2 Future Work

While these calibrations of a few Resolve filters have been successful, several more filters need to be calibrated, such as: DA, CTS, and DMS optical blocking filters. These will need to be calibrated to determine these filters' uniformity as well as their thicknesses and filling factor before the launch of *XRISM*, sometime in 2020. Moreover, the model used for fitting will need to be updated to include edge structure so that points around edges will be correctly modelled and used in calculating film parameters with a higher degree of accuracy.

# References


I. Agudo, M. Boettcher, H. D. E. Falcke, M. Georganopoulos, G. Ghisellini, G. Giovannini, M. Giroletti, L. Gurvits, J. L. Gómez, R. Laing, M. Lister, J. M. Martí, E. Meyer, Y. Mizuno, S. O'Sullivan, P. Padovani, Z. Paragi, M. Perucho, D. Schleicher, L. Stawarz, N. Vlahakis, and J. Wardle. Studies of Relativistic Jets in Active Galactic Nuclei with SKA. *Advancing Astrophysics with the Square Kilometre Array (AASKA14)*, art. 93, April 2015.

S. W. Allen and A. C. Fabian. The relationship between cooling flows and metallicity measurements for X-ray-luminous clusters. , 297(3):L63–L68, Jul 1998. doi: 10.1046/j.1365-8711.1998.01738.x.

J. Als-Nielsen and D. McMorrow. *Elements of Modern X-ray Physics*. 2011.

E. Anders and N. Grevesse. Abundances of the elements - Meteoritic and solar. , 53:197–214, January 1989. doi: 10.1016/0016-7037(89)90286-X.

K. A. Arnaud. XSPEC: The First Ten Years. In G. H. Jacoby and J. Barnes, editors, *Astronomical Data Analysis Software and Systems V*, volume 101 of *Astronomical Society of the Pacific Conference Series*, page 17, 1996.

Y. Ascasibar and M. Markevitch. The Origin of Cold Fronts in the Cores of Relaxed Galaxy Clusters. , 650:102–127, October 2006. doi: 10.1086/506508.

D. Attwood. Soft x-rays and extreme ultraviolet radiation : principles and applications. In *Soft x-rays and extreme ultraviolet radiation : principles and applications / Cambridge ; New York : Cambridge University Press*, Jan 2000.

L. Bîrzan, D. A. Rafferty, B. R. McNamara, M. W. Wise, and P. E. J. Nulsen. A Systematic Study of Radio-induced X-Ray Cavities in Clusters, Groups, and Galaxies. , 607:800–809, June 2004. doi: 10.1086/383519.

L. Bîrzan, B. R. McNamara, P. E. J. Nulsen, C. L. Carilli, and M. W. Wise. Radiative Efficiency and Content of Extragalactic Radio Sources: Toward a Universal Scaling Relation between Jet Power and Radio Power. , 686:859–880, October 2008. doi: 10.1086/591416.

L. Bîrzan, D. A. Rafferty, P. E. J. Nulsen, B. R. McNamara, H. J. A. Röttgering, M. W. Wise, and R. Mittal. The duty cycle of radio-mode feedback in complete samples of clusters. , 427:3468–3488, December 2012. doi: 10.1111/j.1365-2966.2012.22083.x.

H. Boehringer and N. Werner. X-ray Spectroscopy of Galaxy Clusters. *arXiv e-prints*, July 2009.

H. Böhringer and N. Werner. X-ray spectroscopy of galaxy clusters: studying astrophysical processes in the largest celestial laboratories. , 18:127–196, February 2010. doi: 10.1007/s00159-009-0023-3.

G. Branduardi-Raymont, D. Fabricant, E. Feigelson, P. Gorenstein, J. Grindlay, A. Soltan, and G. Zamorani. Soft X-ray images of the central region of the Perseus cluster. , 248:55–60, August 1981. doi: 10.1086/159129.

Michael J. I. Brown, Buell T. Jannuzi, David J. E. Floyd, and Jeremy R. Mould. The Ubiquitous Radio Continuum Emission from the Most Massive Early-type Galaxies. , 731:L41, April 2011. doi: 10.1088/2041-8205/731/2/L41.

M. S. Calzadilla, H. R. Russell, M. McDonald, A. C. Fabian, S. A. Baum, F. Combes, M. Donahue, A. C. Edge, B. R. McNamara, P. E. J. Nulsen, C. P. O'Dea, J. B. R. Oonk, G. R. Tremblay, and A. N. Vantyghem. Revealing a Highly-Dynamic Cluster Core in Abell 1664 with Chandra. *ArXiv e-prints*, October 2018.

K. W. Cavagnolo, M. Donahue, G. M. Voit, and M. Sun. An Entropy Threshold for Strong H$\alpha$ and Radio Emission in the Cores of Galaxy Clusters. , 683:L107, August 2008. doi: 10.1086/591665.

K. W. Cavagnolo, B. R. McNamara, P. E. J. Nulsen, C. L. Carilli, C. Jones, and L. Bîrzan. A Relationship Between AGN Jet Power and Radio Power. , 720:1066–1072, September 2010. doi: 10.1088/0004-637X/720/2/1066.

Kenneth W. Cavagnolo, Megan Donahue, G. Mark Voit, and Ming Sun. Intracluster Medium Entropy Profiles for a Chandra Archival Sample of Galaxy Clusters. , 182(1):12–32, May 2009. doi: 10.1088/0067-0049/182/1/12.

A. Cavaliere and R. Fusco-Femiano. X-rays from hot plasma in clusters of galaxies. , 49: 137–144, May 1976.

E. Churazov, M. Brüggen, C. R. Kaiser, H. Böhringer, and W. Forman. Evolution of Buoyant Bubbles in M87. , 554:261–273, June 2001. doi: 10.1086/321357.

T. E. Clarke, Juan M. Uson, C. L. Sarazin, and E. L. Blanton. Soft X-Ray Absorption Due to a Foreground Edge-on Spiral Galaxy toward the Core of A2029. , 601(2):798–804, Feb 2004. doi: 10.1086/380819.

J. J. Condon, W. D. Cotton, E. W. Greisen, Q. F. Yin, R. A. Perley, G. B. Taylor, and J. J. Broderick. The NRAO VLA Sky Survey. , 115:1693–1716, May 1998. doi: 10.1086/300337.

J. J. Condon, W. D. Cotton, and J. J. Broderick. Radio Sources and Star Formation in the Local Universe. , 124:675–689, August 2002. doi: 10.1086/341650.

L. L. Cowie, A. C. Fabian, and P. E. J. Nulsen. NGC 1275 and the Perseus cluster - The formation of optical filaments in cooling gas in X-ray clusters. , 191:399–410, May 1980. doi: 10.1093/mnras/191.2.399.

L. L. Cowie, E. M. Hu, E. B. Jenkins, and D. G. York. Two-dimensional spectrophotometry of the cores of X-ray luminous clusters. , 272:29–47, September 1983. doi: 10.1086/161259.

C. S. Crawford, S. W. Allen, H. Ebeling, A. C. Edge, and A. C. Fabian. The ROSAT Brightest Cluster Sample - III. Optical spectra of the central cluster galaxies. , 306(4): 857–896, Jul 1999. doi: 10.1046/j.1365-8711.1999.02583.x.

J. H. Croston, J. Ineson, and M. J. Hardcastle. Particle content, radio-galaxy morphology, and jet power: all radio-loud AGN are not equal. , 476:1614–1623, May 2018. doi: 10.1093/mnras/sty274.

Weiguang Cui, Chris Power, Veronica Biffi, Stefano Borgani, Giuseppe Murante, Dunja Fabjan, Alexander Knebe, Geraint F. Lewis, and Greg B. Poole. How does our choice of observable influence our estimation of the centre of a galaxy cluster? Insights from cosmological simulations. , 456(3):2566–2575, Mar 2016. doi: 10.1093/mnras/stv2839.

J. Cutler, D. Chapman, and R. Lamb. The Brightest Light in Canada: The Canadian Light Source. *Quantum Beam Science*, 2017.

J. N. Cutler, E. Hallin, M. Dalzell, M. De Jong, T. Ellis, and W. Thomlinson. Progress at Canada's National Synchrotron Facility: The Canadian Light Source. *Physics in Canada*, 63(3), Sept 2007.

Laurence P. David and Paul E. J. Nulsen. The Extended Fe Distribution in the Intracluster Medium and the Implications Regarding AGN Heating. , 689(2):837–850, Dec 2008. doi: 10.1086/592239.

S. de Grandi and S. Molendi. A Study of the Radial Metallicity Distributions for a Sample of Galaxy Clusters Observed with BeppoSAX. In Riccardo Giacconi, Salvatore Serio, and Luigi Stella, editors, *X-ray Astronomy 2000*, volume 234 of *Astronomical Society of the Pacific Conference Series*, page 381, Jan 2001.

S. De Grandi, S. Ettori, M. Longhetti, and S. Molendi. On the iron content in rich nearby clusters of galaxies. , 419:7–18, May 2004. doi: 10.1051/0004-6361:20034228.

D. S. De Young. The Particle Content of Extragalactic Jets. , 648:200–208, September 2006. doi: 10.1086/505861.

R. J. H. Dunn and A. C. Fabian. Investigating AGN heating in a sample of nearby clusters. , 373(3):959–971, Dec 2006. doi: 10.1111/j.1365-2966.2006.11080.x.

R. J. H. Dunn and A. C. Fabian. Investigating heating and cooling in the BCS and B55 cluster samples. , 385(2):757–768, Apr 2008. doi: 10.1111/j.1365-2966.2008.12898.x.

R. J. H. Dunn, A. C. Fabian, and G. B. Taylor. Radio bubbles in clusters of galaxies. , 364:1343–1353, December 2005. doi: 10.1111/j.1365-2966.2005.09673.x.

Megan E. Eckart, Joseph S. Adams, Kevin R. Boyce, Gregory V. Brown, Meng P. Chiao, Ryuichi Fujimoto, Daniel Haas, Jan-Willem den Herder, Akio Hoshino, Yoshitaka Ishisaki, Caroline A. Kilbourne, Shunji Kitamoto, Maurice A. Leutenegger, Dan McCammon, Kazuhisa Mitsuda, F. Scott Porter, Kosuke Sato, Makoto Sawada, Hiromi Seta, Gary A. Sneiderman, Andrew E. Szymkowiak, Yoh Takei, Makoto S. Tashiro, Masahiro Tsujimoto, Cor P. de Vries, Tomomi Watanabe, Shinya Yamada, and Noriko Y. Yamasaki. Ground calibration of the Astro-H (Hitomi) soft x-ray spectrometer. *Journal of Astronomical Telescopes, Instruments, and Systems*, 4:021406, Apr 2018. doi: 10.1117/1.JATIS.4.2.021406.

A. C. Edge. Molecular Gas in Cluster Cooling Flows. In J. E. Hibbard, M. Rupen, and J. H. van Gorkom, editors, *Gas and Galaxy Evolution*, volume 240 of *Astronomical Society of the Pacific Conference Series*, page 567, 2001.

A. C. Edge and G. C. Stewart. EXOSAT observations of clusters of galaxies - I. The X-ray data. , 252:414, Oct 1991. doi: 10.1093/mnras/252.3.414.

A. C. Fabian. Cooling Flows in Clusters of Galaxies. , 32:277–318, 1994. doi: 10.1146/annurev.aa.32.090194.001425.

A. C. Fabian, P. E. J. Nulsen, and G. C. Stewart. Star formation in a galactic wind. , 287: 613, October 1980. doi: 10.1038/287613a0.

A. C. Fabian, J. S. Sanders, G. B. Taylor, S. W. Allen, C. S. Crawford, R. M. Johnstone, and K. Iwasawa. A very deep Chandra observation of the Perseus cluster: shocks, ripples and conduction. , 366:417–428, February 2006. doi: 10.1111/j.1365-2966.2005.09896.x.

D. Fisher, G. Illingworth, and M. Franx. Kinematics of 13 brightest cluster galaxies. , 438: 539–562, January 1995. doi: 10.1086/175100.

P. E. Freeman, V. Kashyap, R. Rosner, and D. Q. Lamb. A Wavelet-Based Algorithm for the Spatial Analysis of Poisson Data. , 138:185–218, January 2002. doi: 10.1086/324017.

Yasushi Fukazawa, Takaya Ohashi, Andrew C. Fabian, Claude R. Canizares, Yasushi Ikebe, Kazuo Makishima, Richard F. Mushotzky, and Koujun Yamashita. Metal Concentration and X-Ray Cool Spectral Component in the Central Region of the Centaurus Cluster of Galaxies. , 46:L55–L58, Jun 1994.

M. Gaspari, M. Ruszkowski, and P. Sharma. Cause and Effect of Feedback: Multiphase Gas in Cluster Cores Heated by AGN Jets. , 746:94, February 2012. doi: 10.1088/0004-637X/746/1/94.

M. Gaspari, M. Ruszkowski, and S. Peng Oh. Chaotic cold accretion on to black holes. , 432(4):3401–3422, Jul 2013. doi: 10.1093/mnras/stt692.

M. Gaspari, M. McDonald, S. L. Hamer, F. Brighenti, P. Temi, M. Gendron-Marsolais, J. Hlavacek-Larrondo, A. C. Edge, N. Werner, P. Tozzi, M. Sun, J. M. Stone, G. R. Tremblay, M. T. Hogan, D. Eckert, S. Ettori, H. Yu, V. Biffi, and S. Planelles. Shaken Snow Globes: Kinematic Tracers of the Multiphase Condensation Cascade in Massive Galaxies, Groups, and Clusters. , 854:167, February 2018. doi: 10.3847/1538-4357/aaaa1b.

Matthew R. George, Alexie Leauthaud, Kevin Bundy, Alexis Finoguenov, Chung-Pei Ma, Eli S. Rykoff, Jeremy L. Tinker, Risa H. Wechsler, Richard Massey, and Simona Mei. Galaxies in X-Ray Groups. II. A Weak Lensing Study of Halo Centering. , 757(1):2, Sep 2012. doi: 10.1088/0004-637X/757/1/2.

H. Gursky. The X-Ray Emission from Rich Clusters of Galaxies. , 85:493, October 1973. doi: 10.1086/129494.

H. Gursky and D. A. Schwartz. Extragalactic X-ray sources. , 15:541–568, 1977. doi: 10.1146/annurev.aa.15.090177.002545.

S. L. Hamer, A. C. Edge, A. M. Swinbank, J. B. R. Oonk, R. Mittal, B. R. McNamara, H. R. Russell, M. N. Bremer, F. Combes, A. C. Fabian, N. P. H. Nesvadba, C. P. O'Dea, S. A. Baum, P. Salomé, G. Tremblay, M. Donahue, G. J. Ferland, and C. L. Sarazin. Cold gas dynamics in Hydra-A: evidence for a rotating disc. , 437(1):862–878, Jan 2014. doi: 10.1093/mnras/stt1949.

B. L. Henke, E. M. Gullikson, and J. C. Davies. X-Ray Interactions: Photoabsorption, Scattering, Transmission and Reflection at E = 50-30,000 eV, Z = 1-92, journal = Atomic Data and Nuclear Data Tables, year =.

Aaron S. Hoffer, Megan Donahue, Amalia Hicks, and R. S. Barthelemy. Infrared and Ultraviolet Star Formation in Brightest Cluster Galaxies in the ACCEPT Sample. , 199 (1):23, Mar 2012. doi: 10.1088/0067-0049/199/1/23.

M. T. Hogan, A. C. Edge, J. Hlavacek-Larrondo, K. J. B. Grainge, S. L. Hamer, E. K. Mahony, H. R. Russell, A. C. Fabian, B. R. McNamara, and R. J. Wilman. A comprehensive study of the radio properties of brightest cluster galaxies. , 453(2):1201–1222, Oct 2015. doi: 10.1093/mnras/stv1517.

M. T. Hogan, B. R. McNamara, F. Pulido, P. E. J. Nulsen, H. R. Russell, A. N. Vantyghem, A. C. Edge, and R. A. Main. Mass Distribution in Galaxy Cluster Cores. , 837:51, March 2017a. doi: 10.3847/1538-4357/aa5f56.

M. T. Hogan, B. R. McNamara, F. A. Pulido, P. E. J. Nulsen, A. N. Vantyghem, H. R. Russell, A. C. Edge, I. Babyk, R. A. Main, and M. McDonald. The Onset of Thermally Unstable Cooling from the Hot Atmospheres of Giant Galaxies in Clusters: Constraints on Feedback Models. , 851:66, December 2017b. doi: 10.3847/1538-4357/aa9af3.

R. M. Johnstone, A. C. Fabian, and P. E. J. Nulsen. The optical spectra of central galaxies in southern clusters Evidence for star formation. , 224:75–91, January 1987. doi: 10.1093/mnras/224.1.75.

J. S. Kaastra, F. B. S. Paerels, F. Durret, S. Schindler, and P. Richter. Thermal Radiation Processes. , 134(1-4):155–190, Feb 2008. doi: 10.1007/s11214-008-9310-y.

P. M. W. Kalberla, W. B. Burton, D. Hartmann, E. M. Arnal, E. Bajaja, R. Morras, and W. G. L. Pöppel. The Leiden/Argentine/Bonn (LAB) Survey of Galactic HI. Final data release of the combined LDS and IAR surveys with improved stray-radiation corrections. , 440:775–782, September 2005. doi: 10.1051/0004-6361:20041864.

Jr. Kennicutt, Robert C. Star Formation in Galaxies Along the Hubble Sequence. , 36: 189–232, Jan 1998. doi: 10.1146/annurev.astro.36.1.189.

Lisa J. Kewley, Margaret J. Geller, Rolf A. Jansen, and Michael A. Dopita. The H$\alpha$ and Infrared Star Formation Rates for the Nearby Field Galaxy Survey. , 124(6):3135–3143, Dec 2002. doi: 10.1086/344487.

Caroline A. Kilbourne, Joseph S. Adams, Regis P. Brekosky, James A. Chervenak, Meng P. Chiao, Megan E. Eckart, Enectali Figueroa-Feliciano, Masimilliano Galeazzi, Christoph Grein, and Christine A. Jhabvala. Design, implementation, and performance of the Astro-H SXS calorimeter array and anticoincidence detector. *Journal of Astronomical Telescopes, Instruments, and Systems*, 4:011214, Jan 2018. doi: 10.1117/1.JATIS.4.1.011214.

C. C. Kirkpatrick and B. R. McNamara. Hot outflows in galaxy clusters. , 452:4361–4376, October 2015. doi: 10.1093/mnras/stv1574.

C. C. Kirkpatrick, M. Gitti, K. W. Cavagnolo, B. R. McNamara, L. P. David, P. E. J. Nulsen, and M. W. Wise. Direct Evidence for Outflow of Metal-Enriched Gas Along the Radio Jets of Hydra A. , 707:L69–L72, December 2009. doi: 10.1088/0004-637X/707/1/L69.

C. C. Kirkpatrick, B. R. McNamara, and K. W. Cavagnolo. Anisotropic Metal-enriched Outflows Driven by Active Galactic Nuclei in Clusters of Galaxies. , 731:L23, April 2011. doi: 10.1088/2041-8205/731/2/L23.

T. R. Lauer, M. Postman, M. A. Strauss, G. J. Graves, and N. E. Chisari. Brightest Cluster Galaxies at the Present Epoch. , 797:82, December 2014. doi: 10.1088/0004-637X/797/2/82.

Yuan Li, Greg L. Bryan, Mateusz Ruszkowski, G. Mark Voit, Brian W. O'Shea, and Megan Donahue. Cooling, AGN Feedback, and Star Formation in Simulated Cool-core Galaxy Clusters. , 811(2):73, Oct 2015. doi: 10.1088/0004-637X/811/2/73.

R. A. Main, B. R. McNamara, P. E. J. Nulsen, H. R. Russell, and A. N. Vantyghem. A relationship between halo mass, cooling, active galactic nuclei heating and the co-evolution of massive black holes. , 464(4):4360–4382, Feb 2017. doi: 10.1093/mnras/stw2644.

D. Makarov, P. Prugniel, N. Terekhova, H. Courtois, and I. Vauglin. HyperLEDA. III. The catalogue of extragalactic distances. , 570:A13, October 2014. doi: 10.1051/0004-6361/201423496.

M. Markevitch and A. Vikhlinin. Shocks and cold fronts in galaxy clusters. , 443:1–53, May 2007. doi: 10.1016/j.physrep.2007.01.001.

W. G. Mathews and J. C. Baker. Galactic Winds. , 170:241, December 1971. doi: 10.1086/151208.

M. McCourt, P. Sharma, E. Quataert, and I. J. Parrish. Thermal instability in gravitationally stratified plasmas: implications for multiphase structure in clusters and galaxy haloes. , 419:3319–3337, February 2012. doi: 10.1111/j.1365-2966.2011.19972.x.

Michael McDonald, Sylvain Veilleux, David S. N. Rupke, and Richard Mushotzky. On the Origin of the Extended H$\alpha$ Filaments in Cooling Flow Clusters. , 721(2):1262–1283, Oct 2010. doi: 10.1088/0004-637X/721/2/1262.

Michael McDonald, Sylvain Veilleux, David S. N. Rupke, Richard Mushotzky, and Christopher Reynolds. Star Formation Efficiency in the Cool Cores of Galaxy Clusters. , 734 (2):95, Jun 2011. doi: 10.1088/0004-637X/734/2/95.

B. R. McNamara and P. E. J. Nulsen. Heating Hot Atmospheres with Active Galactic Nuclei. , 45:117–175, September 2007. doi: 10.1146/annurev.astro.45.051806.110625.

B. R. McNamara, H. R. Russell, P. E. J. Nulsen, M. T. Hogan, A. C. Fabian, F. Pulido, and A. C. Edge. A Mechanism for Stimulating AGN Feedback by Lifting Gas in Massive Galaxies. , 830(2):79, Oct 2016. doi: 10.3847/0004-637X/830/2/79.

John S. Mulchaey. X-ray Properties of Groups of Galaxies. , 38:289–335, Jan 2000. doi: 10.1146/annurev.astro.38.1.289.

R. Mushotzky, M. Loewenstein, K. A. Arnaud, T. Tamura, Y. Fukazawa, K. Matsushita, K. Kikuchi, and I. Hatsukade. Measurement of the Elemental Abundances in Four Rich Clusters of Galaxies. I. Observations. , 466:686, Aug 1996. doi: 10.1086/177541.

R. F. Mushotzky and M. Loewenstein. Lack of Evolution in the Iron Abundance in Clusters of Galaxies and Implications for the Global Star Formation Rate at High Redshift. , 481 (2):L63–L66, Jun 1997. doi: 10.1086/310651.

R. F. Mushotzky, P. J. Serlemitsos, B. W. Smith, E. A. Boldt, and S. S. Holt. OSO 8 X-ray spectra of clusters of galaxies. I - Observations of twenty clusters: Physical correlations. , 225:21–39, October 1978. doi: 10.1086/156465.

Hiroyuki Nakanishi, Tomoka Tosaki, Kotaro Kohno, Yoshiaki Sofue, and Nario Kuno. ASTE $^{12}$CO(J= 3–2) Survey of Elliptical Galaxies. , 59:61–65, Feb 2007. doi: 10.1093/pasj/59.1.61.

M. Newville. Fundamentals of XAFS. unpublished, 2004.

P. E. J. Nulsen. Thermal instability in cooling flows. , 221:377–392, July 1986. doi: 10.1093/mnras/221.2.377.

P. E. J. Nulsen, S. L. Powell, and A. Vikhlinin. Model-independent X-ray Mass Determinations. , 722:55–64, October 2010. doi: 10.1088/0004-637X/722/1/55.

C. P. O'Dea, S. A. Baum, J. Mack, A. M. Koekemoer, and A. Laor. Hubble Space Telescope STIS Far-Ultraviolet Observations of the Central Nebulae in the Cooling-Core Clusters A1795 and A2597. , 612:131–151, September 2004. doi: 10.1086/422402.

N. Okabe, K. Umetsu, T. Tamura, Y. Fujita, M. Takizawa, K. Matsushita, Y. Fukazawa, T. Futamase, M. Kawaharada, S. Miyazaki, Y. Mochizuki, K. Nakazawa, T. Ohashi, N. Ota, T. Sasaki, K. Sato, and S. I. Tam. Central mass profiles of the nearby cool-core galaxy clusters Hydra A and A478. , 456(4):4475–4487, Mar 2016. doi: 10.1093/mnras/stv2916.

E. O'Sullivan, F. Combes, P. Salomé, L. P. David, A. Babul, J. M. Vrtilek, J. Lim, V. Olivares, S. Raychaudhury, and G. Schellenberger. Cold gas in a complete sample of group-dominant early-type galaxies. , 618:A126, Oct 2018. doi: 10.1051/0004-6361/201833580.

E. K. Panagoulia, A. C. Fabian, J. S. Sanders, and J. Hlavacek-Larrondo. A volume-limited sample of X-ray galaxy groups and clusters - II. X-ray cavity dynamics. , 444 (2):1236–1259, Oct 2014. doi: 10.1093/mnras/stu1499.

I. J. Parrish, E. Quataert, and P. Sharma. Anisotropic Thermal Conduction and the Cooling Flow Problem in Galaxy Clusters. , 703:96–108, September 2009. doi: 10.1088/0004-637X/703/1/96.

R. Paterno-Mahler, E. L. Blanton, S. W. Randall, and T. E. Clarke. Deep Chandra Observations of the Extended Gas Sloshing Spiral in A2029. , 773:114, August 2013. doi: 10.1088/0004-637X/773/2/114.

J. R. Peterson and A. C. Fabian. X-ray spectroscopy of cooling clusters. , 427:1–39, April 2006. doi: 10.1016/j.physrep.2005.12.007.

F. Pizzolato and N. Soker. On the Nature of Feedback Heating in Cooling Flow Clusters. , 632:821–830, October 2005a. doi: 10.1086/444344.

F. Pizzolato and N. Soker. On the Nature of Feedback Heating in Cooling Flow Clusters. , 632:821–830, October 2005b. doi: 10.1086/444344.

E. Pointecouteau, M. Arnaud, and G. W. Pratt. The structural and scaling properties of nearby galaxy clusters. I. The universal mass profile. , 435:1–7, May 2005. doi: 10.1051/0004-6361:20042569.

F. A. Pulido, B. R. McNamara, A. C. Edge, M. T. Hogan, A. N. Vantyghem, H. R. Russell, P. E. J. Nulsen, I. Babyk, and P. Salomé. The Origin of Molecular Clouds in Central Galaxies. , 853:177, February 2018. doi: 10.3847/1538-4357/aaa54b.

D. A. Rafferty, B. R. McNamara, P. E. J. Nulsen, and M. W. Wise. The Feedback-regulated Growth of Black Holes and Bulges through Gas Accretion and Starbursts in Cluster Central Dominant Galaxies. , 652:216–231, November 2006. doi: 10.1086/507672.

D. A. Rafferty, B. R. McNamara, and P. E. J. Nulsen. The Regulation of Cooling and Star Formation in Luminous Galaxies by Active Galactic Nucleus Feedback and the Cooling-Time/Entropy Threshold for the Onset of Star Formation. , 687:899-918, November 2008. doi: 10.1086/591240.

P. Rebusco, E. Churazov, H. Böhringer, and W. Forman. Impact of stochastic gas motions on galaxy cluster abundance profiles. , 359(3):1041–1048, May 2005. doi: 10.1111/j.1365-2966.2005.08965.x.

E. Roediger, M. Brüggen, A. Simionescu, H. Böhringer, E. Churazov, and W. R. Forman. Gas sloshing, cold front formation and metal redistribution: the Virgo cluster as a quantitative test case. , 413:2057–2077, May 2011. doi: 10.1111/j.1365-2966.2011.18279.x.

E. Roediger, L. Lovisari, R. Dupke, S. Ghizzardi, M. Brüggen, R. P. Kraft, and M. E. Machacek. Gas sloshing, cold fronts, Kelvin-Helmholtz instabilities and the merger

history of the cluster of galaxies Abell 496. , 420:3632–3648, March 2012. doi: 10.1111/j.1365-2966.2011.20287.x.

Elke Roediger. Gas sloshing, cold front formation, and metal redistribution: the Virgo cluster as a quantitative test case. In *Galaxy Clusters: Observations, Physics and Cosmology*, page 19, Jul 2010.

M. Rothschild, M. W. Horn, C. L. Keast, R. R. Kunz, V. Liberman, Palmateer S. C., S. P. Doran, A. R. Forte, R. B. Goodman, Uttaro Sedlacek, J. H. C., R. S., D. Corliss, and A. Grenville. Photolithography at 193 nm. 10, 1997.

Mordechai Rothschild. Photolithography at wavelengths below 200 nm, 1998. URL https://doi.org/10.1117/12.309515.

H. R. Russell, J. S. Sanders, and A. C. Fabian. Direct X-ray spectral deprojection of galaxy clusters. , 390:1207–1216, November 2008. doi: 10.1111/j.1365-2966.2008.13823.x.

H. R. Russell, B. R. McNamara, A. C. Fabian, P. E. J. Nulsen, A. C. Edge, F. Combes, N. W. Murray, I. J. Parrish, P. Salomé, J. S. Sand ers, S. A. Baum, M. Donahue, R. A. Main, R. W. O'Connell, C. P. O'Dea, J. B. R. Oonk, G. Tremblay, A. N. Vantyghem, and G. M. Voit. ALMA observations of cold molecular gas filaments trailing rising radio bubbles in PKS 0745-191. , 458(3):3134–3149, May 2016. doi: 10.1093/mnras/stw409.

P. Salomé and F. Combes. Cold molecular gas in cooling flow clusters of galaxies. , 412:657–667, December 2003. doi: 10.1051/0004-6361:20031438.

J. S. Sanders. Contour binning: a new technique for spatially resolved X-ray spectroscopy applied to Cassiopeia A. , 371:829–842, September 2006. doi: 10.1111/j.1365-2966.2006.10716.x.

J. S. Sanders and A. C. Fabian. A deeper X-ray study of the core of the Perseus galaxy cluster: the power of sound waves and the distribution of metals and cosmic rays. , 381:1381–1399, November 2007. doi: 10.1111/j.1365-2966.2007.12347.x.

J. S. Sanders, A. C. Fabian, G. B. Taylor, H. R. Russell, K. M. Blundell, R. E. A. Canning, J. Hlavacek-Larrondo, S. A. Walker, and C. K. Grimes. A very deep Chandra view of metals, sloshing and feedback in the Centaurus cluster of galaxies. , 457:82–109, March 2016. doi: 10.1093/mnras/stv2972.

C. L. Sarazin. The Physics of Cluster Mergers. In L. Feretti, I. M. Gioia, and G. Giovannini, editors, *Merging Processes in Galaxy Clusters*, volume 272 of *Astrophysics and Space Science Library*, pages 1–38, June 2002. doi: 10.1007/0-306-48096-4_1.

C. L. Sarazin. *X-Ray Emission from Clusters of Galaxies*. June 2009.

Kosuke Sato, Kazuyo Tokoi, Kyoko Matsushita, Yoshitaka Ishisaki, Noriko Y. Yamasaki, Manabu Ishida, and Takaya Ohashi. Type Ia and II Supernovae Contributions to Metal Enrichment in the Intracluster Medium Observed with Suzaku. , 667(1):L41–L44, Sep 2007. doi: 10.1086/522031.

P. Sharma, M. McCourt, E. Quataert, and I. J. Parrish. Thermal instability and the feedback regulation of hot haloes in clusters, groups and galaxies. , 420:3174–3194, March 2012. doi: 10.1111/j.1365-2966.2011.20246.x.

Prateek Sharma, Benjamin D. G. Chandran, Eliot Quataert, and Ian J. Parrish. Buoyancy Instabilities in Galaxy Clusters: Convection Due to Adiabatic Cosmic Rays and Anisotropic Thermal Conduction. , 699(1):348–361, Jul 2009. doi: 10.1088/0004-637X/699/1/348.

J. Shin, J.-H. Woo, and J. S. Mulchaey. A Systematic Search for X-Ray Cavities in Galaxy Clusters, Groups, and Elliptical Galaxies. , 227:31, December 2016. doi: 10.3847/1538-4365/227/2/31.

A. Simionescu, N. Werner, H. Böhringer, J. S. Kaastra, A. Finoguenov, M. Brüggen, and P. E. J. Nulsen. Chemical enrichment in the cluster of galaxies Hydra A. , 493(2):409–424, Jan 2009. doi: 10.1051/0004-6361:200810225.

Ashmeet Singh and Prateek Sharma. The cold mode: a phenomenological model for the evolution of density perturbations in the intracluster medium. , 446(2):1895–1906, Jan 2015. doi: 10.1093/mnras/stu2264.

R. K. Smith, N. S. Brickhouse, D. A. Liedahl, and J. C. Raymond. Standard Formats for Atomic Data: the APED. In G. Ferland and D. W. Savin, editors, *Spectroscopic Challenges of Photoionized Plasmas*, volume 247 of *Astronomical Society of the Pacific Conference Series*, page 161, 2001.

A. N. Vantyghem, B. R. McNamara, H. R. Russell, R. A. Main, P. E. J. Nulsen, M. W. Wise, H. Hoekstra, and M. Gitti. Cycling of the powerful AGN in MS 0735.6+7421 and the duty cycle of radio AGN in clusters. , 442:3192–3205, August 2014. doi: 10.1093/mnras/stu1030.

A. N. Vantyghem, B. R. McNamara, H. R. Russell, M. T. Hogan, A. C. Edge, P. E. J. Nulsen, A. C. Fabian, F. Combes, P. Salomé, S. A. Baum, M. Donahue, R. A. Main, N. W. Murray, R. W. O'Connell, C. P. O'Dea, J. B. R. Oonk, I. J. Parrish, J. S.

Sanders, G. Tremblay, and G. M. Voit. Molecular Gas Along a Bright H$\alpha$ Filament in 2A 0335+096 Revealed by ALMA. , 832(2):148, Dec 2016. doi: 10.3847/0004-637X/832/2/148.

A. N. Vantyghem, B. R. McNamara, H. R. Russell, A. C. Edge, P. E. J. Nulsen, F. Combes, A. C. Fabian, M. McDonald, and P. Salomé. Molecular Gas Filaments and Star-forming Knots Beneath an X-Ray Cavity in RXC J1504-0248. , 863(2):193, Aug 2018. doi: 10.3847/1538-4357/aad2e0.

A. Vikhlinin, A. Kravtsov, W. Forman, C. Jones, M. Markevitch, S. S. Murray, and L. Van Speybroeck. Chandra Sample of Nearby Relaxed Galaxy Clusters: Mass, Gas Fraction, and Mass-Temperature Relation. , 640:691–709, April 2006. doi: 10.1086/500288.

L. M. Voigt and A. C. Fabian. Thermal conduction and reduced cooling flows in galaxy clusters. , 347:1130–1149, February 2004. doi: 10.1111/j.1365-2966.2004.07285.x.

G. M. Voit. A Role for Turbulence in Circumgalactic Precipitation. , 868:102, December 2018. doi: 10.3847/1538-4357/aae8e2.

G. M. Voit and M. Donahue. Cooling Time, Freefall Time, and Precipitation in the Cores of ACCEPT Galaxy Clusters. , 799:L1, January 2015a. doi: 10.1088/2041-8205/799/1/L1.

G. M. Voit and M. Donahue. Cooling Time, Freefall Time, and Precipitation in the Cores of ACCEPT Galaxy Clusters. , 799:L1, January 2015b. doi: 10.1088/2041-8205/799/1/L1.

G. M. Voit, M. Donahue, G. L. Bryan, and M. McDonald. Regulation of star formation in giant galaxies by precipitation, feedback and conduction. , 519:203–206, March 2015a. doi: 10.1038/nature14167.

G. Mark Voit, Greg L. Bryan, Brian W. O'Shea, and Megan Donahue. Precipitation-regulated Star Formation in Galaxies. , 808(1):L30, Jul 2015b. doi: 10.1088/2041-8205/808/1/L30.

Michael Werner, Kieran Cleary, William Forman, Varoujan Gorjian, Ryan Hickox, Christine Jones, Stephen Murray, and Daniel Stern. Infrared Search for Hidden Active Galactic Nuclei. Spitzer Proposal, Mar 2008.

Ann I. Zabludoff and Marijn Franx. Morphology and Kinematics in Clusters of Galaxies. , 106:1314, Oct 1993. doi: 10.1086/116727.

# APPENDICES

# Appendix A

# Scaling Relations

## A.1 Jet Power and Radio Power Scaling Relations

We determine the mechanical power of the AGN using $P_{\rm jet} - P_{\rm radio}$ scaling relations which are available at different frequencies, typically at the 1.4 GHz passband. One such relation (Cavagnolo et al., 2010), used a bivariate correlated error and intrinsic scatter (BCES) algorithm and found the best-fit scaling relations for the 1.4 GHz band to be,

$$\log P_{\rm jet} = (0.75 \pm 0.14) \log P_{1.4} + (1.91 \pm 0.18), \tag{A.1}$$

where $P_{1.4}$ is in units of $10^{40}$ erg s$^{-1}$ and $P_{\rm cav}$ is in units of $10^{42}$ erg s$^{-1}$. The scatter of this relation is 0.78 dex. Another $P_{\rm jet} - P_{\rm radio}$ relation (Bîrzan et al., 2008), uses an ordinary least squares regression for a generalized radio power,

$$\log P_{\rm jet} = (0.48 \pm 0.07) \log P_{\rm radio} + (2.32 \pm 0.09), \tag{A.2}$$

which has a scatter of $\sim 0.83$ dex. Here $\rm P_{radio}$ and $P_{\rm cav}$ are in units of $10^{42}$ erg s$^{-1}$. Both the relation derived from (Bîrzan et al., 2008; Cavagnolo et al., 2010) are shown in Figure A.1.

Using the NASA/IPAC Extragalactic Database (NED) we obtained the spectral flux densitiy ($S_\nu$) of each clusters BCG at 1.4 GHz. This data was obtained at the National Radio Astronomy Observatory (NRAO) using the Very Large Array (VLA). The corresponding radio powers were obtained using the relation,

$$P_\nu = 4\pi D_L^2 S_\nu \nu, \tag{A.3}$$

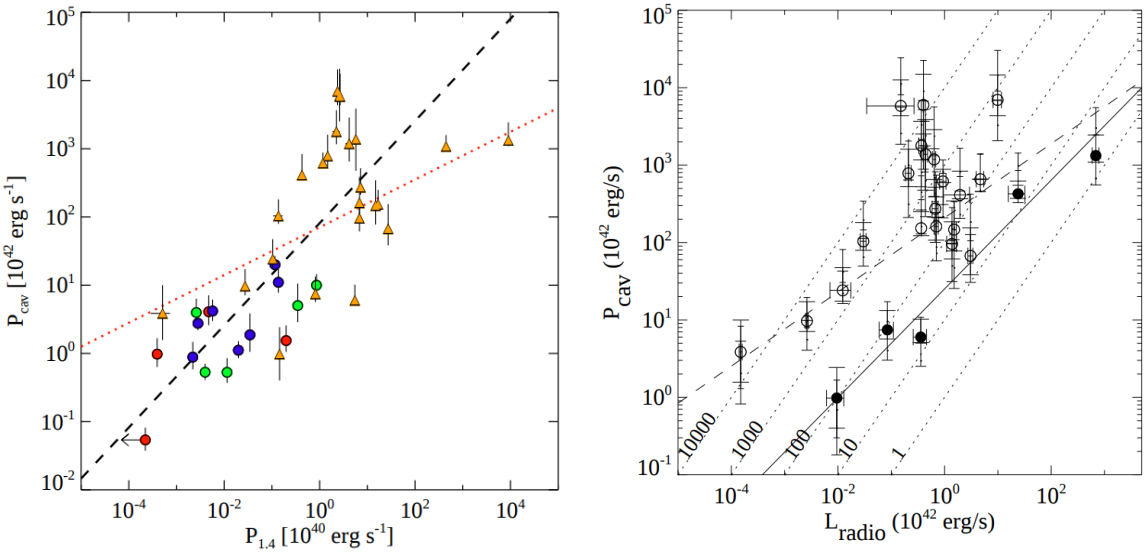


Figure A.1: **Left**: The mechanical AGN power plotted against the the radio power at 1.4 GHz taken from (Cavagnolo et al., 2010), orange triangles are clusters of galaxies from (Bîrzan et al., 2008), circle represent points from their sample. The dotted red line represents the best-fit power-law from (Bîrzan et al., 2008), and the dashed line is the BCES power law of Equation A.1. **Right**: Jet power versus bolometric radio power taken from (Bîrzan et al., 2008). "Short" and "medium" sized error bars denote upper and lower limits for the power required to inflate cavities using a sound speed and refill timescale respectively. All points are either filled or empty which correspond to radio filled or ghost cavities (lacks any significant radio emission in cavities) respectively, where dotted lines denote different ratios of cavity power to bolometric luminosity. The dashed line is a best-fit power law for the sample in Equation A.2, where the solid line is a best-fit for solid points only.

where $D_L$ is the luminosity distance, $z$ is the redshift, and $\nu = 1.4$ GHz. This was done for all clusters excluding A2107, for which no radio observations at this frequency are available. Instead, we adopted the integrated radio power from the ACCEPT database for this cluster (Voit and Donahue, 2015b). $P_{\rm jet}$ was calculated for all clusters using Equation A.1, except A2107 which was done using Equation A.2. Assuming a time frame based on the sound crossing time, $t_{\rm c}$, one can calculated the expected sizes of cavities at different radii given $P_{\rm jet}$, assuming that cavities are spherically symmetric. The possible sizes of circular cavities at 5 kpc and 10 kpc for each cluster are shown in Table A.1. This also shows that the bubble in RBS0533 is approximately within the expected size for a bubble at $R = 10$ kpc.

Table A.1: Cavity Sizes from $P_{\rm jet} - P_{\rm radio}$ Scaling Relations

| | | | | $R = 5$ kpc | | $R = 10$ kpc | |
|---|---|---|---|---|---|---|---|
| Cluster | BCG | $S_{1.4}$ (mJy) | $P_{\rm radio}$ $10^{40}$ erg s$^{-1}$ | $4PV$ $10^{58}$ erg | r (kpc) | $4PV$ $10^{58}$ erg | r (kpc) |
| | (1) | (2) | (3) | (4) | (5) | (4) | (5) |
| A2029 | IC 1101 | $541 \pm 20$[1] | $11.1 \pm 0.4$ | $14.2^{+8}_{-8}$ | $5.0^{+4.2}_{-4.2}$ | $25.1^{+14}_{-14}$ | $6.7^{+5.5}_{-5.5}$ |
| RBS0540 | MCG-01-12-005 | $130 \pm 30$[1] | $0.6 \pm 0.02$ | $2.2^{+1.0}_{-1.0}$ | $4.1^{+3.1}_{-3.1}$ | $4.3^{+2}_{-2}$ | $6.0^{+4.4}_{-4.4}$ |
| A2151 | NGC 6041 | 11[2] | 0.05 | $0.4^{+0.1}_{-0.1}$ | $3.4^{+2.0}_{-2.1}$ | $0.7^{+2}_{-2}$ | $4.5^{+3}_{-3}$ |
| A2107 | UGC 09958 | N/A | 0.08[3] | $0.3^{+0.1}_{-0.1}$ | $2.8^{+2}_{-2}$ | $0.4^{+0.2}_{-0.2}$ | $3.5^{+3}_{-3}$ |
| RBS0533 | NGC 1550 | $20 \pm 2.0$[4] | $0.01 \pm 0.001$ | $0.1^{+0.04}_{-0.04}$ | $2.6^{+1.7}_{-1.7}$ | $0.3^{+0.1}_{-0.1}$ | $4.0^{+3}_{-3}$ |

The mechanical power of the AGN with the possible cavity sizes calculated at 5 and 10 kpc from the cluster centre.

**Columns**: (1) name of the clusters BCG, (2) radio flux of the BCG measured at 1.4 GHz, (3) radio power measured at 1.4 GHz, excluding A2107, which was found using an integrated radio luminosity from the ACCEPT database (Voit and Donahue, 2015b), (3) jet power from the relation in Equation A.1 and Equation A.2, (4) the enthalpy required to create the cavity, (5) projected cavity radius. BCG spectral flux density measurement: [1] Condon et al. (1998), [2] Condon et al. (2002), [3] Taken from ACCEPT archive (Cavagnolo et al., 2008), [4] Brown et al. (2011).